University of Warsaw

Institute of Theoretical Physics

Mateusz Grzegorz Zych

Dynamics of bubble walls in cosmological first-order phase transitions

Doctoral dissertation prepared under the supervision of

dr hab. Marek Lewicki

September 2025

Abstract

Terminal velocity reached by bubble walls in cosmological first-order phase transitions is an important parameter determining both primordial gravitational wave spectrum and the production of baryon asymmetry in models of electroweak baryogenesis. In this dissertation, we summarize our efforts to better understand the impact of the early stages of bubble growth on its final fate. To this end, we developed a dedicated numerical code to study the real-time evolution of expanding bubbles and investigate how their walls approach stationary configurations.

We first focus on the approximation of local thermal equilibrium, within which we confirm that pure hydrodynamic backreaction can lead to steady-state expansion. In such cases, the resulting bubble-wall velocity agrees very well with analytic estimates known in the literature. However, this outcome is not generic. In many realistic scenarios, the early-stage dynamics following bubble nucleation allow walls to accelerate to supersonic speeds before a sufficient thermal shell can form in front of the wall. This often results in a runaway behaviour.

To account for this effect, we extend the analytical framework beyond the LTE regime. We identify a qualitative criterion that distinguishes between different modes of bubble wall propagation and determines which is physically realized in a given situation. This distinction is crucial for reliably assessing the cosmological consequences of first-order phase transitions.

Streszczenie

Prędkość osiągana przez ściany bąbli w kosmologicznych przemianach fazowych pierwszego rodzaju jest istotnym parametrem wpływającym zarówno na widmo pierwotnych fal grawitacyjnych, jak i na efektywność generacji asymetrii barionowej w modelach bariogenezy elektrosłabej. W niniejszej rozprawie podsumowujemy nasze wysiłki mające na celu lepsze zrozumienie wpływu wczesnych etapów wzrostu bąbli na ich późniejsze zachowanie. W tym celu opracowaliśmy kod numeryczny umożliwiający analizę ewolucji czasowej rosnących bąbli oraz badanie sposobu, w jaki ich ściany osiągają stany stacjonarne.

W pierwszej kolejności skupiamy się na przybliżeniu lokalnej równowagi termicznej, dla którego potwierdziliśmy, że czysto hydrodynamiczne sprzężenie zwrotne może prowadzić do osiągnięcia stanu ustalonego. W takich przypadkach prędkość ściany bąbla jest zgodna z dostępnymi w literaturze oszacowaniami analitycznymi. Niemniej jednak, nie jest to typowy scenariusz. W wielu realistycznych przypadkach dynamika bezpośrednio po nukleacji pozwala ścianom bąbli osiągać prędkości naddźwiękowe, zanim wytworzy się odpowiednia otoczka podgrzanej plazmy poprzedzająca ścianę. Prowadzi to wówczas do tzw. ucieczki ściany (ang. runaway).

Aby uchwycić ten efekt, uogólniamy podejście analityczne poza reżim lokalnej równowagi termicznej. Wprowadzamy jakościowe kryterium, pozwalające rozróżnić tryby ekspansji oraz określić, który z nich jest realizowany w danym przypadku. Wynik ten odgrywa kluczową rolę w ocenie wpływu przemiany fazowej na obserwacje kosmologiczne.

Contents

Preface

List of Publications

The research presented in this dissertation is primarily based on the following publications, which constitute the core scientific contributions of this work [1–3]:

1. T. Krajewski, M. Lewicki and M. Zych, *Hydrodynamical constraints on the bubble wall velocity*, Phys. Rev. D 108 (2023) no.10, 103523, [arXiv:2303.18216].

2. T. Krajewski, M. Lewicki and M. Zych, *Bubble-wall velocity in local thermal equilibrium: hydrodynamical simulations vs analytical treatment*, JHEP 05 (2024), 011, [arXiv:2402.15408].

3. T. Krajewski, M. Lewicki, I. Nałęcz and M. Zych, *Steady-state bubbles beyond local thermal equilibrium*, JHEP 06 (2025), 118, [arXiv:2411.16580].

In addition, some aspects of the thesis are supported by results obtained within complementary side projects [4–7]:

4. M. Lewicki, M. Merchand and M. Zych, *Electroweak bubble wall expansion: gravitational waves and baryogenesis in Standard Model-like thermal plasma*, JHEP 02 (2022), 017, [arXiv:2111.02393].

5. J. Ellis, M. Lewicki, M. Merchand, J. M. No and M. Zych, *The scalar singlet extension of the Standard Model: gravitational waves versus baryogenesis*, JHEP 01 (2023), 093, [arXiv:2210.16305].

6. M. Kierkla, G. Laverda, M. Lewicki, A. Mantziris, M. Piani, J. Rubio and M. Zych, *From Hubble to Bubble*, JHEP 11 (2023), 077, [arXiv:2309.08530].

7. T. Krajewski, M. Lewicki, M. Vasar, V. Vaskonen, H. Veermäe and M. Zych, *Thermalization effects on the dynamics of growing vacuum bubbles*, JHEP 03 (2025) 178, [arXiv:2411.15094].

Acknowledments

First and foremost, I would like to express my deepest gratitude to my supervisor, dr hab. Marek Lewicki, for his continuous support, guidance, and patience throughout my doctoral studies. His expertise, encouragement, and insightful feedback have been invaluable in shaping this work.

I am also grateful to all my collaborators and colleagues with whom I had the pleasure of working during this journey. Our discussions, sometimes challenging, often inspiring, greatly contributed to the scientific depth and clarity of this dissertation. Special thanks go to dr Tomasz Krajewski and Ignacy Nałęcz, without whose knowledge, skills, and help a significant part of this work would not have been possible. I would also like to thank my friends and family for their unwavering support and understanding throughout these years.

This work was supported by the National Science Center through the research grants no. 2018/31/D/ST2/02048 and 2023/50/E/ST2/00177, as well as by the Polish National Agency for Academic Exchange within the Polish Returns Programme, no. PPN/PPO/2020/1/00013/U/00001. I also acknowledge support from the IDUB Early Universe scholarship program during final stages of my work. Without this financial support, the research presented here would not have been possible.

Acronyms and conventions

Below the acronyms used throughout the dissertation are explained:

CMB	cosmic microwave background
EoS	equation of state
EoM	equation(s) of motion
FCT	flux-corrected transport
FOPT	first-order phase transition
GW	gravitational waves
LISA	Laser Interferometer Space Antenna
LTE	local thermal equilibrium
SM	Standard Model (of particle physics)
SNR	signal-to-noise ratio
VEV	vacuum expectation value

The following conventions are used throughout the whole dissertation:

- Greek indices $(\mu, \nu, \dots)$ run over $0, 1, 2, 3$, while Latin indices $(i, j, \dots)$ run over $1, 2, 3$, unless stated otherwise
- Natural system of units is used, where the Boltzmann constant, the speed of light and the reduced Planck constant are equal to unity: $k_B = c = \hbar = 1$. Hence, all quantities are expressed in appropriate powers of gigaelectronvolts (GeV).

Introduction

Physical cosmology has come a long way, since its humble beginnings over a hundred years ago, when Albert Einstein formulated his General Theory of Relativity. This revolutionary framework redefined our understanding of gravity and provided the mathematical foundation for describing the Universe as a dynamic structure. Around the same time, Edwin Hubble observed distant galaxies and discovered a striking correlation between their velocities and distances from us. Known today as Hubble–Lemaître law, it was historically the first observational evidence for the expansion of our Universe and sparked speculation about its origin. Georges Lemaître, considered today to be the first to propose the hypothesis of the hot Big Bang, laid the groundwork for modern cosmological theory, which has since evolved in close interplay with observational data. A major breakthrough came in the 1960s, when the cosmic microwave background was accidentally discovered by Arno Penzias and Robert Wilson [8], providing compelling evidence in favor of Big Bang cosmology. Over the subsequent decades, the era of precise experiments began with the launch of the COBE [9], WMAP [10], and Planck [11] missions. The excellent angular resolution of these missions allowed for the study of tiny anisotropies in the CMB, which now constitute the most important source of our knowledge about the early Universe, summarized in the ΛCDM model. However, this picture is far from being complete. There is no convincing candidate for dark matter, the nature of dark energy remains unknown, not to mention other unresolved issues such as searches for the origin and dynamics of cosmic inflation.

The second pillar of our understanding of the fundamental interactions is the Standard Model of particle physics, one of the most successful and well-established theoretical frameworks in modern physics. Its origins date back to the mid-20th century, when progress in quantum mechanics and special relativity culminated in the development of quantum field theory - the theoretical backbone of the Standard Model. The critical milestone was the unification of electromagnetic and weak interactions by Sheldon Glashow, Steven Weinberg, and Abdus Salam, earning them the Nobel Prize in Physics [12–14]. The prediction and subsequent discovery of the W and Z bosons at CERN in the early 1980s provided further validation of the electroweak theory [15, 16]. The crowning achievement came in 2012 with the detection of the Higgs boson at the Large Hadron Collider [17, 18], confirming the mechanism responsible for mass generation through spontaneous symmetry breaking, initially theorized by Peter Higgs, François Englert and others in the 1960s [19–21]. Despite its success, the Standard Model also remains a work in progress. It does not provide solutions to the problems of modern cosmology, suggesting that a deeper, more encompassing theory still awaits discovery.

A significant breakthrough may be on the horizon, thanks to recent advances in gravitational-wave astronomy. The first detection of GWs by the LIGO collaboration [22] opened an entirely new observational window into the cosmos, allowing scientists to use minute distortions of spacetime to collect data from astrophysical processes. So far, the observed sources have primarily been mergers of black holes or neutron stars. However, GW interferometers may also provide direct access to the physics of the Early Universe - an epoch that remains largely inaccessible to conventional electromagnetic observations. Before photon decoupling, the primordial plasma was opaque to light, but gravitational waves could propagate freely, which makes them a unique messenger from the dawn of time. Detecting the stochastic background from these earliest epochs is one of the primary goals of next-generation GW experiments. From a cosmological perspective, the LISA mission [23], planned for launch in the 2030s, appears particularly well-suited to this task. It aims to probe the frequency band around ~ 1 mHz, associated with energies relevant to the Early Universe near the electroweak scale (i.e., $T \sim 100$ GeV).

One of the most promising sources of the GW stochastic background at these scales is a cosmological first-order phase transition, predicted by many extensions of the Standard Model. It proceeds via the nucleation of bubbles of the broken vacuum within a sea of metastable phase and can be qualitatively illustrated by the familiar process of boiling water. In this everyday analogy, thermodynamic fluctuations cause bubbles of vapour to spontaneously form within the liquid, eventually converting the entire water into vapour. A similar scenario could take place in the Early Universe, when the transition occurred between the false and the true vacuum of the scalar potential. Bubbles of the new phase spontaneously nucleated and began to grow. As these bubbles expanded, they interacted with the surrounding plasma of relativistic particles, generating shock waves, turbulence and acoustic waves. Furthermore, bubbles nucleating in different regions could collide, leading to complex dynamics. All these processes seeded stress-energy inhomogeneities, which were ultimately converted into spacetime distortions, propagating as gravitational waves.

Another compelling motivation to postulate an electroweak first-order phase transition in the thermal history of our Universe is the unresolved puzzle of matter-antimatter asymmetry. In the standard cosmological model, matter and antimatter should have been created in equal amounts during the early stages of the Universe. Yet, observations show that matter dominates, with almost no primordial antimatter present today. Resolving this discrepancy requires some processes that satisfy Sakharov's conditions [24]. The nucleation and expansion of bubbles associated with a first-order phase transition offer just such a scenario. As a result, the electroweak baryogenesis [25–28] taking place at the surfaces of growing bubbles could explain the origin of the observable baryon asymmetry.

Thus, a comprehensive understanding of phase transition dynamics is essential for accurately predicting both the generation of baryon asymmetry in electroweak baryogenesis scenarios and the spectra of gravitational waves produced during first-order phase transitions. While most of the thermodynamic parameters describing these processes are fairly well understood, the computation of the bubble-wall velocity, despite recent progress [29–37], remains an active area of research. The growing bubbles are driven by the potential difference between the phases inside and outside the wall. On the other hand, particles in the surrounding plasma collide with the bubble wall, exerting

velocity-dependent friction on it. These two forces may balance each other, leading to steady expansion at constant velocity. Otherwise, the bubble wall may continue to accelerate and approach a velocity very close to the speed of light. This distinction has significant implications for cosmological observables. Bubble walls with moderate, constant velocities are typically more favourable for efficient baryon asymmetry generation, while the ultra-relativistic walls tend to produce stronger GW signals. Accurate modelling and careful evaluation of the wall velocity are therefore key steps in bridging theoretical models with experimental data from future gravitational wave detectors.

This dissertation summarizes our efforts to better understand the dynamics of bubble walls in cosmological first-order phase transitions, with particular emphasis on evaluating their velocity. In Chapter 1, we lay the theoretical foundation by reviewing the basic principles underlying cosmological phase transitions. This includes a discussion of the evolution of the scalar potential and the tunnelling process that leads to the formation of critical bubbles. Key tools and transition parameters used throughout the thesis are introduced. We also explore more exotic scenarios where the transition is gravitationally induced [6]. Finally, we discuss gravitational wave production, presenting templates for the resulting spectra.

Chapter 2 focuses on the real scalar singlet extension of the Standard Model, a simple yet extensively studied framework capable of realizing a relatively strong first-order electroweak phase transition. After outlining the effective potential and vacuum structure, we present transition parameters across the model's parameter space and discuss its observational prospects. These results serve as benchmark points for the main parts of the dissertation, presented in Chapters 3 and 4, where we report most of the original findings [1–3].

In Chapter 3, we investigate bubble-wall expansion using a hydrodynamic description based on the bag model. We analyze the plasma profiles around the bubble wall and review the recently developed local thermal equilibrium (LTE) approximation [31, 34], which provides a simple estimate that can be interpreted as an upper limit on the bubble-wall velocity for a given model. Using a similar framework, we generalize this description by introducing the entropy production rate at the bubble front. This allows us to go beyond the LTE approximation and relate the wall velocity to the effective friction exerted by the plasma.

Chapter 4 validates these predictions using real-time numerical simulations of bubble growth. We begin by presenting the simulation setup, highlighting key aspects of the discretization and the implementation of the problem on the lattice. The performance of the code is verified using typical toy models introduced in similar contexts [38–40]. Our analysis reveals that not all velocities are dynamically realized, with the size of the velocity gap systematically depending on the model parameters.

Next, we move to a more realistic model: the scalar singlet extension of the Standard Model (see Chapter 2), and study the process of bubble growth within the local thermal equilibrium scenario. We observe that the early-stage evolution of the bubble wall often prevents the system from reaching the analytically predicted steady state. Nevertheless, in some rare, fine-tuned cases where stationary states are reached, both methods agree remarkably well. Fortunately, our generalized formalism explains this behaviour by predicting an additional branch of stable relativistic solutions, clearly visible in numerical simulations, approaching the speed of light in the limit of vanishing friction. The presence of this branch provides a convenient criterion to distinguish between physical and unphysical expansion modes, as the faster solution prevails dynamically.

We conclude by emphasizing the importance of starting from a well-motivated initial configuration when evaluating bubble-wall velocities. Our findings offer a practical selection rule for predicting the final outcome of bubble evolution without resorting to computationally demanding simulations. These insights could play a crucial role in improving the modelling, interpretation, and reconstruction of gravitational wave signals in future experiments. If confirmed, these results may also place significant constraints on models capable of successful electroweak baryogenesis.

CHAPTER 1

Theoretical description of cosmological first-order phase transitions

Studies on cosmological first-order phase transitions date back to the pioneering works of Sidney Coleman, who introduced the concept of false vacuum decay [41, 42]. He developed a semiclassical theory for scalar fields describing how a system initially trapped in a metastable state, the false vacuum, can transition to a more stable and energetically favourable true vacuum. This process is realized through the spontaneous nucleation of bubbles of the new phase, which then expand and eventually complete the transition. These early developments focused on vacuum transitions at zero temperature.

The extension to finite-temperature systems, crucial for understanding phase transitions in the early Universe, was proposed by Andrei Linde [43], who demonstrated how thermal fluctuations can catalyse bubble nucleation. Building on this foundation, subsequent studies refined the treatment of thermal potentials and developed systematic methods for incorporating temperature-dependent corrections into the effective potential [44]. These advancements laid the groundwork for realistic modelling of first-order phase transitions, enabling detailed analysis of transition dynamics, such as nucleation rates, bubble growth, and their thermodynamic and observational implications.

In this chapter, we review the key theoretical aspects of cosmological first-order phase transitions and introduce the main tools used to describe them. Most derivations are based on seminal works [41, 44] as well as standard textbooks [45, 46]. We begin with an introduction to the theory of a single scalar field, deriving the spherically symmetric equations of motion that govern the tunnelling process. Next, we present a simple quartic potential to illustrate generic thermal evolution and explore methods for finding the critical bubble, providing useful approximations along the way. Subsequently, we examine the origin of thermal corrections in greater detail and introduce key parameters characterizing phase transitions, such as the nucleation temperature, transition strength, and duration.

After summarizing the standard treatment of thermally induced transitions, we turn to a novel mechanism of gravitationally induced phase transitions, originally proposed in [6]. Finally, we discuss the generation of gravitational waves during cosmological first-order transitions, reviewing the main sources, with particular emphasis on acoustic waves in the plasma, and present the most recent templates for the resulting GW spectra [47].

1.1 Basics of scalar field theory

The description of cosmological phase transitions often begins with a classical field-theoretic approach to scalar fields. In particular, the mechanism of false vacuum decay can be studied using a simple model involving a single real scalar field $\phi(x)$ defined in four-dimensional Minkowski spacetime. The dynamics of this field are governed by the Lagrangian density

$$\mathcal{L} = \frac{1}{2}(\partial_\mu \phi)(\partial^\mu \phi) - V(\phi), \tag{1.1}$$

where $V(\phi)$ is the scalar potential characterizing the self-interactions of the field and determining the structure of its vacua. The equation of motion for ϕ follows from the Euler–Lagrange equation

$$\partial_\mu \left(\frac{\partial \mathcal{L}}{\partial(\partial_\mu \phi)} \right) - \frac{\partial \mathcal{L}}{\partial \phi} = 0, \tag{1.2}$$

which leads to the well-known Klein–Gordon equation

$$\partial_\mu \partial^\mu \phi + \frac{\partial V}{\partial \phi} = 0. \tag{1.3}$$

In the study of quantum tunnelling between vacua, it is convenient to perform a Wick rotation to Euclidean time by setting $\tau = it$. This transforms the Minkowski metric into the Euclidean one and modifies the equation of motion accordingly:

$$\left(\frac{\partial^2}{\partial\tau^2} + \nabla^2\right)\phi = \frac{\partial V}{\partial\phi}. \tag{1.4}$$

Solutions relevant for tunnelling in the zero-temperature limit are assumed to be spherically symmetric in four dimensions. This $O(4)$ symmetry implies that the field only depends on the radial coordinate $\varrho = \sqrt{\tau^2 + x^2 + y^2 + z^2}$. To express the Laplacian in terms of ϱ, one needs to rewrite the differential operators. For example,

$$\frac{\partial}{\partial x} = \frac{\partial\varrho}{\partial x}\frac{\partial}{\partial\varrho} = \frac{x}{\varrho}\frac{\partial}{\partial\varrho} \tag{1.5}$$

and

$$\begin{aligned}\frac{\partial^2}{\partial x^2} &= \frac{\partial}{\partial x}\frac{\partial}{\partial x} = \frac{x}{\varrho}\frac{\partial}{\partial\varrho}\left(\frac{x}{\varrho}\frac{\partial}{\partial\varrho}\right) = \frac{x}{\varrho}\left(\frac{1}{\varrho} - \frac{x^2}{\varrho^3}\right)\frac{\partial}{\partial\varrho} + \frac{x^2}{\varrho^2}\frac{\partial^2}{\partial\varrho^2} \\ &= \left(\frac{1}{\varrho} - \frac{x^2}{\varrho^3}\right)\frac{\partial}{\partial\varrho} + \frac{x^2}{\varrho^2}\frac{\partial^2}{\partial\varrho^2}.\end{aligned} \tag{1.6}$$

Applying similar transformations to the other coordinates, one obtains the full equation of motion, which simplifies to

$$\begin{aligned}\left(\frac{\partial^2}{\partial\tau^2} + \nabla^2\right)\phi &= \left(\frac{\tau^2 + x^2 + y^2 + z^2}{\varrho^2}\right)\frac{\partial^2\phi}{\partial\varrho^2} + \left(\frac{4}{\varrho} - \frac{\tau^2 + x^2 + y^2 + z^2}{\varrho^3}\right)\frac{\partial\phi}{\partial\varrho} = \\ &= \frac{\partial^2\phi}{\partial\varrho^2} + \frac{3}{\varrho}\frac{\partial\phi}{\partial\varrho} = \frac{\mathrm{d}V}{\mathrm{d}\phi},\end{aligned} \tag{1.7}$$

which corresponds to a one-dimensional radial field equation with a damping term proportional to $1/\varrho$. The associated Euclidean action for the $O(4)$-symmetric solution, obtained by integrating the Lagrangian over four-dimensional Euclidean space, takes the form

$$S_4 = 2\pi^2\int_0^\infty \varrho^3\mathrm{d}\varrho\left[\frac{1}{2}\left(\frac{\mathrm{d}\phi}{\mathrm{d}\varrho}\right)^2 + V(\phi)\right], \tag{1.8}$$

and is the relevant quantity determining the tunnelling probability via the semiclassical approximation, as discussed later in this chapter.

At finite temperatures, quantum tunnelling is replaced by thermal fluctuations, and the dominant field configurations become static in Euclidean time and exhibit spherical symmetry in the remaining three spatial dimensions ($O(3)$-symmetric solution). In this

case, the radial coordinate is defined as $r = \sqrt{x^2 + y^2 + z^2}$, and the equation of motion reduces to

$$\frac{\mathrm{d}^2\phi}{\mathrm{d}r^2} + \frac{2}{r}\frac{\mathrm{d}\phi}{\mathrm{d}r} = \frac{\mathrm{d}V}{\mathrm{d}\phi}. \tag{1.9}$$

The corresponding Euclidean action for the three-dimensional theory is

$$S_3 = 4\pi \int_0^\infty r^2 \mathrm{d}r \left[\frac{1}{2}\left(\frac{\mathrm{d}\phi}{\mathrm{d}r}\right)^2 + V(\phi)\right] \tag{1.10}$$

and the full finite-temperature tunnelling rate is governed by the dimensionless combination S_3/T, where the inverse temperature corresponds to the extent of the compactified Euclidean time direction. With the general form of the equations of motion established, we now turn to solving them in specific potentials that exhibit metastable vacua.

1.2 Decay of the false vacuum

Before turning to realistic extensions of the Standard Model where the electroweak symmetry breaking may occur via a first-order phase transition, we begin by examining the essential features of such transitions through a simple illustrative model. Consider a general quartic scalar potential given by

$$V_0(\phi) = -\frac{1}{2}\mu^2\phi^2 - \frac{1}{3}\mu_3\phi^3 + \frac{1}{4}\lambda\phi^4 \tag{1.11}$$

with $\lambda > 0$, that in the relevant part of the parameter space possesses two local minima at $\phi = 0$ and $\phi = \upsilon$. Defining $\eta = \mu_3/(\lambda\upsilon) - 1$, the potential can be rewritten as

$$V_0(\phi) = \lambda\left(\frac{\eta}{2}\upsilon^2\phi^2 - \frac{1+\eta}{3}\upsilon\phi^3 + \frac{1}{4}\phi^4\right), \tag{1.12}$$

where the thermal evolution of the potential is encoded in the parameter η. For $\eta > 1/2$ the symmetry is restored, as the vacuum lies at the origin $\phi = 0$, corresponding to the high-temperature limit. The value $\eta = 1/2$ corresponds to the so-called critical temperature T_c, where two minima are degenerate. Below the critical temperature (for $0 < \eta < 1/2$), symmetry breaking can occur, as the second minimum at $\phi = \upsilon$ becomes the global one. At a temperature T_0 (for $\eta = 0$) the barrier vanishes, leaving only the symmetry-breaking vacuum. Qualitative evolution of the scalar potential is depicted on the left panel of Fig. 1.1. To understand how the transition between vacua proceeds, we now turn to the study of the bounce solution that mediates the decay.

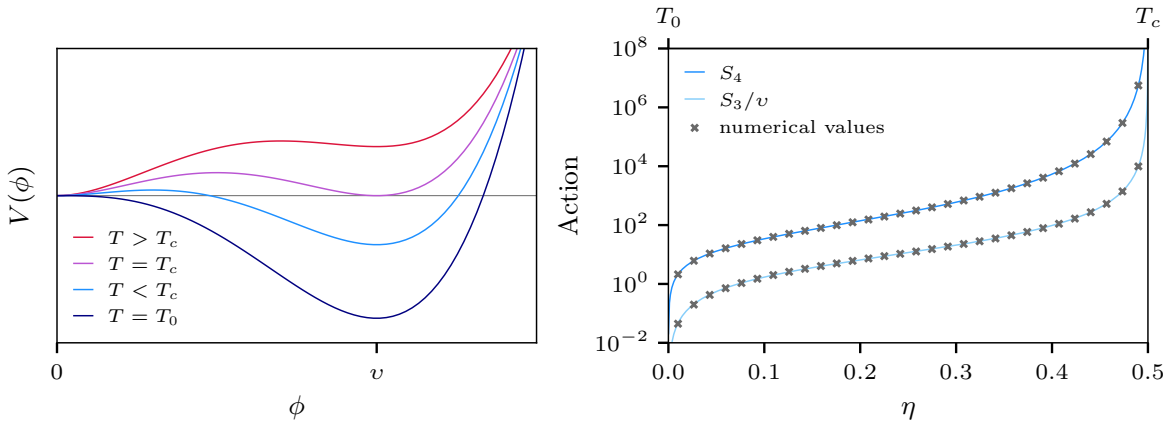

Figure 1.1: *Effective potential and Euclidean action in first-order phase transitions.* ***Left panel:*** *Thermal evolution of the scalar potential in typical models with a first-order phase transition. Different colours represent different temperatures. Tunnelling is allowed for* $T_0 < T < T_c$. ***Right panel:*** *Euclidean action as a function of temperature (parametrised by* η*). Blue curves represent analytical expressions for* S_4 *and* S_3 *(eq.* (1.14) *and* (1.17) *respectively). Gray crosses denote the numerical results obtained by evaluating the integrals* (1.8) *and* (1.10) *for the tunnelling profiles. The action diverges near* T_c *and vanishes as the barrier disappears.*

The process of symmetry breaking in cosmological first-order phase transitions proceeds through quantum tunnelling (or thermal fluctuations) between the metastable false vacuum (here at $\phi = 0$) and the true vacuum (here at $\phi = v$). To find the tunnelling bubble, also known as the bounce solution, one must solve the appropriate equation of motion: (1.9) for the thermal fluctuations or (1.7) for pure quantum tunnelling, with the correct boundary conditions. In what follows, we focus on thermally induced transitions and the corresponding $O(3)$-symmetric equation of motion, but the vacuum case is fully analogous. The relevant boundary conditions read

$$\left.\frac{\mathrm{d}\phi}{\mathrm{d}r}\right|_{r=0} = 0 \qquad \text{and} \qquad \lim_{r\to\infty} \phi(r) = 0. \tag{1.13}$$

The value of $\phi(r = 0) = \phi_e$ is, in principle, unknown and is implicitly determined by the other two boundary conditions; it is called the escape point.

Since an analytical solution of this problem does not exist, we now briefly outline the strategy for finding the field profile $\phi(r)$, which can be interpreted as the critical

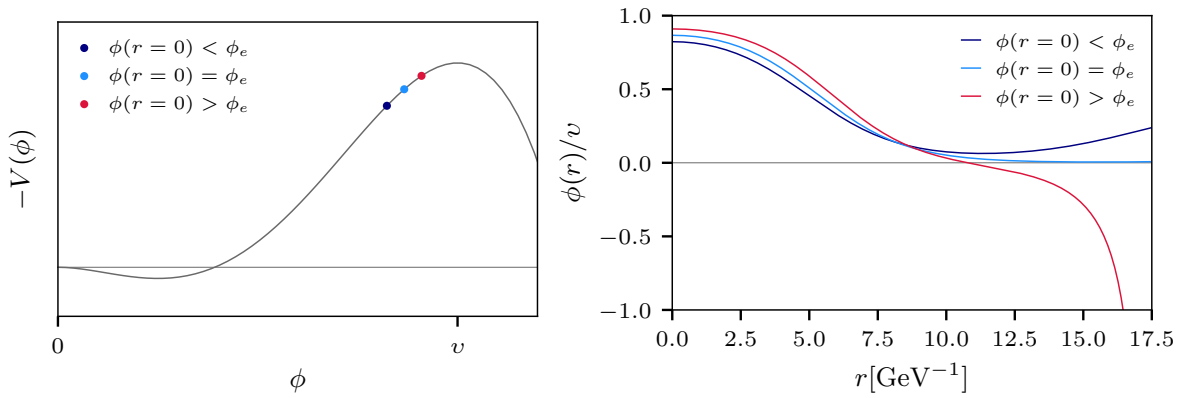

Figure 1.2: *Shooting method used to find the critical bubble.*
Left panel: *Inverted scalar potential with different boundary conditions marked with different colours. Light blue dot represents the escape point ϕ_e, while dark blue and red denotes lower and higher values, respectively.*
Right panel: *Solutions of the bounce equation of motion corresponding to different initial field values.*

bubble [45]. Although this may seem like a purely mathematical exercise, the problem admits a compelling physical analogy. It can be mapped onto the classical dynamics of a particle moving in the inverted potential $-V(\phi)$, subject to a friction-like force proportional to velocity. Interpreting ϕ as the position and r as time, the escape point ϕ_e corresponds to the initial position from which the particle gradually approaches $\phi = 0$ as $r \to \infty$. This analogy offers valuable intuition for the structure of the solution.

Operationally, the escape point can be found using the numerical shooting method, illustrated in Figure 1.2. If the initial value is too low, the field "undershoots" and never reaches the false vacuum. Conversely, if it is too high, the field "overshoots", reaching the false vacuum at finite r with non-zero velocity. By employing the bisection search method, the escape point ϕ_e can be determined with arbitrary precision. The resulting bounce solution not only determines the tunnelling rate, but also serves as the basis for computing the nucleation temperature and other physical observables relevant to cosmological phase transitions, as discussed later in this chapter.

1.3 Analytical approximation for the Euclidean action

For a broad class of quartic potentials, such as the one represented by equation (1.11), a semi-analytic formula for the Euclidean action exists [48]. This approximation is particularly useful when the tunnelling profile is not explicitly needed, as demonstrated in [6]. For quantum tunnelling, the $O(4)$-symmetric action can be expressed as

$$S_4 = \frac{4\pi^2}{3\lambda}\frac{\alpha_1\delta + \alpha_2\delta^2 + \alpha_3\delta^3}{(2-\delta)^3}, \tag{1.14}$$

where the parameter δ is given by

$$\delta = \frac{9\lambda\mu^2}{\mu_3^2}. \tag{1.15}$$

The numerical values of the coefficients are

$$\alpha_1 = 13.832, \qquad \alpha_2 = -10.819, \qquad \alpha_3 = 2.0765. \tag{1.16}$$

Similarly, the approximation of the $O(3)$-symmetric action is given by

$$S_3 = \frac{64\sqrt{2}\pi\mu_3}{243\lambda^{3/2}}\sqrt{\frac{\delta}{2}}\frac{\beta_1\delta + \beta_2\delta^2 + \beta_3\delta^3}{(2-\delta)^2}, \tag{1.17}$$

with numerical coefficients

$$\beta_1 = 8.2938, \qquad \beta_2 = -5.5330, \qquad \beta_3 = 0.8180. \tag{1.18}$$

The validity of these approximations for the benchmark potential is demonstrated in the right panel of Fig. 1.1, where the qualitative evolution of the Euclidean action is also shown.

1.4 Origin of the thermal potential

Once the qualitative behaviour of the effective potential has been established, it is crucial to examine the temperature-dependent corrections that govern its evolution. These contributions arise from the presence of particles in the thermal bath and can be systematically computed using the real-time formalism [44]. At the one-loop level, the finite-temperature correction from a particle species i is given by

$$V_i = \pm \int \frac{\mathrm{d}^3k}{(2\pi)^3}\frac{1}{2E_i} f_{\mp}(k), \tag{1.19}$$

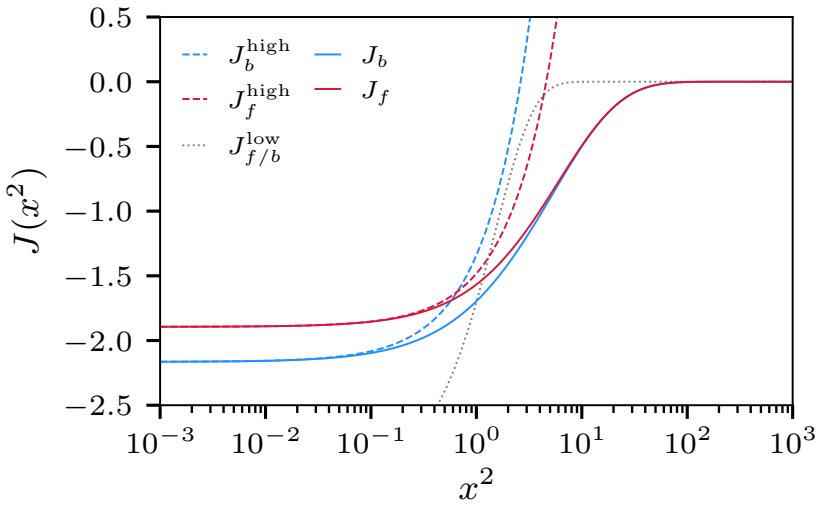

Figure 1.3: *Bosonic (blue) and fermionic (red) thermal functions* $J_{\mathrm{b/f}}$*, plotted as functions of* $x^2 = m^2/T^2$*, together with their high- and low-temperature expansions. The solid lines represent the exact numerical results, while the dashed and dotted curves show the corresponding analytical approximations.*

where the upper (lower) sign corresponds to bosons (fermions), and $f_{\mp}(k)$ denotes the equilibrium distribution functions:

$$f_{\mp}(k) = \frac{1}{\exp(-\beta E_i) \mp 1}, \tag{1.20}$$

which follow from Bose-Einstein and Fermi-Dirac statistics, respectively. Here, $\beta = 1/T$ is the inverse temperature, and $E_i = \sqrt{k^2 + m_i^2(\phi)}$ is the energy of a mode with mass $m_i(\phi)$. By integrating over $m_i^2(\phi)$, equation (1.19) can be rewritten in a more convenient form:

$$\begin{aligned} V_i &= \pm \frac{1}{\beta} \int \mathrm{d}m_i^2(\phi) \frac{\mathrm{d}}{\mathrm{d}m_i^2} \int \frac{\mathrm{d}^3k}{(2\pi)^3} \log(1 \mp \exp(-\beta E_i)) = \\ &= \pm \frac{T^4}{2\pi^2} \int \mathrm{d}y y^2 \log\left(1 \mp \exp\left(-\sqrt{y^2 + \frac{m_i^2(\phi)}{T^2}}\right)\right) = \\ &= \frac{T^4}{2\pi^2} J_{\mathrm{b/f}}\left(\frac{m_i^2}{T^2}\right), \end{aligned} \tag{1.21}$$

where we introduced the dimensionless integration variable $y = k/T$. The functions $J_{\mathrm{b/f}}$ are known as the bosonic and fermionic thermal functions, respectively.

In the relativistic limit ($T \gg m$), these functions can be expanded as

$$J_{\mathrm{b}}(x) \approx -\frac{\pi^4}{45} + \frac{\pi^2}{12}x^2 + \mathcal{O}(x^3) \qquad \text{and} \qquad J_{\mathrm{f}}(x) \approx -\frac{7}{8}\frac{\pi^4}{45} + \frac{\pi^2}{24}x^2 + \mathcal{O}(x^4 \log x^2), \tag{1.22}$$

a result commonly referred to as the high-temperature approximation.

In the opposite, non-relativistic limit ($m \gg T$), the thermal functions exhibit exponential suppression:

$$J_{\mathrm{b/f}}(x) \approx -\sqrt{\frac{\pi}{2}} x^{\frac{3}{2}} e^{-x} \left[1 + \frac{15}{8} x^{-1} + \frac{105}{128} x^{-2}\right]. \tag{1.23}$$

The shapes of the thermal functions, together with their high- and low-temperature approximations, are presented in Fig. 1.3. The full one-loop thermal potential is obtained by summing over all species, with each species contributing according to its number of degrees of freedom n_i, as

$$V_T = \frac{T^4}{2\pi^2} \sum_i n_i J_{\mathrm{b/f}}\left(\frac{m_i}{T}\right), \tag{1.24}$$

providing the foundation for analysing high-temperature behaviour of the system.

1.5 Phase transition parameters

After developing the formalism for the effective potential and the bounce action, we now turn to extracting physical parameters that describe the dynamics of the phase transition. In particular, we are interested in when and how bubbles of the true vacuum form, as well as in quantifying the strength and duration of the transition. These parameters are essential for assessing the cosmological impact of the phase transition, including possible observational signatures.

A key quantity in this context is the nucleation rate Γ, which characterizes the probability of bubble formation per unit volume and time as the Universe cools. It is typically defined as the exponential of the Euclidean action:

$$\Gamma \sim \exp(-S). \tag{1.25}$$

In practice, the rate is approximated by the dominant contribution from either thermally-induced or quantum tunnelling processes [42, 49]:

$$\Gamma(T) = \max\left[T^4 \left(\frac{S_3}{2\pi T}\right)^{\frac{3}{2}} \exp\left(\frac{-S_3}{T}\right), R_0^{-4} \left(\frac{S_4}{2\pi}\right)^2 \exp(-S_4)\right], \tag{1.26}$$

where the three- and four-dimensional Euclidean actions are given in (1.10) and (1.8), respectively, and R_0 denotes the physical radius of the nucleated bubble. At high temperatures, thermal fluctuations dominate, and the quantum tunneling rate is typically

negligible. However, at very low temperatures or in models where the transition is non-thermal (see [6]), the quantum contribution can become significant.

The nucleation temperature T_n is defined as the point at which the probability of nucleating at least one bubble within a Hubble volume becomes order one [50], i.e.,

$$N(T_n) = \int_{T_n}^{T_c} \frac{dT}{T} \frac{\Gamma(T)}{H(T)^4} \approx 1. \tag{1.27}$$

Assuming that the phase transition proceeds rapidly, much faster than the Hubble time, the expansion rate of the Universe can be treated as approximately constant ($H(t) \approx$ const). In this case, the condition in (1.27) simplifies to

$$\frac{S_3}{T_n} \approx 4 \log \left(\frac{T_n}{H} \right), \tag{1.28}$$

which, for temperatures near the electroweak scale, yields the commonly used criterion $S_3/T_n \approx 140$ [51]. A useful measure of the degree of supercooling is the ratio between the nucleation and critical temperatures, T_n/T_c.

While the nucleation temperature T_n marks the point at which the probability of a single bubble forming within a horizon volume becomes significant, it does not signal the completion of the phase transition. At T_n, the Universe is still predominantly in the false vacuum. The probability that a randomly chosen point remains in the false vacuum at time t is given by

$$P(t) = e^{-I(t)}, \tag{1.29}$$

where $I(t)$ represents the fraction of space that has already transitioned to the true vacuum. It is given by the expression

$$I(t) = \frac{4\pi}{3} \int_{t_c}^{t} dt' \Gamma(t') a(t')^3 r(t, t')^3. \tag{1.30}$$

with $a(t)$ being the scale factor and $r(t, t')$ the physical radius of a bubble nucleated at time t' and expanding with velocity v_w until time t, as

$$r(t, t') = \int_{t'}^{t} \frac{v_w(\tilde{t}) d\tilde{t}}{a(\tilde{t})}. \tag{1.31}$$

A key moment in the transition is the percolation time t_p, which marks when a significant portion of space has undergone the transition to the true vacuum. This is typically defined as the time when $P(t_p) \approx 0.71$, or equivalently, when $I(t_p) \approx 0.34$ [50].

In practical calculations, it is more convenient to express these quantities in terms of temperature, T, rather than time. The space fraction can then be rewritten as

$$I(T) = \frac{4\pi}{3} \int_T^{T_c} \frac{dT'}{H(T')} \Gamma(T') \frac{r(T,T')^3}{T'^4}, \tag{1.32}$$

which leads to the definition of the percolation temperature T_p as the temperature for which

$$I(T_p) = 0.34. \tag{1.33}$$

Although, in principle, all parameters describing the phase transition should be evaluated at the percolation temperature, in this work we focus on moderately strong transitions for which $T_p \approx T_n$. Therefore, we will not distinguish between these two temperatures in the following analysis.

Another important parameter characterizing the phase transition is its duration, often quantified by the inverse time scale β. This quantity captures how rapidly the nucleation rate grows and is defined as the time derivative of the action at the moment of nucleation:

$$\beta = -\frac{\mathrm{d}}{\mathrm{d}t} S \bigg|_{t_n}. \tag{1.34}$$

Here, t_n denotes the time corresponding to the nucleation temperature T_n. Assuming radiation domination, where the scale factor scales as $a \sim T^{-1}$, the time derivative can be translated into a temperature derivative, yielding

$$\frac{\beta}{H} = T_n \frac{\mathrm{d}}{\mathrm{d}t} \left(\frac{S_3}{T} \right) \bigg|_{T_n}. \tag{1.35}$$

The strength of the transition can be identified with the amount of latent heat released during the process, normalized to the energy density of the thermal bath

$$\rho_r = \frac{\pi^2}{30} g_* T^4. \tag{1.36}$$

This quantity reflects how much the transition deviates from equilibrium and therefore plays a key role in determining its cosmological consequences. The most commonly used definition reads [52, 53]

$$\alpha = \frac{1}{\rho_r} \left(\Delta V - \frac{T}{4} \Delta \frac{\mathrm{d}V}{\mathrm{d}T} \right) \bigg|_{T_n}, \tag{1.37}$$

where Δ denotes the difference between the symmetric and broken phases. Although alternative definitions can be found in the literature [40], the expression above captures

the essential thermodynamic content of the transition. In particular, in hydrodynamic treatments of bubble expansion, a commonly used alternative definition of α is based on the trace of the energy-momentum tensor of the plasma [1, 54]. For an ideal fluid with a radiation-like equation of state, this formulation is equivalent to the one given above.

The parameters α and β, together with the bubble-wall velocity v_w discussed in the following chapters, play a central role in predicting the resulting gravitational wave spectrum. In particular, α determines the energy budget available for sourcing gravitational waves, while β^{-1} sets the characteristic time scale of the emission process. Additionally, the nucleation temperature T_n determines the redshift of the signal and therefore affects the peak frequency of the spectrum observed today.

1.6 Hubble-induced phase transitions

So far, we have discussed the theory of thermally induced phase transitions, in which the barrier between vacua typically arises from thermal corrections to the effective potential. In such scenarios, tunnelling becomes efficient as the Universe cools down, with the characteristic energy scale set by the nucleation temperature.

In this section, we turn to a qualitatively different mechanism that goes beyond the standard thermal picture. Here, the transition is not triggered by temperature, but by the evolution of the Hubble rate in the early Universe. In particular, the nucleation of true-vacuum bubbles is driven by the changing spacetime curvature following the end of inflation, which modifies the effective scalar potential via a non-minimal coupling to gravity. As the Hubble rate decreases, the potential barrier may vanish or become sufficiently suppressed to enable bubble nucleation. This idea was originally proposed in [6] and has since been developed further in [55, 56].

We consider a minimal setup comprising two scalar fields: the inflaton, which governs the expansion of the Universe during and immediately after inflation, and a subdominant spectator field. Such spectator scalars are common in extensions of the Standard Model and here are assumed to be non-minimally coupled to gravity. This curvature coupling provides a natural mechanism for the field to track the cosmic evolution, effectively acting as a clock. In particular, the curvature-induced mass correction

dynamically reshapes the effective potential, potentially triggering a first-order phase transition. Importantly, this occurs during the post-inflationary kinetic domination epoch, when the inflaton's kinetic energy dominates the total energy density.

As a concrete example, we consider a scalar field χ described by the action [57–59]

$$S = \int d^4x\sqrt{-g}\left[\frac{M_P^2 - \xi\chi^2}{2}\mathcal{R} - \frac{1}{2}\partial_\mu\chi\partial^\mu\chi - \frac{m^2}{2}\chi^2 + \frac{\sigma}{3}\chi^3 - \frac{\lambda}{4}\chi^4\right], \tag{1.38}$$

where $M_P = 2.435 \times 10^{18}$ GeV is the reduced Planck mass, ξ is the non-minimal coupling, and $\mathcal{R}$ is the Ricci scalar. The parameters m, σ, and λ are the mass, cubic, and quartic self-interaction couplings of χ, respectively. For physical consistency, all parameters are taken to be real and positive.

For a spatially flat FLRW metric, the Ricci scalar is given by

$$\mathcal{R} = 3(1 - 3w)H^2, \tag{1.39}$$

where $w = p/\rho$ is the equation of state parameter of the dominant cosmic fluid. Since the spectator field χ is assumed to remain subdominant during the early post-inflationary evolution, it does not influence the background dynamics and hence the value of w. Under this assumption, the non-minimal coupling term leads to an effective mass correction for χ, allowing us to write the effective potential as

$$V_{\text{eff}}(\chi) = \frac{M^2}{2}\chi^2 - \frac{\sigma}{3}\chi^3 + \frac{\lambda}{4}\chi^4, \qquad \text{with} \qquad M^2 = m^2 + \xi\mathcal{R}\,. \tag{1.40}$$

From the relation for the Ricci scalar given in eq. (1.39), it is clear that an increasing EoS parameter leads to a decreasing effective mass. For $0 < M^2 < 2\sigma^2/(9\lambda)$, the effective potential in eq. (1.40) exhibits a false vacuum at $\chi = 0$ and a true vacuum at

$$\chi_{\text{tv}} = \frac{\sigma}{2\lambda}\left(1 + \sqrt{1 - \frac{4M^2\lambda}{\sigma^2}}\right). \tag{1.41}$$

The existence of two distinct vacua sets the stage for a first-order phase transition after inflation. During slow-roll inflation, the inflaton's kinetic energy is negligible with $w = -1$, corresponding to a nearly constant Hubble parameter. As inflation ends, the inflaton begins to roll towards its minimum, and w reaches 1. Lastly, we consider the period of kinetic domination after inflation.

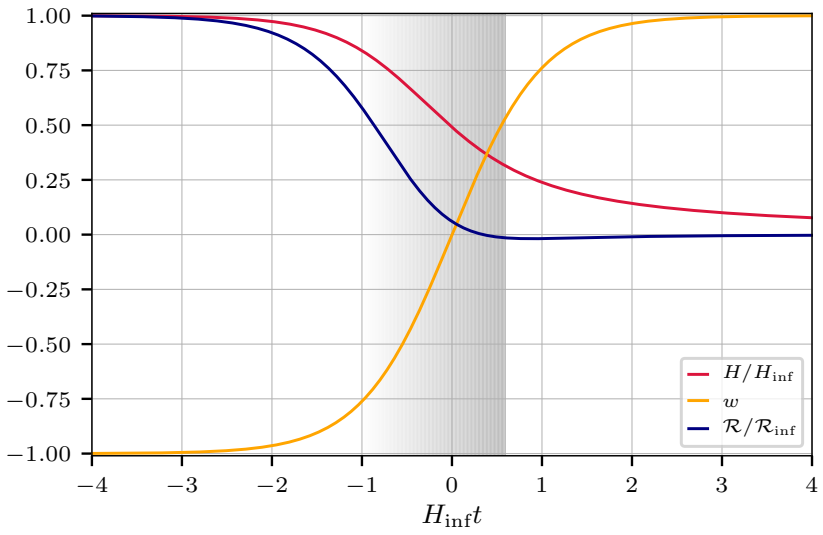

Figure 1.4: *Evolution of the equation of state parameter w, the Hubble rate H and the Ricci scalar $\mathcal{R}$ from inflation to kination. The rate of change is set to $\beta_w/H_{\rm inf} = 1$. The shaded area denotes the period in which a FOPT can naturally occur.*

To simplify the calculations, we model the evolution of the global equation of state parameter using a smooth transition function:

$$w(t) = \tanh\left(\beta_w(t - t_0)\right), \tag{1.42}$$

where t_0 denotes the reference time at which $w = 0$ and the free parameter $\beta_w > 0$ controls the speed of the transition between inflation and kination.

The corresponding Hubble parameter reads

$$H(t) = \left[\frac{3}{2}\left(t + \frac{1}{\beta_w}\ln\left[\cosh\left(\beta_w(t - t_0)\right)\right] + c\right)\right]^{-1}, \tag{1.43}$$

where the integration constant is $c = \frac{2}{3H_{\rm inf}} + \frac{\ln 2}{\beta_w} - t_0$ and $H_{\rm inf} = H(t \to -\infty)$ denotes the inflationary Hubble scale. Expressed in units of $H_{\rm inf}$, the time evolution becomes

$$\frac{H(t)}{H_{\rm inf}} = \frac{2}{3}\left(H_{\rm inf}(t - t_0) + \left(\frac{\beta_w}{H_{\rm inf}}\right)^{-1}\ln\left[2\cosh\left(\left(\frac{\beta_w}{H_{\rm inf}}\right)H_{\rm inf}(t - t_0)\right)\right] + \frac{2}{3}\right)^{-1}. \tag{1.44}$$

The time evolution of the Hubble parameter $H(t)$, the equation of state $w(t)$, and the Ricci scalar $\mathcal{R}(t)$ across the transition from inflation to kination is shown in Fig. 1.4. The shaded region indicates the epoch during which the effective mass term becomes negative, marking the window in which the first-order phase transition can be triggered.

The technical details of computing the parameters that characterize the Hubble-induced phase transition, such as the nucleation rate, the Euclidean action, and the bubble profile, are comprehensively discussed in the original work [6]. We provide there a semi-analytical framework to evaluate the tunnelling process in a time-dependent cosmological background, employing the thin-wall approximation tailored to the post-inflationary epoch. The study also investigates the resulting gravitational wave signal from bubble-wall collisions across various inflationary scales $H_{\rm inf}$, showing that low-scale inflation scenarios may lead to detectable signals in future gravitational wave observatories.

Our analysis represents a first step towards quantitatively understanding expansion-driven phase transitions. Several directions for refinement remain open. In particular, the assumption of a negligible flat-space mass m simplifies the dynamics, making the evolution controlled primarily by the non-minimal coupling ξ and the parameter β_w. If m is appreciable, it could delay the nucleation epoch and lead to slower transitions. Moreover, the formalism can be generalized to accommodate more complex scalar sectors, non-trivial gravitational couplings, and a variety of inflationary histories. These extensions open up novel pathways for connecting the physics of early-Universe phase transitions with potential observational signatures.

1.7 Production of gravitational waves

As described in the previous sections, cosmological first-order phase transitions proceed through the nucleation and expansion of bubbles corresponding to a more energetically favourable phase. When these bubbles grow and collide, they source substantial inhomogeneities in the energy-momentum tensor. These disturbances are subsequently imprinted in the spacetime metric as stochastic gravitational waves, which may be observable today as a relic signal from the early Universe.

The production of gravitational waves from such transitions has been extensively studied in the literature [40, 47, 51, 60–62]. Three primary mechanisms have been identified as the dominant sources of the GW signal:

1. Collisions of the vacuum bubble walls,

2. Sound waves in the primordial plasma,

3. Turbulent motion of the primordial plasma.

Which of these mechanisms contributes most significantly depends on the dynamics of the bubble walls during the transition. If the expansion is stationary, most of the released latent heat is efficiently transferred to the surrounding primordial plasma. In this regime, the main sources of GWs are the resulting sound waves and the turbulent motion, however the latter one is typically subdominant.

In contrast, if the friction acting on the bubble walls is insufficient to counterbalance the vacuum pressure difference, the walls can continuously accelerate, approaching ultra-relativistic speeds. This so-called runaway regime leads to most of the latent heat being converted into the kinetic energy of the bubble walls themselves, making bubble collisions the dominant source of gravitational radiation.

The resulting GW spectra differ between these regimes and can often be modelled as broken or double-broken power laws. Their shape and amplitude are governed by several key parameters of the transition, introduced in Section 1.5, including the strength of the transition α, its inverse duration β/H_*, the temperature T_* at which the transition completes (which, for moderately strong transitions, can be identified with the nucleation temperature T_n), and the bubble-wall velocity v_w.

Following the conventions and parametrizations established in [47], we now present a template framework to estimate the gravitational wave signal, focusing on the sound-wave contribution, which dominates for non-runaway and moderately strong transitions. We illustrate the predicted spectra for a set of representative benchmark parameters relevant to our model.

The stochastic gravitational wave background generated by sound waves can be described by the following expression:

$$h^2\Omega_{\rm GW}(f,\vec{\theta}) = h^2\Omega_{\rm int}(\vec{\theta}) \times S(f), \tag{1.45}$$

where $h^2\Omega_{\rm int}$ denotes the model-dependent amplitude that encapsulates the physical parameters of the transition (collectively denoted by $\vec{\theta}$), and $S(f)$ describes the spectral shape of the signal:

$$S(f) = N \left(\frac{f}{f_1}\right)^{n_1} \left[1 + \left(\frac{f}{f_1}\right)^{a_1}\right]^{\frac{-n_1+n_2}{a_1}} \left[1 + \left(\frac{f}{f_2}\right)^{a_2}\right]^{\frac{-n_2+n_3}{a_2}}. \tag{1.46}$$

The normalization factor N is fixed by the condition $\int_{-\infty}^{\infty} S(f)\,\mathrm{d}(\log f) = 1$ and the spectral slopes are chosen to match the results from hydrodynamic simulations:

$$n_1 = 3 \qquad n_2 = 1 \qquad n_3 = -3 \qquad a_1 = 2 \qquad a_2 = 4.$$

The two characteristic frequencies f_1 and f_2 correspond to the peak and the high-frequency break of the spectrum, respectively, and are given by:

$$f_1 \simeq 0.2 H_{*,0}(H_* R_*)^{-1} \qquad \text{and} \qquad f_2 \simeq 0.5 H_{*,0} \Delta_w^{-1}(H_* R_*)^{-1}, \tag{1.47}$$

where $\Delta_w = \xi_{\mathrm{shell}}/\max(v_w, c_s)$ and ξ_{shell} represents the comoving sound shell thickness, while c_s is the speed of sound in the plasma.

The Hubble parameter at the time of GW production, redshifted to today, is approximated as

$$H_{*,0} \approx 1.65 \times 10^{-5}\,\mathrm{Hz} \left(\frac{g_*}{100}\right)^{\frac{1}{6}} \left(\frac{T_*}{100\ \mathrm{GeV}}\right), \tag{1.48}$$

with the effective number of relativistic degrees of freedom at the end of the transition g_*. Finally, the characteristic bubble size R_* is related to the transition time scale via:

$$H_* R_* = (8\pi)^{\frac{1}{3}} \max(v_w, c_s) \left(\frac{\beta}{H_*}\right)^{-1}. \tag{1.49}$$

This relation follows from the sound shell model and captures the typical scale over which coherent acoustic perturbations are generated.

To estimate the integrated amplitude of the gravitational wave spectrum sourced by sound waves, one can use the following parametric expression:

$$h^2 \Omega_{\mathrm{int}} = h^2 F_{\mathrm{GW},0} A_{\mathrm{sw}} K^2 (H_* \tau_{\mathrm{sw}})(H_* R_*), \tag{1.50}$$

where $A_{\mathrm{sw}} \approx 0.11$ is a numerical factor derived from simulations, and $h^2 F_{\mathrm{GW},0}$ accounts for the redshift of the gravitational wave energy density to today:

$$h^2 F_{\mathrm{GW},0} \approx 1.64 \times 10^{-5} \left(\frac{100}{g_*}\right)^{\frac{1}{3}}. \tag{1.51}$$

The efficiency factor K quantifies the fraction of the vacuum energy that is converted into bulk motion of the plasma and is approximately given by

$$K \approx 0.6 \frac{\kappa\alpha}{1+\alpha}, \tag{1.52}$$

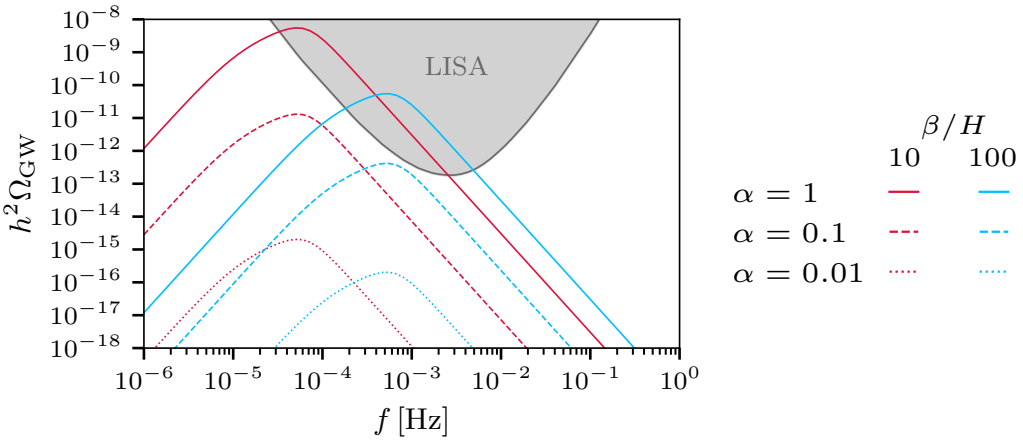

Figure 1.5: *Representative gravitational wave spectra from sound waves for various values of the transition strength α and the inverse time duration β/H. The gray shaded region indicates the parameter space where the signal is expected to be observable by LISA with a signal-to-noise ratio SNR ≥ 10.*

with κ being the efficiency of kinetic energy transfer for a single bubble (see [31, 54, 63] for detailed treatments).

The amplitude is additionally reduced by the finite duration of the source $\tau_{\rm sw}$. If the acoustic source operates for less than a Hubble time, the gravitational wave amplitude is correspondingly suppressed. The effective duration is therefore given by:

$$H_*\tau_{\rm sw} = \min(H_*\tau_{\rm sw}, 1), \qquad \text{with} \qquad H_*\tau_{\rm sw} = H_* R_* / \sqrt{\bar{v}_f^2}, \tag{1.53}$$

where the effective squared fluid velocity is related to the kinetic energy as $\bar{v}_f^2 = \frac{3}{4}K$.

The detectability of a stochastic gravitational wave background by a given experiment is quantified using the signal-to-noise ratio (SNR). For a background with energy density spectrum $h^2\Omega_{\rm GW}$ observed over time $T_{\rm obs}$, the SNR is defined as

$$SNR = \sqrt{T_{\rm obs} \int_{f_{\rm min}}^{f_{\rm max}} \mathrm{d}f \left(\frac{h^2\Omega_{\rm GW}}{h^2\Omega_{\rm sens}} \right)^2}, \tag{1.54}$$

where $h^2\Omega_{\rm sens}$ denotes the effective sensitivity curve of the detector. The construction of the LISA sensitivity curve used in our analysis is described in Appendix A.

In Figure 1.5, we present several examples of gravitational wave spectra originating from cosmological first-order phase transitions, calculated for representative benchmark parameters. These spectra are compared against the LISA sensitivity threshold corre-

sponding to $SNR = 10$, illustrating the potential detectability of such signals in the upcoming space-based interferometer era.

CHAPTER 2

Cosmological phase transitions in the real scalar singlet extension of the Standard Model

In the Standard Model, electroweak symmetry breaking proceeds through a smooth crossover, which is insufficient to account for the observed baryon asymmetry of the Universe. This asymmetry requires out-of-equilibrium processes during the early Universe, as outlined by Sakharov's conditions [24], which can naturally be realized in scenarios with a first-order electroweak phase transition. Such transitions, apart from offering a viable framework for electroweak baryogenesis, also have the potential to generate a stochastic background of gravitational waves. Their detection in future observatories would thus serve as a powerful probe of physics beyond the Standard Model. Importantly, first-order phase transitions arise generically in a wide class of SM extensions.

Probably the simplest and most extensively studied extension of the Standard Model that allows for a strong first-order electroweak phase transition is the real scalar singlet model (xSM) [4, 64–80]. In this scenario, the Standard Model Higgs doublet H is supplemented by an additional real scalar field s. If the mixing between the singlet and the Higgs is forbidden by a Z_2 symmetry of the scalar potential, the singlet scalar becomes stable. This stability makes the singlet a natural dark matter candidate,

offering a predictive and minimal framework, where the relic abundance compatible with cosmological observations can be obtained in the large part of the parameter space, although not in regions that simultaneously allow for strong FOPT [75, 81].

In this chapter, we explore the properties of the model in the context of cosmological first-order phase transitions. The analysis of their dynamics builds upon the formalism introduced in the previous chapter. Beginning with the tree-level scalar potential, we include thermal corrections and investigate the resulting vacuum structure and phase transition patterns. This enables us to constrain the relevant parameter space and extract the characteristic transition parameters within the phenomenologically interesting region. Given the relatively weak experimental constraints on this model from current and future collider searches, which are briefly discussed below, we then shift our focus to its cosmological implications, particularly the predictions for gravitational wave signals originating from the early Universe.

Our approach partially follows the methods and results presented in Ref. [4], though we adopt a simplified form of the thermal potential to facilitate later use of the selected points in numerical simulations of bubble expansion (see Chapter 4). The results of these parameter space scans, along with benchmark points, have already been employed in studies of bubble-wall velocities in both local thermal equilibrium and beyond [2, 3].

2.1 Effective potential of the xSM model

The theory under consideration is defined by the Lagrangian

$$\mathcal{L} = (\partial_\mu H)^\dagger(\partial^\mu H) + (\partial_\mu s)(\partial^\mu s) + V_0(H, s), \tag{2.1}$$

where $H = (G^+, \frac{h+iG^0}{\sqrt{2}})^T$ denotes the Standard Model Higgs doublet and s is the additional real scalar singlet. The singlet is assumed to respect a Z_2 symmetry and to couple to the SM fields exclusively via the Higgs portal. Consequently, the tree-level scalar potential takes the form

$$V_0(H, s) = \mu_h^2 H^\dagger H + \lambda_h (H^\dagger H)^2 + \frac{1}{2}\lambda_{hs}(H^\dagger H)s^2 + \frac{1}{2}\mu_s^2 s^2 + \frac{1}{4}\lambda_s s^4. \tag{2.2}$$

Rewriting the potential in the unitary gauge, one obtains

$$V_0(h, s) = \frac{1}{2}\mu_h^2 h^2 + \frac{1}{4}\lambda_h h^4 + \frac{1}{4}\lambda_{hs} h^2 s^2 + \frac{1}{2}\mu_s^2 s^2 + \frac{1}{4}\lambda_s s^4, \tag{2.3}$$

where h and s are the only remaining dynamical scalar degrees of freedom. The mass parameter for the Higgs μ_h and the quartic coupling λ_h are fixed such that the electroweak vacuum at the zero-temperature is located at $(h, s) = (v, 0)$ with $v = 246.2$ GeV. This requirement leads to the condition

$$\left.\frac{\partial V_0(h,s)}{\partial h}\right|_{(v,0)} = 0 \quad \Longrightarrow \quad \mu_h^2 = -\lambda_h v^2. \tag{2.4}$$

The elements of the scalar mass matrix are given by

$$M_{hh}^2 = \left.\frac{\partial^2 V_0(h,s)}{\partial h^2}\right|_{(v,0)} = \mu_h^2 + 3\lambda_h v^2 \tag{2.5a}$$

$$M_{hs}^2 = \left.\frac{\partial^2 V_0(h,s)}{\partial h \partial s}\right|_{(v,0)} = 0 \tag{2.5b}$$

$$M_{ss}^2 = \left.\frac{\partial^2 V_0(h,s)}{\partial s^2}\right|_{(v,0)} = \mu_s^2 + \frac{\lambda_{hs} v^2}{2}, \tag{2.5c}$$

and thus the physical masses are

$$m_h^2 = 2\lambda_h v^2 \qquad \text{and} \qquad m_s^2 = \mu_s^2 + \lambda_{hs}\frac{v^2}{2} \tag{2.6}$$

with the Higgs boson mass fixed to $m_h = 125.09$ GeV [82]. This leaves the scalar singlet mass m_s, its quartic self-coupling λ_s and the portal coupling λ_{hs} as the remaining three free parameters of the model.

To study the temperature-dependent vacuum structure of the theory, thermal corrections to the potential must be included. The effective potential is then defined as

$$V_{\text{eff}}(h, s, T) = V_0(h, s) + \sum_i \frac{n_i T^4}{2\pi^2} J_{b/f}\left(\frac{m_i(h,s)}{T}\right), \tag{2.7}$$

where the sum runs over all particle species in the model. For each species, n_i is the number of degrees of freedom, $m_i(h, s)$ is the field-dependent mass, and $J_{b/f}$ denotes the bosonic or fermionic thermal function defined in eq. (1.21). In principle, one-loop quantum corrections, known as the Coleman-Weinberg potential, should also be included. However, this term is neglected here since it does not qualitatively change the shape of the potential and does not play a significant role in modelling bubble expansion, which is the main focus of this work. Including the full one-loop potential would only result in a slight shift in the values of the singlet couplings, without changing the overall conclusions drawn from the following results.

At temperatures around the electroweak scale, most Standard Model species are light ($m \ll T$), making the high-temperature expansion (1.22) a good approximation of the full potential. Under this assumption, eq. (2.7) simplifies to

$$V_{\text{eff}}(h, s, T) \approx V_0(h, s) - \frac{g_* \pi^2}{90} T^4 + \sum_i \frac{c_i n_i}{24} m_i^2(h, s) T^2 \tag{2.8}$$

where $c_i = 1/2$ for fermions and $c_i = 1$ for bosons. The parameter $g_*(T)$ denotes the effective number of relativistic degrees of freedom, given by

$$g_*(T) = \sum_{i \in \text{bosons}} g_i \left(\frac{T_i}{T}\right)^4 + \sum_{i \in \text{fermions}} \frac{7}{8} g_i \left(\frac{T_i}{T}\right)^4 . \tag{2.9}$$

In practice, we use the temperature-dependent parametrization of $g_*(T)$ proposed in Ref. [83], which provides a smooth interpolation based on the particle content of the Standard Model across the relevant temperature range. Finally, the complete effective potential of the model can be written in a compact form as

$$V_{\text{eff}}(h, s, T) = -\frac{g_* \pi^2}{90} T^4 + \frac{1}{2}\mu_h^2(T) h^2 + \frac{1}{4}\lambda_h h^4 + \frac{1}{4}\lambda_{hs} h^2 s^2 + \frac{1}{2}\mu_s^2(T) s^2 + \frac{1}{4}\lambda_s s^4 . \tag{2.10}$$

The temperature-dependent mass terms are now given by

$$\mu_h^2(T) \coloneqq \mu_h^2 + c_h^2 T^2 \qquad \text{and} \qquad \mu_s^2(T) \coloneqq \mu_s^2 + c_s^2 T^2 \tag{2.11}$$

with

$$c_h^2 = \frac{1}{48}\left(9g^2 + 3g'^2 + 12y_t^2 + 24\lambda_h + 2\lambda_{hs}\right) \qquad \text{and} \qquad c_s^2 = \frac{1}{12}\left(2\lambda_{hs} + 3\lambda_s\right), \tag{2.12}$$

where g and g' are electroweak couplings and y_t is the Yukawa coupling for the top quark. This approximate parametrization of the effective potential has been widely used in the literature to study the dynamics of this model, see for example [73, 84].

2.2 Vacuum structure and transition scheme

Having established the form of the temperature-dependent effective potential, we now turn to the analysis of the vacuum structure and the associated phase transition. This step is essential to determine whether and under what conditions the model exhibits a first-order electroweak phase transition. The behaviour of the potential as the Universe

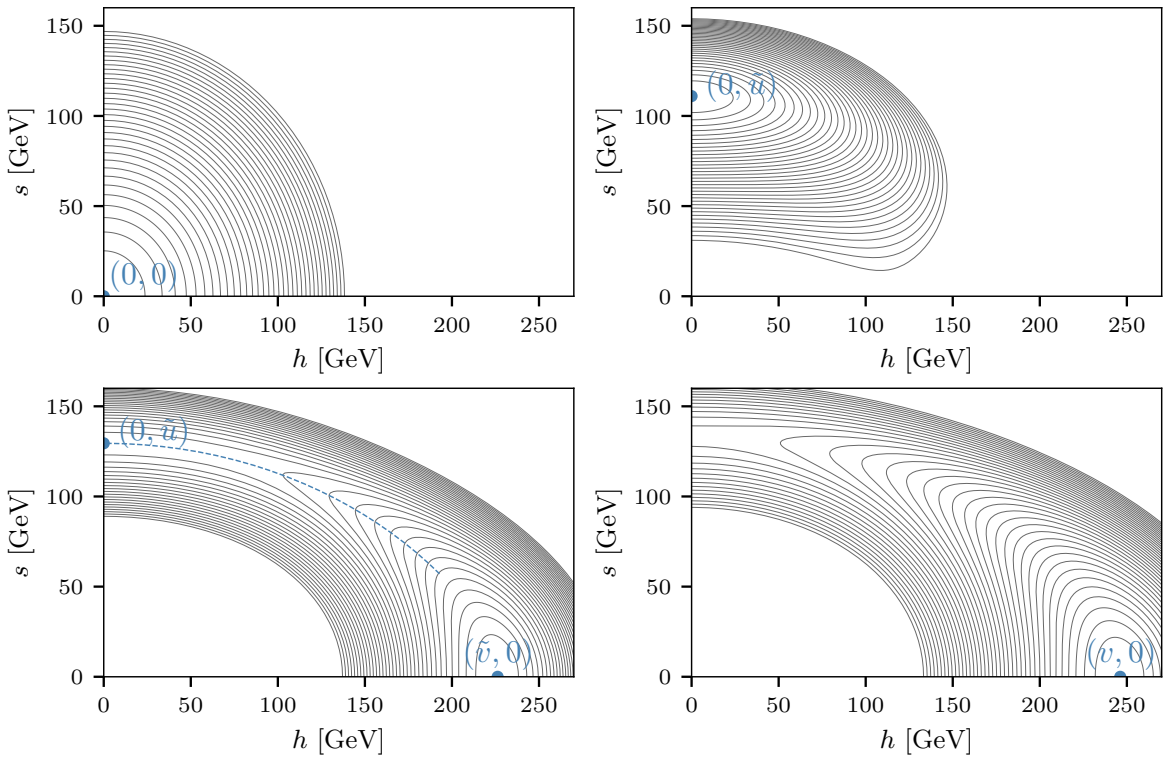

Figure 2.1: *Thermal evolution of the two-dimensional effective potential and the corresponding configuration of the fields for the benchmark realization of the xSM model. Different panels show the subsequent stages of the phase transition. The positions of the minima are denoted by blue dots, and the tunneling path is represented by the dashed curve. Detailed descriptions of each stage of the phase transition can be found in the main text.*

cools, as well as the key stages of the phase transition are illustrated in Fig. 2.1, where successive panels correspond to decreasing temperatures. The thermal history of the system can be summarised as follows:

1. At very high temperatures, the symmetry of the theory is restored, and the effective potential exhibits a single minimum located at the origin, $(h, s) = (0, 0)$ (see the first panel of Fig. 2.1).

2. As the temperature decreases, the minimum gradually shifts along the s direction. This stage of the vacuum evolution proceeds smoothly and is referred to as a crossover. In the context of a two-step phase transition, it is commonly identified as the first step (see the second panel of Fig. 2.1).

3. At a certain point, a second minimum appears along the h direction and becomes progressively deeper as the temperature drops. At the critical temperature T_c, both minima are energetically degenerate. Below this value, the electroweak-like vacuum at $(h, s) = (\tilde{v}, 0)$ becomes energetically preferred. At the nucleation temperature $T_n < T_c$, thermal tunnelling between the two minima occurs along a path of least Euclidean action (indicated by the dashed blue line in the third panel of Fig. 2.1). It is important to note that the tunnelling typically ends at a point shifted from the true vacuum due to the potential barrier and energy difference between the minima. For the mathematical details of tunnelling process see Chapter 1.

4. As the Universe continues to cool, the system evolves toward the true electroweak vacuum located at $(h, s) = (v, 0)$, which corresponds to the present-day configuration (see the fourth panel of Fig. 2.1).

The two-step phase transition pattern described above can only be realised within a restricted region of the parameter space. First, the symmetry breaking in the singlet direction must precede that in the Higgs direction. This requirement, when applied to the temperature-dependent mass parameters defined in eq. (2.12), yields the condition

$$\frac{\mu_s^4}{c_s^2} > \frac{\mu_h^4}{c_h^2}. \tag{2.13}$$

Secondly, in order for the electroweak minimum at $(h, s) = (v, 0)$ to be the true vacuum of the theory at zero temperature, the potential at this point must be lower than in the singlet direction. This leads to the constraint

$$\frac{\mu_h^4}{\lambda_h} > \frac{\mu_s^4}{\lambda_s}. \tag{2.14}$$

Finally, during the tunnelling process, the false vacuum $(0, \tilde{u})$ must constitute a local minimum of the potential. At the critical temperature T_c, this translates into the inequality

$$\lambda_{hs} > 2\sqrt{\lambda_h \lambda_s}, \tag{2.15}$$

which becomes even more stringent at lower temperatures, particularly at the nucleation temperature $T_n < T_c$.

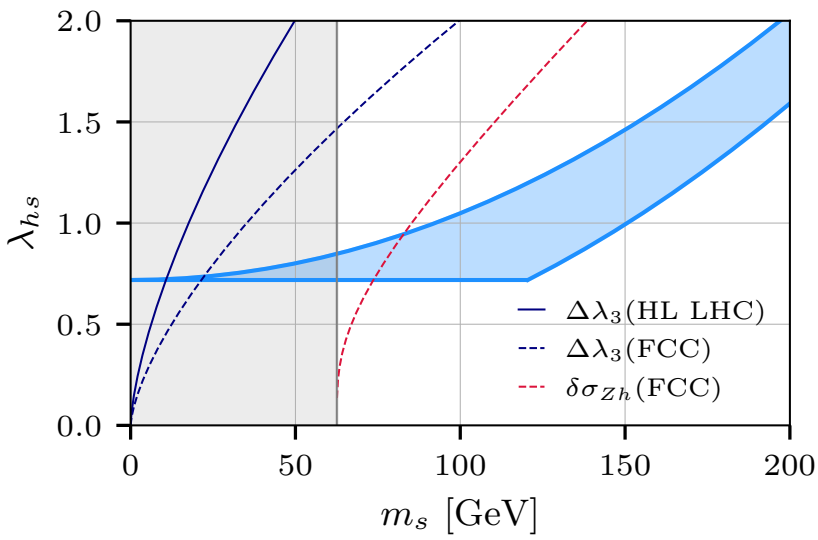

Figure 2.2: *The parameter space of the xSM model for a benchmark value of the singlet quartic coupling $\lambda_s = 1$. The light blue region indicates where a two-step first-order phase transition can occur. The gray area, corresponding to $m_s < m_h/2$, is excluded by LHC bounds on the Higgs invisible decay width. The dark blue lines show the projected sensitivity to deviations in the Higgs self-coupling at the HL-LHC (solid) and FCC (dashed), while the red dashed line corresponds to the projected FCC sensitivity to the associated Zh production cross section.*

In principle, the portal coupling λ_{hs} and the singlet self-coupling λ_s are not subject to upper bounds from the structure of the potential itself. However, to ensure the perturbative validity of the theory, we impose the condition that both couplings remain within the perturbative regime:

$$\lambda_s,\ \lambda_{hs} \leq 4\pi. \tag{2.16}$$

In practice, we remain well below this upper limit, as values approaching 4π may lead to a breakdown of perturbativity and require careful treatment of higher-order corrections.

The region of the parameter space satisfying all three conditions (2.13), (2.14) and (2.15) for the benchmark choice $\lambda_s = 1$ is illustrated in Fig. 2.2 with light blue shading. Experimental bounds displayed in the figure will be discussed in the subsequent part of this chapter.

Note that not all points in the previously discussed parameter space lead to a successful completion of a first-order phase transition. In particular, for large values of the

portal coupling λ_{hs}, the tunnelling rate can become extremely suppressed, at very low temperatures, causing the Universe to remain trapped in the false vacuum or preventing the transition from completing if the bubbles of the true vacuum fail to percolate. To accurately determine whether a given parameter choice results in a completed transition, and to extract the relevant properties of the transition, a detailed scan of the parameter space is required. This will be the focus of the following section.

2.3 Scan of the parameter space

To prepare a sample for our study we performed a scan over the scalar singlet mass m_s and the portal coupling λ_{hs} fixing the quartic coupling to $\lambda_s = 1$. The scan was conducted using the `CosmoTransitions` package [85], which allows for the calculation of key quantities governing the phase transition dynamics.

For each point of the parameter space, we determine the critical temperature T_c and the nucleation temperature T_n, as well as the transition strength α and characteristic time scale β/H. We also evaluate the steady-state velocity of the expanding bubble v_w, assuming local thermal equilibrium. The detailed discussion of v_w will follow in the next chapters.

The relevant part of the parameter space has the following structure: for a given singlet mass m_s, stronger transitions tend to correspond to larger values of the portal coupling λ_{hs}. The level of supercooling T_n/T_c is also correlated with the latent heat, as the lowest temperature ratios correspond to the strongest transitions.

As we are interested in moderately-strong phase transitions, we restrict the scan to values of the transition strength where $\alpha < 1$. This cut ensures that the assumption of radiation domination, which is crucial for the model's consistency, is not violated during the phase transition. In this range of α there is no need to consider the percolation temperature separately, as the transition is assumed to occur almost instantaneously at T_n.

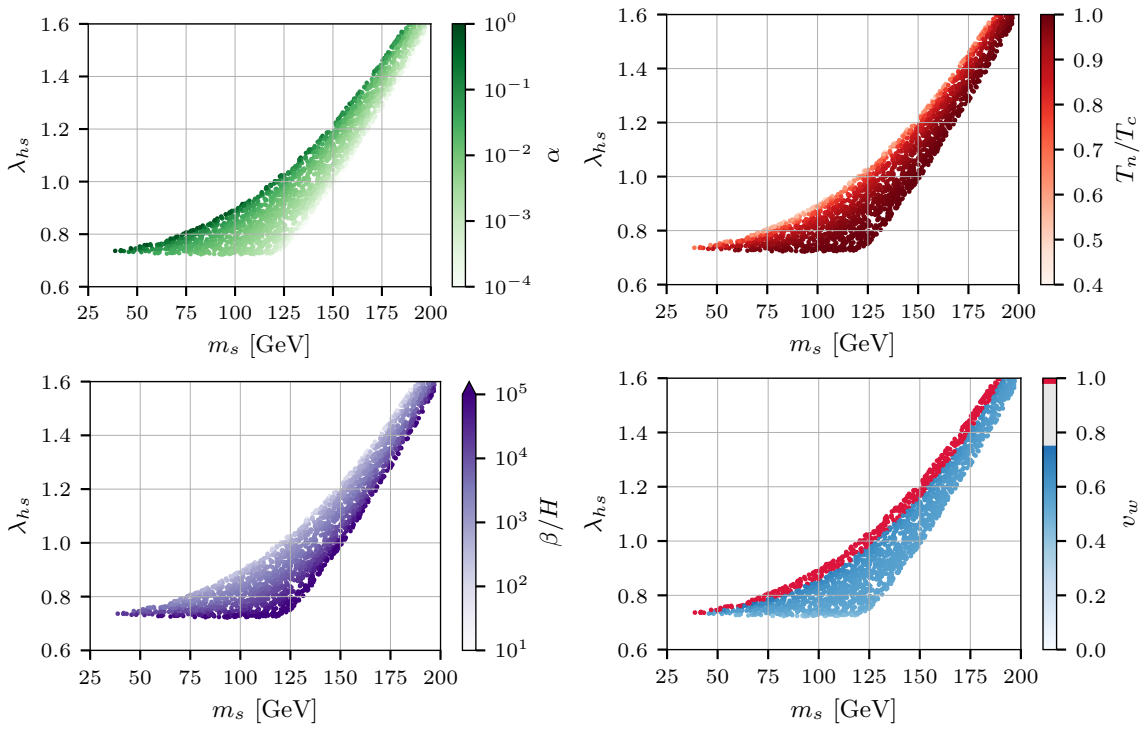

Figure 2.3: *Transition strength α, supercooling ratio T_n/T_c, characteristic time scale β/H, and bubble-wall velocity in the LTE approximation v_w as function of the scalar singlet mass m_s, and portal coupling λ_{hs}. The quartic coupling is fixed to $\lambda_s = 1$.*

2.4 Observational prospects

The model discussed here, often referred to as a *nightmare scenario* in the context of collider searches [72], provides a natural, stable candidate for a dark matter particle. Due to the preserved Z_2 symmetry, the singlet does not mix with the SM Higgs boson, which strongly suppresses both direct detection signals and production rates at colliders [86]. This makes experimental verification particularly challenging, as conventional searches relying on Higgs portal interactions become largely ineffective. The only robust constraint arises from measurements of the invisible Higgs decay width by ATLAS and CMS [87, 88], excluding scenarios with $m_s < m_h/2$.

Nonetheless, the model can be indirectly probed through one-loop corrections to the Higgs self-coupling, induced by the portal interaction λ_{hs}, given by [50]

$$\Delta\lambda_3 = \frac{1}{96\pi^2}\frac{\lambda_{hs}^3 v^4}{m_h^2 m_s^2}. \tag{2.17}$$

The projected sensitivities at the 95% confidence level, corresponding to $\Delta\lambda_3 \sim 0.8$ for

HL LHC [89, 90] and $\Delta\lambda_3 \sim 0.2$ for FCC [91], are indicated in Fig. 2.2 with dark blue lines. Another possibility is the precise measurement of the cross section σ_{Zh} for the Higgs production associated with a Z boson for e^+e^- collisions at FCC. The fractional deviation from the SM prediction induced by the Higgs portal coupling λ_{hs} is given with [50, 72]

$$\delta\sigma_{Zh} = \left| \frac{\lambda_{hs}^2 v^2}{64\pi^2 m_h^2} (1 - F\left(\frac{m_h^2}{4m_s^2}\right) \right|, \tag{2.18}$$

where

$$F(\tau) = \frac{\arcsin(\sqrt{\tau})}{\sqrt{\tau(1-\tau)}}. \tag{2.19}$$

The projected 95% confidence level sensitivity of the FCC to the associated production cross section is $\delta\sigma_{Zh} \sim 0.4\%$ [92], and the corresponding constraint is shown in Fig. 2.2 as a red dashed line. Comparable limits could also be obtained from singlet pair production in association with jets via vector boson fusion, as studied in the context of both HL LHC and FCC [72].

As shown in Fig. 2.2, current experimental constraints still leave a large portion of the parameter space open for exploration, particularly in the context of cosmological phase transitions. Altogether, these findings underscore the difficulty of probing the electroweak phase transition in this scenario using collider-based approaches alone, and highlight the importance of future gravitational wave observatories such as LISA as complementary tools to explore the electroweak epoch.

The expected gravitational wave signal generated by first-order phase transitions in the considered scenario is shown in Fig. 2.4. The left panel presents representative spectra for different benchmark points in the parameter space. For clarity, only spectra with a signal-to-noise ratio above unity ($SNR > 1$) are shown. Among them, those corresponding to particularly strong signals with $SNR > 10$ are highlighted in a darker shade. This visual distinction illustrates the range of gravitational wave amplitudes that can be expected across different realizations of the model.

The right panel displays the signal-to-noise ratio computed using eq. (1.54) for each point in the parameter space, assuming the LISA sensitivity curve. While only a subset of the parameter space yields a potentially observable signal, the results indicate that detectable gravitational waves can arise, particularly in the low-mass and large portal coupling regime, where the phase transition tends to be stronger. Note that for strongly

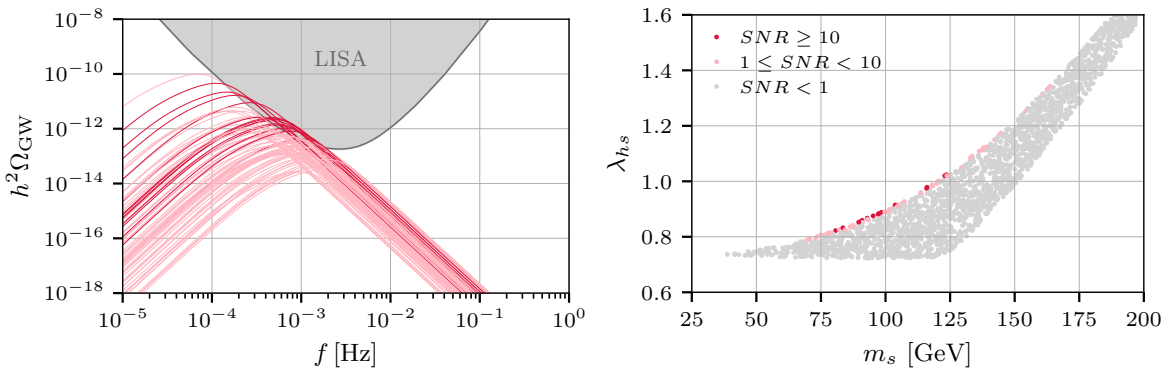

Figure 2.4: ***Left panel:*** *Gravitational wave spectra for different realizations of the model, with spectra for which the signal-to-noise ratio (SNR) exceeds 1 shown for clarity. Darker curves represent spectra with* $SNR > 10$*. The LISA power law sensitivity for* $SNR \geq 10$ *is shown in gray.* ***Right panel:*** *Signal-to-noise ratio (SNR) for each point in the parameter space, computed assuming the LISA sensitivity curve (see Appendix A).*

supercooled transitions, with $\alpha \gg 1$, the signal would be even stronger. However, this regime goes beyond the scope of this work, as in such cases the bubbles always expand as runaways, making their dynamics trivial. This highlights the potential of gravitational wave observations as a complementary probe of the electroweak epoch, especially in scenarios where collider signatures are suppressed. However, for accurate predictions, a precise determination of the transition parameters is crucial. In particular, the accurate modelling of bubble expansion has a significant impact on these results, as faster wall velocities typically lead to larger amplitudes in the spectra, resulting in stronger signals. The study of this dynamics will be the main topic of the remainder of this dissertation.

CHAPTER 3

Hydrodynamic description of expanding bubbles

During a cosmological first-order phase transition, the false vacuum decays through the nucleation of bubbles of the true vacuum, as described in Chapter 1. Once formed, the bubbles rapidly grow, driven by the potential difference between the phases inside and outside the bubble. However, particles in the plasma interacts with the bubble wall, creating an effective friction that slows down the expansion. These opposing effects may reach a balance, resulting in a steady-state evolution with a constant bubble-wall velocity. Otherwise, the bubble wall continues to accelerate, potentially reaching velocities very close to the speed of light. Therefore, to predict the physical observables, it is crucial to correctly evaluate both forces.

The backreaction from the particles interacting with the bubble wall has typically been estimated by solving the Boltzmann equation for all species in the plasma, combined with the equation of motion for the scalar field [4, 5, 29, 32, 33, 93–99]. As these plasma particles are pushed out of equilibrium by the passing wall, the friction force is dominated by those strongly interacting with it. However, this method is technically demanding and the non-equilibrium part of the friction in the equation of motion is instead often parametrized by an effective phenomenological coefficient, which is then treated as a free parameter in hydrodynamic simulations [39, 100].

Recently, it has been shown that purely equilibrium hydrodynamic backreaction

can inhibit acceleration and that the resulting bubble-wall velocity, evaluated within the local thermal equilibrium (LTE) framework, can be estimated in a relatively simple way [30, 31, 34]. This method relies on the conservation of entropy and introduces an additional matching condition relating its value across the bubble wall. Since additional non-equilibrium friction can only further slow down the wall, the LTE result can serve as the upper bound on the full out-of-equilibrium computation. Moreover, studies using the example of a scalar singlet extension of the Standard Model have shown that non-equilibrium corrections are typically subdominant [33].

This chapter focuses on the hydrodynamical description of expanding bubbles, treating the cosmic plasma as a perfect fluid. Following [31], interactions between the bubble wall and the plasma will be separated into equilibrium and non-equilibrium parts, laying the groundwork for both the local thermal equilibrium (LTE) framework and extensions beyond LTE. By introducing the energy-momentum tensor for a perfect fluid and starting from the conservation laws, we derive hydrodynamic equations together with the so-called matching conditions describing the discontinuities of thermodynamic quantities at the bubble front. We discuss the resulting velocity profiles and their physical features. We then explore the LTE approach, where entropy conservation introduces an additional matching condition that determines the steady-state bubble-wall velocity. This part draws heavily from [34], which offers a comprehensive and self-consistent computational framework for the LTE calculations.

Finally, we present the generalised version of the third-matching condition beyond LTE, which constitutes the original result of our work [3]. Assuming a specific class of interactions between the wall and the plasma, valid for the SM and many of its extensions [94, 101], we express the entropy production rate in the thin wall regime using basic physical quantities and the effective friction parameter η [38]. This approach enables the computation of the steady-state wall velocity as a function of the effective friction. Intriguingly, our new formalism typically predicts an additional branch of stable detonation solutions, for which we observe runaway behaviour with $v_w = 1$ in the LTE limit. The existence of this branch provides a useful selection rule to distinguish between physical and unphysical deflagration/hybrid solutions as the faster detonation solution is typically the one that is dynamically realised.

In the last section, we briefly discuss the ballistic approach [7], which allows us to estimate the impact of non-equilibrium effects on particles traversing the wall. Furthermore, recent studies [102] have shown that applying the large-mass limit in this context leads to the maximal entropy production, establishing a lower bound on the wall velocity.

3.1 Equations of motion for the expanding bubble

To describe the dynamics of the growing bubble and estimate the wall velocity, it is essential to evaluate the total force exerted on the wall by the plasma surrounding the bubble and compare it with the driving force coming from the pressure difference between the false and true vacuum. The corresponding equation of motion for the scalar field in the presence of the relativistic plasma is given by [31, 93, 94]

$$\Box\phi + \frac{\partial V_0}{\partial \phi} + \sum_i \frac{\mathrm{d}m_i^2(\phi)}{\mathrm{d}\phi} \int \frac{\mathrm{d}^3 p}{(2\pi)^3 2E_i} f_i(p,x) = 0, \tag{3.1}$$

where the index i runs over all the particle species interacting with ϕ, Here $f_i(p,x)$ represents the particle distribution functions for given species, and E_i denotes the energy of the particles. Additionally, the distribution functions can be separated into equilibrium and non-equilibrium part as follows:

$$f_i(p,x) = f_i^{\mathrm{eq}} + \delta f_i(p,x). \tag{3.2}$$

As shown in Chapter 1, the contribution from the equilibrium part can be interpreted as thermal corrections to the potential. Therefore, the equation of motion can be rewritten as

$$\Box\phi + \frac{\partial V_{\mathrm{eff}}}{\partial \phi} + \sum_i \frac{\mathrm{d}m_i^2(\phi)}{\mathrm{d}\phi} \int \frac{\mathrm{d}^3 p}{(2\pi)^3 2E_i} \delta f_i(p,x) = 0, \tag{3.3}$$

where the effective potential is defined as $V_{\mathrm{eff}}(\phi,T) = V_0(\phi) + V_T(\phi,T)$. Next, assuming a field profile corresponding to a planar bubble wall expanding with constant velocity in the z direction, the above equation can be multiplied by $\mathrm{d}\phi/\mathrm{d}z$ and integrated over z, yielding

$$\int \mathrm{d}z \frac{\mathrm{d}\phi}{\mathrm{d}z} \left(\Box\phi + \frac{\partial V_{\mathrm{eff}}}{\partial \phi} + \sum_i \frac{\mathrm{d}m_i^2(\phi)}{\mathrm{d}\phi} \int \frac{\mathrm{d}^3 p}{(2\pi)^3 2E_i} \delta f_i(p,x) \right) = 0. \tag{3.4}$$

Performing the integration, we obtain the following expression

$$\Delta V_{\text{eff}} = \int \mathrm{d}z \frac{\partial V_{\text{eff}}}{\partial T} \frac{\mathrm{d}T}{\mathrm{d}z} - \sum_i \int \mathrm{d}\phi \frac{\mathrm{d}m_i^2(\phi)}{\mathrm{d}\phi} \int \frac{\mathrm{d}^3 p}{(2\pi)^3 2E_i} \delta f_i(p, x), \tag{3.5}$$

where the left-hand side can be interpreted as the pressure difference between the broken phase inside the bubble and the symmetric phase outside, which drives the expansion. Similarly, the right-hand side corresponds to the backreaction force and can be separated into two parts: the equilibrium plasma contribution from the heated fluid at the bubble front (the first term), and the non-equilibrium dissipative interaction with the species in the plasma (the second term). Neglecting the non-equilibrium part leads to the local thermal equilibrium (LTE) approximation, while parametrizing it allows us to extend the analysis beyond LTE.

3.2 Profiles of the plasma for the stationary states

After identifying the potential sources of interactions that could stop the accelerating expansion, we now focus on the different types of stationary state that can be realised in the system. To do this, we adopt a hydrodynamical approximation, where the plasma of various particle species is modelled as a relativistic perfect fluid. The energy-momentum tensor for such a fluid is given by

$$T^{\mu\nu}_{\text{fluid}} = w u^\mu u^\nu - g^{\mu\nu} p. \tag{3.6}$$

where u^μ represents the four-velocity of the plasma, given with

$$u = (\gamma, v\gamma, 0, 0), \tag{3.7}$$

while p and w are the pressure and the enthalpy, respectively. Conservation of the energy-momentum tensor (3.6) projected onto direction of the flow u^μ and the direction perpendicular to the flow $\bar{u}^\mu$ leads to the following equations:

$$\partial_\mu (u^\mu w) - u_\mu \partial^\mu p = 0, \tag{3.8}$$

$$\bar{u}^\nu u^\mu w \partial_\mu u_\nu - \bar{u}^\nu \partial_\mu p = 0, \tag{3.9}$$

with $\bar{u}_\mu u^\mu = 0$ and $\bar{u}^2 = -1$. In a stationary regime, no characteristic length scale is present. As a result, the solution should depend only on the self-similar variable $\xi = r/t$,

where r is the distance from the centre of the bubble and t is the time since nucleation. For sufficiently large bubbles, the distinct value ξ_w corresponds to the velocity of the bubble wall, while the plasma at the point described by ξ moves with velocity $v(\xi)$. Exploiting this self-similar structure, along with the assumption of spherical symmetry, allows us to derive the following set of equations:

$$(\xi - v)\frac{\partial_\xi e}{w} = 2\frac{v}{\xi} + [1 - \gamma^2 v(\xi - v)]\partial_\xi v, \tag{3.10}$$

$$(1 - v\xi)\frac{\partial_\xi p}{w} = \gamma^2(\xi - v)\partial_\xi v. \tag{3.11}$$

Using the definition of the speed of sound in the plasma, $c \equiv \frac{\mathrm{d}p}{dT}/\frac{\mathrm{d}e}{dT}$, these equations can be combined into hydrodynamic equations that govern the plasma velocity and enthalpy profiles $v(\xi)$ and $w(\xi)$ in the frame of the bubble centre:

$$\begin{aligned} 2\frac{v}{\xi} &= \gamma^2(1 - v\xi)\Big[\frac{\mu^2(\xi, v)}{c^2} - 1\Big]\partial_\xi v, \\ \partial_\xi w &= w\Big(1 + \frac{1}{c^2}\Big)\gamma^2\mu(\xi, v)\partial_\xi v, \end{aligned} \tag{3.12}$$

where $\mu = \frac{\xi - v}{1 - \xi v}$ denotes the Lorentz-transformed fluid velocity. As hydrodynamical flow can develop discontinuities, the conservation of the energy-momentum tensor (3.6) can also be used to derive matching conditions for the thermodynamic quantities in front $(+)$ and behind $(-)$ the bubble front. Under the planar-wall approximation, these conditions take the form

$$w_+\gamma_+^2 v_+ = w_-\gamma_-^2 v_-, \tag{3.13}$$

$$w_+\gamma_+^2 v_+^2 + p_+ = w_-\gamma_-^2 v_-^2 + p_-. \tag{3.14}$$

Note that these relations are defined in in the reference frame of the bubble wall. However, we assume trivial transformation of p and w, while v can be transformed to the plasma rest frame with a simple Lorentz boost.

To proceed further, we need to introduce the equation of state for the plasma. A commonly used choice is the bag model [54, 65], which is given by

$$e_s(T) = a_s T^4 + \epsilon_s \qquad p_b(T) = \frac{1}{3}a_b T^4 - \epsilon_b \tag{3.15}$$

$$e_s(T) = a_s T^4 + \epsilon_s \qquad p_b(T) = \frac{1}{3}a_b T^4 - \epsilon_b, \tag{3.16}$$

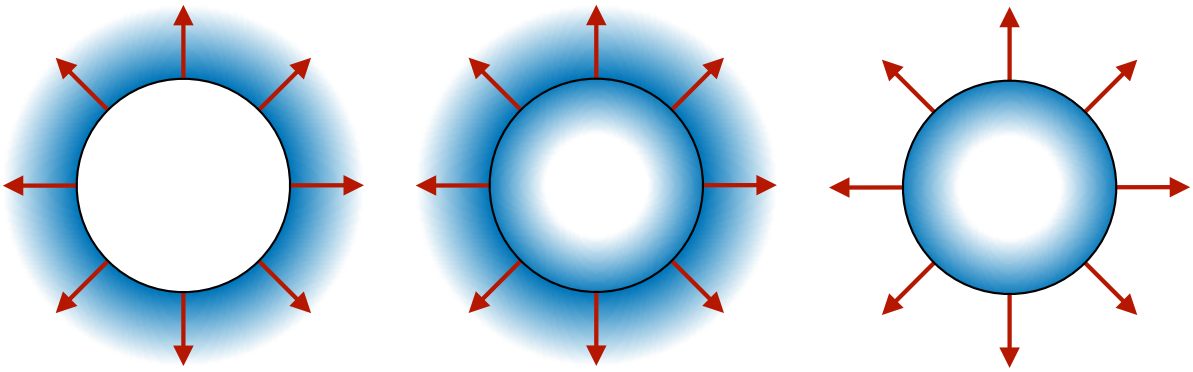

Deflagration: $v_w < c_b$ Hybrid: $c_b < v_w < c_J$ Detonation: $c_J < v_w$

Figure 3.1: *Schematic representation of three different types of expanding bubbles. The colour saturation indicates the plasma velocity with darker colour corresponding to larger values. The black circles represent the position of the bubble wall, while red arrows show the direction of expansion.*

with the subscripts denoting the values in the symmetric (s) and broken (b) phase, however, more complex templates, which allow for different values of the speed of sound, have recently been considered [31, 34] and will be further discussed in this dissertation. Additionally, we introduce the trace of energy-momentum tensor defined as

$$\theta = e - 3p, \tag{3.17}$$

or, taking into account that the speed of sound in the broken phase may differ from the standard value $c_b = 1/\sqrt{3}$ and assuming only a weak dependence on the temperature T [103], the pseudotrace

$$\bar{\theta} = e - \frac{p}{c_b^2}. \tag{3.18}$$

These quantities allow us to define the strength of the transition, without a need to specify the potential, through the relations

$$\alpha_\theta = \frac{\Delta\theta}{3w_s} \qquad \text{and} \qquad \alpha_{\bar{\theta}} = \frac{\Delta\bar{\theta}}{3w_s}, \tag{3.19}$$

where Δ represents the difference between the phases. Unless specified differently, we assume $c_s = c_b = 1/\sqrt{3}$.

Solutions of the hydrodynamic equation (3.12) with the bag-model equation of state depend solely on the transition strength α_θ and bubble-wall velocity in the stationary state, ξ_w. Depending on the terminal velocity of the wall, the expansion can proceed as

subsonic deflagration, supersonic detonation, or as a hybrid possessing features of both types. The velocity at which the shell around the bubble vanishes and the solution shifts from hybrid to detonation is determined by the Chapman-Jouguet condition [4, 34, 104]

$$c_J = \frac{1 + \sqrt{3\alpha_{\bar{\theta}}(1 - c_b^2 + c_b^2\alpha_{\bar{\theta}})}}{1/c_b + 3c_b\alpha_{\bar{\theta}}}. \tag{3.20}$$

Different types of solutions, schematically illustrated in Fig. 3.1, can be characterized as follows:

1. **Deflagrations** are the slowest solutions, with a subsonic bubble-wall velocity $\xi_w < c_b$. In this case, the expanding bubble pushes the plasma in front of it, creating a shell of heated plasma surrounding the bubble. This may locally inverse the hierarchy of minima leading to hydrodynamic obstruction [1, 105]. Behind the wall, the plasma velocity remains unperturbed, implying the condition $v_- = \xi_w$. Additionally, if the bubble wall is fast enough, a supersonic shock front may develop at $\xi_{sh} \gtrsim c_b$ (see Fig. 3.3).

2. **Detonations** are found on the opposite side of the spectrum, with a bubble-wall velocity $\xi_w > c_J$, where c_J is the Jouguet velocity, defined in equation 3.20. In this scenario, the moving wall hits the fluid which remains at rest in front of the bubble. For detonations, the bubble-wall position corresponds to the rarefaction front (a smooth continuation of the shock front), for which $v_+ = \xi_w$. Just behind the wall, $v_- < v_+$, and within the rarefaction front, the velocity gradually slows down, reaching 0 at $\xi = c_b$ (in the plasma reference frame). Note that unlike deflagrations, the overall amplitude of the profile decreases as the wall velocity grows. Due to this fact, stationary detonations are not found in LTE.

3. **Hybrids**, also known as supersonic deflagrations, occur for $c_b < v_w < c_J$. They are constructed as a combination of a deflagration profile with a rarefaction wave characteristic for detonations. The matching conditions are fulfilled with $v_+ < v_- = c_b$. As ξ_w approaches the Jouguet velocity c_J, the profiles become increasingly thinner, with $\xi_w \to \xi_{sh}$. From dynamical perspective, hybrids develop a heated fluid shell similar as for deflagrations, and therefore, these two categories will be often considered together.

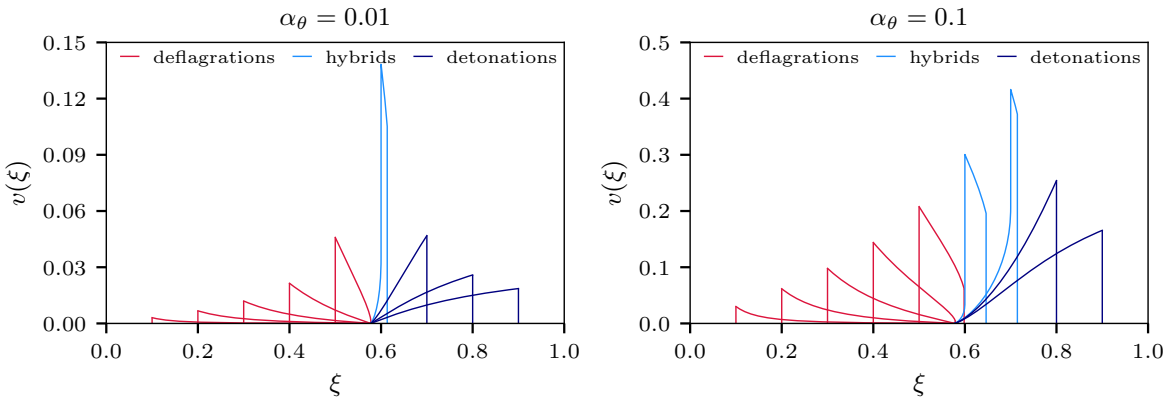

Figure 3.2: *Family of stationary solutions for fluid velocity profiles in the plasma rest frame, shown for benchmark transitions with* $\alpha_\theta = 0.01$ *(left panel) and* $\alpha_\theta = 0.1$ *(right panel). Each profile corresponds to a different wall velocity, with types of solutions indicated by colour.*

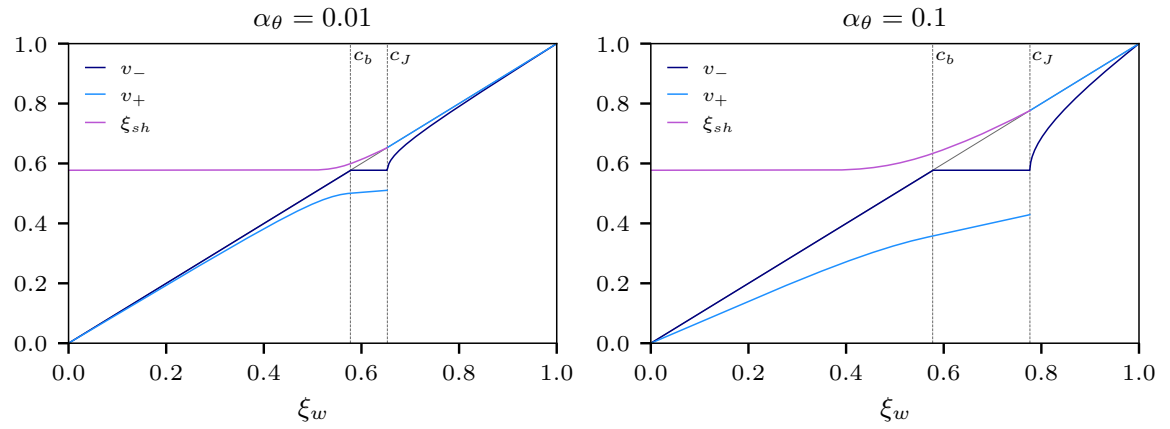

Figure 3.3: *Plasma velocities at the bubble front* v_+ *and* v_- *along with the shock front position* ξ_{sh}*, as function of the wall velocity* ξ_w*, for a benchmark transition with* $\alpha_\theta = 0.01$ *(left panel) and* $\alpha_\theta = 0.1$ *(right panel). Vertical dashed lines represent speed of sound in the plasma* c_b *and the Jouguet velocity* c_J*. Plasma velocities* v_+ *and* v_- *are evaluated in the wall frame.*

The family of solutions, parametrised by the wall velocity ξ_w, for two benchmark transitions with $\alpha_\theta = 0.01$ and $\alpha_\theta = 0.1$ are presented in Fig. 3.2. Meanwhile, Fig. 3.3 illustrates the characteristic velocities v_+ and v_-, along with the position of the shock front ξ_{sh}, as functions of the wall velocity ξ_w. Note that the plasma velocities on both sides of the bubble wall, v_+ and v_-, are defined in the wall frame, while the velocity

profiles in Fig. 3.2 correspond to the plasma rest frame. For a more detailed discussion of the bag model solutions, see [54].

3.3 Bubble-wall velocity in local thermal equilibrium

As previously discussed, the interaction between the bubble wall and the plasma is not solely out-of equilibrium effect. The authors of [105] observed, that pure equilibrium effects can inhibit the accelerating expansion, referring to this phenomenon as hydrodynamic obstruction. This mechanism is based on the fact, that for deflagrations and hybrids, the fluid in front of the bubble is heated, potentially raising the temperature above the critical value. As a result, the hierarchy of the minima is locally inverted, causing the driving force to vanish and leading to stationary expansion. By analysing temperature profiles as a function of the wall velocity, the authors provided simple estimates for its upper and lower bounds.

A thermodynamic approach to estimating interaction strength was proposed in [106], where the authors attempted to relate the pressure difference to changes in entropy density across the wall. This approach turned out to be very fruitful, yielding new thermodynamical constraints on the wall velocity. Further studies concluded, under the assumption of LTE approximation and using using entropy conservation, it is possible to determine the steady-state bubble-wall velocity in a relatively simple manner. The first attempt based, on the bag equation of state [31], has since been extended to a broader class of equations of state and beyond the planar wall limit [34]. Moreover, it has been shown, that the bubble-wall velocity can be estimated using a few parameters evaluated at the nucleation temperature. The key idea is based on the observation, that in local thermal equilibrium, no entropy is produced in the system. This implies that the entropy current remains constant, leading to the condition

$$\partial_\mu (u^\mu s) = 0. \tag{3.21}$$

This requirement must hold across the bubble wall, leading to the third matching relation:

$$s_- \gamma_- v_- = s_+ \gamma_+ v_+, \tag{3.22}$$

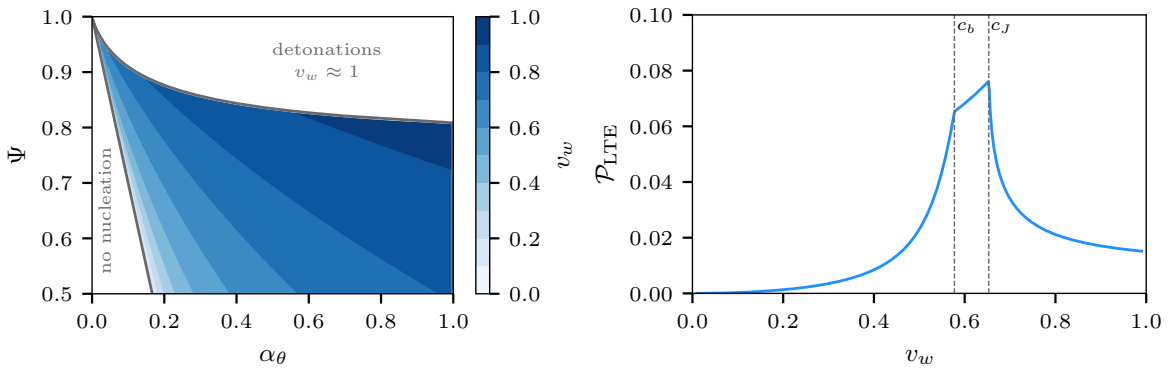

Figure 3.4: ***Left panel:*** *Bubble-wall velocity v_w for deflagration and hybrid solutions as a function of transition strength α_θ and enthalpy ratio Ψ, evaluated using matching condition* (3.22). ***Right panel:*** *Relation between pressure acting on the wall and the wall velocity in local thermal equilibrium, given with* (3.29)*, for a benchmark transition with $\alpha_\theta = 0.01$.*

which can also be expressed as

$$\frac{T_+}{T_-} = \frac{\gamma_-}{\gamma_+}, \tag{3.23}$$

using the definition of enthalpy, $w = \frac{s}{T}$, along with the first matching condition (3.13). As before, the subscripts $+$ and $-$ indicate quantities evaluated in front of and behind the bubble wall, respectively. This additional constraint eliminates the wall velocity as a free parameter in the hydrodynamic solutions discussed in the previous section. Instead, it allows for its determination based on basic thermodynamic quantities of the model: the enthalpy ratio between phases, defined as

$$\Psi = \frac{w_b}{w_s}, \tag{3.24}$$

the transition strength $\alpha_{\bar{\theta}}$, and the speed of sound in both phases, c_s and c_b [34]. The left panel of Fig. 3.4 presents estimates of the wall velocity in local thermal equilibrium based on this approach. Since additional friction can only slow down the wall, the resulting velocity can be interpreted as the upper bound for a fully out-of-equilibrium computation. Note that non-zero velocity requires a positive driving force. This fact, together with the definition (3.19), leads to the conclusion that the transition strength α_θ cannot be arbitrary small. The lower bound for its value is given by

$$\alpha_\theta^{\rm min} = \frac{1 - \Psi}{3}. \tag{3.25}$$

The region that does not satisfy this condition is labelled as *no nucleation*, as the symmetric minimum remains the global one there. In contrast, the other white region represents a scenario where no stationary solution can be found. It corresponds to the case when driving force always dominates over the hydrodynamic backreaction, causing the bubble wall to continue accelerating and reaching ultrarelativistic velocities. This behaviour, often referred to as *runaways*, is typical for thermal equilibrium. However, in realistic scenarios, it is expected that out-of-equilibrium corrections can eventually stop the acceleration for $v_w \approx 1$ [107–110].

To apply these results to a realistic theory and match a particular particle physics model with the hydrodynamic description of the plasma, we use the fact that the effective potential $V_{\text{eff}}(\phi, T)$ can be interpreted as the free energy density $\mathcal{F}$ of the system. Thus, similarly as in [38–40, 53, 60, 111, 112], we can define the equation of state for a system:

$$p(\phi, T) = -V_{\text{eff}}(\phi, T), \tag{3.26}$$

$$e(\phi, T) = V_{\text{eff}}(\phi, T) - T\frac{\mathrm{d}V_{\text{eff}}(\phi, T)}{\mathrm{d}T}, \tag{3.27}$$

$$w(\phi, T) = e(\phi, T) + p(\phi, T) = -T\frac{\mathrm{d}V_{\text{eff}}(\phi, T)}{\mathrm{d}T}. \tag{3.28}$$

Relating thermal potential to the pressure allows for an estimation of the hydrodynamic backreaction, as given in eq. (3.5). A simple approximation, derived in [113], yields

$$\mathcal{P}_{\text{LTE}} \approx \int_{-\epsilon}^{+\epsilon} \mathrm{d}z \frac{\partial V_{\text{eff}}}{\partial T}\frac{\partial T}{\partial z} \approx w_+ \gamma_+^2 v_+ (v_+ - v_-). \tag{3.29}$$

This relation is illustrated in the right panel of Fig. 3.4, where the hydrodynamic backreaction is shown as a function of the wall velocity. The stationary velocity corresponds to the point where it equals the driving force. However, as the backreaction is not a monotonic function of velocity, the solution, if exists, is not unique. It should be emphasized that every deflagration/hybrid solution always comes with a corresponding detonation, though these detonations are unstable. This instability arises from the fact that the net pressure in the detonation regime is a decreasing function of the wall velocity. When the bubble expands with $v_w > c_J$, any increase in velocity results in a reduction of the hydrodynamic backreaction, which can no longer balance the driving force, leading to further acceleration of the wall. The peak, located at the Jouguet

velocity c_J, corresponds to the strongest heating of the fluid shell in the hybrid regime. If the wall velocity exceeds the Jouguet value, the shock wave disappears and the total pressure begins to decrease. To summarize, the LTE approximation predicts only stable deflagrations and hybrids or ultrarelativistic runaways.

To prepare a sample for further studies, we performed a scan of the parameter space for the xSM model, as described in Chapter 2. Next, using the LTE approximation discussed above, we determined the bubble-wall velocities, identifying a range of deflagration and hybrid solutions, as well as runaway scenarios for the strongest transitions in the investigated sample. The results are shown in Fig. 2.3, where the shades of blue indicate the wall velocity, and the red points represent the runaway solutions. The validation of these results using dynamical simulations was the subject of our work described in [2] and will be presented in Chapter 4.

3.4 Bubble-wall velocity beyond local thermal equilibrium

The local thermal equilibrium approximation, while useful for a rough estimation of the wall velocity, is incomplete. In principle, a full description requires accounting for non-equilibrium friction arising from particles interacting with the bubble wall and deviating from their thermal distributions. The backreaction from these effects has traditionally been estimated by solving the Boltzmann equation for all species in the plasma alongside the equation of motion for the scalar field [4, 5, 29, 32, 33, 93–99]. However, this method is computationally demanding, so the non-equilibrium contribution to the friction in the equation of motion is instead often parametrized by an effective phenomenological coefficient, treated as a free parameter in hydrodynamical simulations [1, 39, 60].

The impact of this non-equilibrium friction can be linked with the entropy production in the system [31, 114]. Building on this idea, we extended the matching method described in the previous section to go beyond the LTE approximation [3]. An additional relation between the thermodynamic quantities on both sides of the wall can be derived by imposing the entropy production rate. We assume that the only process in which the entropy is produced during FOPT is a dissipative, friction-like interaction of thermal plasma with the moving wall. We focus on the regime where this interaction

is local and depends on the microscopic structure of the model, the plasma velocity, the field profile and temperature across the wall. This dependence can be expressed through some function f_s, leading to

$$\partial_\mu(u^\mu s) = f_s\,(v, \phi, T). \tag{3.30}$$

By integrating (3.30) over the bubble wall *in the wall frame*, one obtains

$$\frac{\partial}{\partial t}\Big(\int_M \mathrm{d}V\, s\,\gamma\Big) - \int_M \mathrm{d}V\Big(\nabla\cdot(s\gamma\vec{v})\Big) = \int_M \mathrm{d}V\, f_s(v,\phi,T), \tag{3.31}$$

where M is a thin shell with $\partial_r\phi \neq 0$. In the steady-state regime, the total entropy in the bubble wall remains constant, meaning that the time derivative of the total entropy vanishes.

Applying Gauss's theorem, we convert the volume integral of the entropy current divergence into a flux integral over the boundaries of the region. In the planar wall limit, this condition simplifies to

$$s_-\gamma_- v_- - s_+\gamma_+ v_+ = \int_{-l/2}^{l/2} \mathrm{d}z\, f_s(v,\phi,T), \tag{3.32}$$

where l is the width of the shell M, measured as a distance from the centre of the wall. This expression reduces to the familiar local thermal equilibrium condition, as discussed in the previous section, when setting $f_s = 0$.

The inhomogeneity introduced by the integral over the field profile can be interpreted as the entropy production rate at the bubble front and will be denoted by

$$\Delta S = \int_{-l/2}^{l/2} \mathrm{d}z\, f_s(v,\phi,T). \tag{3.33}$$

Using the definition of enthalpy $w = \frac{s}{T}$ and the matching condition (3.13), we obtain

$$\frac{T_+}{T_-} = \frac{\gamma_-}{\gamma_+}\left(1 + \frac{T_+\Delta S}{w_+\gamma_+ v_+}\right) \tag{3.34}$$

which represents the generalized form of our third matching condition.

The evaluation of ΔS requires knowledge of the entropy source f_s, which is determined by the microscopic structure of the plasma in a given model. This calculation involves solving the associated system of Boltzmann equations which is typically solved numerically [36]. Analytical approximations have been derived for the SM [94] and the

Minimal Supersymmetric Standard Model [101] under the assumption of a small departure from LTE, which is valid for weak FOPTs. Here, we adopt a simplified approach based on a phenomenological ansatz [38, 39, 114] which is also widely used in lattice studies of this system [40, 53, 60, 111, 112]

$$f_s(v, \phi, T) = \frac{\eta}{T}(u^\mu \partial_\mu \phi)^2. \tag{3.35}$$

The effective coupling η, treated here as a free parameter, encodes the microscopic model structure and provides a good approximation of the non-equilibrium friction.

Since the scalar field derivative $\partial_\mu \phi$ is nonzero only around the bubble front, we estimate ΔS by evaluating $1/T$ and $u^\mu u^\nu$ at their values just ahead of the wall, yielding

$$\Delta S \approx \frac{\eta}{T_+} u_+^\mu u_+^\nu \int_{-l/2}^{l/2} \mathrm{d}z \, \partial_\mu \phi \partial_\nu \phi. \tag{3.36}$$

Strictly speaking, there is no fundamental reason to evaluate ΔS using only the plasma quantities in front of the bubble. Nevertheless, for the relatively weak transitions considered here, the differences between the values just ahead of and just behind the wall are small, so more refined treatments do not lead to appreciable numerical changes.

To obtain analytically tractable expressions, we assume that the scalar field profile follows the commonly used ansatz:

$$\phi(z, t) = \frac{\upsilon_0}{2} \left[1 - \tanh\left(\frac{z}{L_w} \right) \right], \tag{3.37}$$

which provides a good approximation in most physical cases. Here υ_0 represents the vacuum expectation value (VEV) of the scalar field at the broken phase, while L_w characterizes the width of the bubble wall. Given this field profile, along with and the four-velocity of the perfect fluid from (3.7), we substitute into the entropy production integral (3.36) to obtain

$$\frac{\eta (v_+ \gamma_+)^2}{T_+} \int_{-\infty}^{\infty} \mathrm{d}z (\partial_z \phi)^2 = \frac{\eta}{3} \frac{\upsilon_0^2}{L_w} \frac{\gamma_+^2 v_+^2}{T_+}. \tag{3.38}$$

Here, we extended the integration limits setting $l \to \infty$, since the derivative of the field profile $\partial_z \phi$ rapidly vanishes away from the bubble wall. This allows us to approximate the integral over the entire real domain without introducing significant error.

Substituting (3.38) into (3.34), we obtain the modified form of the third matching condition:

$$\frac{T_+}{T_-} = \frac{\gamma_-}{\gamma_+}\,(1 + \tilde{\eta}\,\gamma_+\,v_+) \tag{3.39}$$

where we introduced the rescaled friction parameter, defined as

$$\tilde{\eta} \equiv \chi\,\eta, \qquad \chi \equiv \frac{v_0^2}{3w_+L_w}. \tag{3.40}$$

As long as the transition remains relatively weak ($\alpha_\theta \lesssim 0.1$), the enthalpy w_+ can be well approximated by its value in the symmetric phase w_s, making the scaling factor χ largely independent of friction. Notably, in the limit $\eta \to 0$, the friction term vanishes, and we recover the standard matching condition valid in the LTE regime [31, 34].

To find the bubble-wall velocity as a function of the friction parameter $\tilde{\eta}$, we solve the system of equations in (3.12) by employing the modified third matching condition (3.39), along with the two standard ones (3.13) and (3.14). The problem is tackled using the modified version of the `Python` code presented in [34], which is publicly accessible at [115].

The left panel of Fig. 3.5 shows the limiting case with $\tilde{\eta} \to 0$ corresponding to the LTE approximation. Different types of stationary solutions are shown on the (α_θ, Ψ) plane. In most of the parameter space, we find stable detonation solutions which for $\tilde{\eta} = 0$ become runaways. Reference [31] also finds detonation solutions for some benchmarks in LTE, but correctly classifies them as unphysical. Here, we found a different branch of stable detonation solutions, which do not exist in LTE. For all solutions on this new branch we find $v_w \to 1$ in the limit $\eta \to 0$. Dynamic lattice simulations discussed in the next Chapter indicate that for realistic initial conditions, the run-away branch is preferred even if there exist other stationary solutions. Thus, the LTE deflagration/hybrid solutions found in [31] are only realised in the blue region where no run-away solutions exist.

The map of the stationary states in $(\alpha_\theta, \tilde{\eta})$ plane for a benchmark value of $\Psi = 0.95$ is shown in the right panel of Fig. 3.5. The solid black line corresponds to the Jouguet velocity c_J, which represents the fastest hybrid solution, while the dashed black line marks the slowest detonations. The lower edge of the plot represents the LTE limit ($\tilde{\eta} \to 0$), where for relatively strong transitions, we observe only ultrarelativistic detonations with $v_w \to 1$, while for moderate and weak transition strengths, deflagrations and hybrid

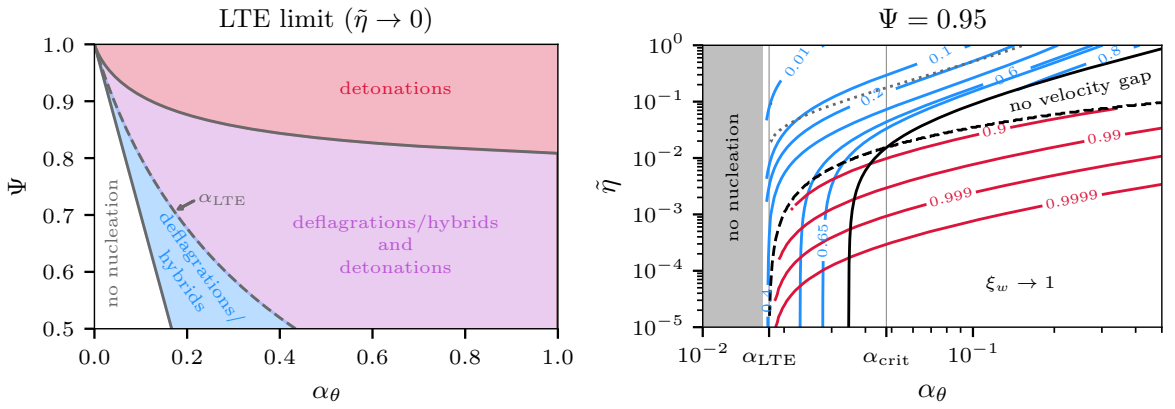

Figure 3.5: *Bubble-wall velocity evaluated using the beyond LTE third matching condition* (3.39).

Left panel: *LTE limit of the hydrodynamic solution. The blue region corresponds to the case when only deflagration/hybrid branch exists for* $\tilde{\eta} \to 0$. *The purple region denotes the situation where both deflagration/hybrid and detonation branches coexist, however, the detonation solution is typically realized in lattice simulations. The red region corresponds to the situation with no deflagration/hybrid solution (runaway scenario).*

Right panel: *contour plot of the bubble-wall velocity in* $(\alpha_\theta, \tilde{\eta})$ *plane for fixed* $\Psi = 0.95$. *The red contours represent detonation solutions with different values of the velocity, while deflagration/hybrid profiles are coloured in blue. Solid black line marks the contour of Joguet deflagration, below which there is no stable deflagration or hybrid, while black dashed line limits the region where detonation solutions exist. For transitions with* $\alpha < \alpha_{LTE}$, *only deflagration/hybrid solutions exist in the limit of* $\tilde{\eta} \to 0$. *In the grey shaded region nucleation is forbidden. Gray, dotted line illustrates the upper bound on* $\tilde{\eta}$, *coming from the ballistic limit, given with eq.* (3.47).

solutions also exist. As the friction parameter increases, the wall velocity decreases and for detonation solutions, it approaches the lower velocity limit, denoted with the black dashed line. When friction increases further, only deflagrations and hybrid solutions remain, and the wall velocity continues to decrease.

For latent heat values below the threshold $\alpha_{\rm crit}$, the velocity of the slowest detonation lies above c_J, while deflagrations and hybrids crossing the dashed line, have velocities slower than c_J. This results in a gap in the allowed velocities, as discussed in [1]. For stronger transitions with $\alpha_\theta > \alpha_{\rm crit}$, all velocities are kinematically allowed and can

potentially be realized.

If the transition is sufficiently weak ($\alpha_\theta < \alpha_{\rm LTE}$), only deflagration/hybrid solutions exist for any value of $\tilde{\eta}$. In this region, for $\tilde{\eta} \to 0$ the wall acceleration can be halted purely by hydrodynamic obstruction [105], resulting in the realization of the LTE estimate for the bubble-wall velocity [34]. The value of $\alpha_{\rm LTE}$ is determined numerically and corresponds to the asymptotic behaviour of the black dashed curve as $\tilde{\eta} \to 0$. This value is represented by the dashed line between the blue and purple regions on the left panel in Fig. 3.5.

The comparison of the resulting velocities with numerical simulations offers a possibility to know which solution of two is realised. As we will see in Chapter 4, if the two stable stationary states coexist, it is always the faster one that is favourable. Therefore, the existence of the detonation branch offers a simple criterion for determining whether the bubble wall will settle into the deflagration/hybrid steady state or continue to accelerate. Specifically, for benchmarks where a detonation solution does not exist, regardless of the value of $\tilde{\eta}$, the wall velocity cannot reach ultrarelativistic speeds. In such scenarios, the only possible solution is deflagration or hybrid. This provides a straightforward condition for evaluating the validity of LTE predictions concerning bubble-wall velocities. Notably, this condition is derived in the limit $\tilde{\eta} \to 0$, meaning it is independent of the specific form of the entropy source given by (3.35). This is crucial because such an entropy source might not be well-suited for describing ultrarelativistic bubble expansion, as discussed in [54, 116].

3.5 Bubble-wall velocity in the ballistic regime

The assumption of local thermal equilibrium holds when the mean free path of plasma particles is much shorter than the bubble wall thickness, ensuring instantaneous thermalization. If this condition is not met and particle interactions are negligible, the system can instead be described using a ballistic approach. This framework allows us to quantify the impact of nonequilibrium effects and develop more effective methods for incorporating such deviations in hydrodynamical simulations.

In [7], we distinguished between a fully ballistic fluid with free-streaming particles [117, 118] and an intermediate case, where LTE is preserved far from the wall but not

within it. This corresponds to a situation where the mean free path is larger than the wall thickness but shorter than the thickness of the surrounding fluid shell.

Scenarios involving ballistic dynamics at the bubble front can be studied using the thin wall approximation, where the wall thickness is much smaller than the bubble size. In this approximation, the energy of the bubble is given by [117]:

$$E_\phi = 4\pi\sigma \frac{R^2}{\sqrt{1-\dot{R}^2}} - \frac{4\pi}{3} R^3 \Delta V, \tag{3.41}$$

where R is the bubble radius and σ denotes the surface tension. From the conservation of energy during the expansion, the EoM reads

$$\ddot{R} + 2\frac{1-\dot{R}^2}{R} = \frac{(1-\dot{R}^2)^{3/2}}{\sigma}(\Delta V_0 - \Delta P), \tag{3.42}$$

where the interaction of the wall with the surrounding particles is captured by the pressure difference ΔP. Omitting particle self-interactions inside the wall and the soft-particle emission, the pressure difference is defined as [117]

$$\Delta P = \int \frac{\mathrm{d}^3 p}{(2\pi)^3} \sum_{i\in\pm 1} f_i(p) \frac{(n\cdot p)^2}{E_i} \mathcal{F}_i(-n\cdot p), \tag{3.43}$$

where $i = \pm 1$ refers to the regions just behind and just after the wall, respectively, and $f_i(p)$ denotes the particles distribution functions. The function $\mathcal{F}$ is given by:

$$\mathcal{F}_i(-n\cdot p) = \theta(-in\cdot p)\left[\mathcal{T}_i(n\cdot p)\left(1-\sqrt{1-i\frac{\Delta m^2}{(n\cdot p)^2}}\right) + 2\mathcal{R}_i(n\cdot p)\right], \tag{3.44}$$

where $\Delta m^2 = m_-^2 - m_+^2$ is the difference in particle mass when it enters the bubble, while $\mathcal{R}$ and $\mathcal{T} = 1-\mathcal{R}$ are the reflection and transmission coefficients, respectively. From eq. (3.42) we see, that the terminal wall velocity is attained when

$$\Delta P = \Delta V_0, \tag{3.45}$$

which represents ballistic analogue of the matching condition. In a scenario where LTE is maintained far from the wall, but breaks down within it, the fluid profiles in the steady state can be determined solving eq. (3.10). This solution provides the distribution functions $f_i(p)$ for the particles colliding with the wall, enabling the evaluation of the pressure difference (3.43). To determine the terminal wall velocity, we employ an

iterative procedure that successively refines the solution by cycling through eqs. (3.10), (3.43), and (3.45).

A similar approach was independently proposed in [102], where in addition, the authors applied the large mass limit and the bag EoS to derive the upper bound on entropy production in the ballistic regime. Using our notation, this bound is given by

$$\frac{\Delta S}{s_+ \gamma_+ v_+} \leq \left(\frac{\gamma_+^2 v_-}{\gamma_-^2 v_+} \Psi \right)^{1/4} - 1. \tag{3.46}$$

For the entropy production given by eq. (3.38), this translates into a constraint on the friction parameter:

$$\tilde{\eta}_{\max} = \frac{1}{\gamma_+ v_+} \left[\left(\frac{\gamma_+^2 v_-}{\gamma_-^2 v_+} \Psi \right)^{1/4} - 1 \right]. \tag{3.47}$$

This expression sets an upper limit on $\tilde{\eta}$, which is illustrated with a gray, dotted line in the right panel of Fig. 3.5, for a fixed value of $\Psi = 0.95$.

In fact, the entropy production ansatz given in eq. (3.35) is simplified, which inherently limits its range of validity. It relies on a local description of friction, appropriate only in the regime of strong interactions and small departures from equilibrium distribution functions of plasma constituents. As such, it does not capture the full non-local behavior expected from solutions of the Boltzmann equation, particularly near the ballistic regime. For this reason, the resulting bound should be interpreted with caution, and we advise applying it conservatively with $\tilde{\eta} \ll \tilde{\eta}_{\max}$.

CHAPTER 4

Real-time simulations of the bubble growth

So far we have employed the hydrodynamic approximation to explore possible stationary states of expanding bubbles. In this chapter, we extend this framework to investigate the real-time dynamics of the system. Instead of focusing solely on equilibrium solutions, we now study the time evolution of a single, spherically symmetric bubble using a dedicated numerical implementation. This approach incorporates both the full hydrodynamics of the system and a phenomenological model for the microscopic entropy production mechanism at the bubble front.

Our simulations track the coupled evolution of the scalar field profile and the surrounding plasma, which consists of light particles modelled as a relativistic perfect fluid. The interaction between these two components is governed by a temperature-dependent effective potential and an effective coupling term that accounts for non-equilibrium dissipative effects in the equation of motion. This formalism provides a more comprehensive description of bubble propagation, capturing the energy transfer between the field and the plasma as well as the impact of different friction mechanisms on bubble growth.

The numerical framework we adopt is well established in the literature, having been developed primarily by the Helsinki-Sussex group [38, 39, 100], and remains a widely used approach for predicting the gravitational wave spectrum [40, 60, 111, 119]. Building upon this foundation, we have developed an independent implementation tailored

to our specific objectives, with particular emphasis on ensuring the stability of hydrodynamic solutions and accurately resolving shock structures that emerge during the late-time expansion.

In this chapter, we begin by deriving the equations of motion governing the system, followed by a discussion of their discretization and the numerical methods used to solve them on a lattice. We then present simulation results for a set of toy-model benchmarks, illustrating how bubble fronts evolve toward a stationary state. These results are compared with thermodynamic profiles obtained within the bag-model approximation, highlighting both the similarities and the limitations of this simplified approach. This comparison sets the stage for our extension to realistic particle physics models. In particular, we emphasize the presence of a velocity gap in the $v(\eta)$ relation and provide a qualitative explanation for its origin [1].

Next, we adjust the framework to the real scalar extension of the Standard Model and perform simulations in local thermal equilibrium to assess the validity of the approximation derived in [34]. We find that not all the stationary solutions are dynamically realized. Instead, runaways are frequently observed, as the early-stage dynamics following nucleation enable bubble walls to reach highly supersonic velocities before a heated fluid shell forms in front of the expanding bubble. This effect is not captured by other methods that assume the existence of stationary solutions at all times [2].

Finally, we refine the simulations for the xSM model by incorporating a phenomenological friction term, thereby extending our analysis beyond local thermal equilibrium. We compare the stationary-state predictions obtained from the generalized third matching condition with our numerical results, ultimately establishing a comprehensive connection between these two methodologies and verifying the selection rule to determine which stationary states are physical [3].

This chapter represents the most innovative part of the thesis, offering new insights into the real-time dynamics of phase transitions and, for the first time, establishing a direct connection between the analytical methods discussed in Chapter 3 and the results of numerical simulations. By bridging these two approaches, we provide a new framework for studying bubble expansion, with implications for gravitational wave predictions and beyond.

4.1 Equations of motion for the system

To describe the dynamics of the phase transition, we consider a system consisting of a scalar field ϕ interacting with a thermal plasma. The evolution of such a system is governed by the conservation of the total energy-momentum tensor, which includes contributions from both the field and the fluid. It takes the form

$$T^{\mu\nu} = T^{\mu\nu}_{\text{field}} + T^{\mu\nu}_{\text{fluid}}. \tag{4.1}$$

The individual components are given by

$$T^{\mu\nu}_{\text{field}} = \partial^\mu\phi\partial^\nu\phi - g^{\mu\nu}\left(\frac{1}{2}\partial\alpha\phi\partial^\alpha\phi\right), \tag{4.2}$$

$$T^{\mu\nu}_{\text{fluid}} = wu^\mu u^\nu + g^{\mu\nu}p, \tag{4.3}$$

where u^μ is the four-velocity of the fluid, and p denotes its pressure. Note that in our convention the vacuum energy is incorporated into the fluid energy-momentum tensor via the equation of state (3.26)-(3.28), so it does not explicitly appear in the above expressions. To recover eq. (3.3), we will later introduce the derivatives of the effective potential as a source term for hydrodynamic backreaction.

Since we focus on the dynamics of a single, spherically symmetric bubble, it is convenient to work in spherical coordinates. In flat spacetime, the metric tensor takes the form

$$g = -dt \otimes dt + dr \otimes dr + r^2\left(d\theta \otimes d\theta + \sin^2\theta d\varphi \otimes d\varphi\right). \tag{4.4}$$

Here, we neglect the effects of cosmological expansion, as the timescale for bubble growth in moderately strong phase transitions during the radiation-dominated era is much shorter than the Hubble time.

The conservation of the energy momentum tensor can be separated into field and fluid parts, both of which are not conserved independently due to the additional energy transfer terms:

$$\nabla_\mu T^{\mu\nu}_{\text{field}} = \frac{\partial V}{\partial\phi}\partial^\nu\phi + \eta u^\mu\partial_\mu\phi\partial^\nu\phi, \tag{4.5}$$

$$\nabla_\mu T^{\mu\nu}_{\text{fluid}} = -\frac{\partial V}{\partial\phi}\partial^\nu\phi - \eta u^\mu\partial_\mu\phi\partial^\nu\phi. \tag{4.6}$$

The left-hand side of equation (4.5) contains the wave equation in spherical coordinates, which leads to the equation of motion in the following form:

$$-\partial_t^2\phi + \frac{1}{r^2}\partial_r(r^2\partial_r\phi) - \frac{\partial V}{\partial\phi} = \eta\gamma(\partial_t\phi + v\partial_r\phi). \tag{4.7}$$

This equation recovers (3.3) for the η-dependent term that parametrizes the non-equilibrium friction, expressed as:

$$-\sum_i \frac{\mathrm{d}m_i^2(\phi)}{\mathrm{d}\phi}\int\frac{\mathrm{d}^3p}{(2\pi)^3 2E_i}\delta f_i(p,x) \equiv \eta u^\mu\partial_\mu\phi, \tag{4.8}$$

which is consistent with the form of entropy current (3.35). The numerical value of η remains, in principle unknown, so we leave it as the free parameter in the simulation. The equations governing the fluid dynamics determine the evolution of thermodynamic quantities v and p that describe the plasma. With the four-velocity of the perfect fluid, and considering the time ($\nu = 0$) and spatial ($\nu = 1$) components of equation (4.6), we obtain

$$\nabla_\mu T^{\mu 0}_{\text{fluid}} = \nabla_\mu\left(wu^\mu u^0 + g^{\mu 0}p\right) = \partial_t(w\gamma^2 - p) + \frac{1}{r^2}\partial_r(r^2 w\gamma^2 v), \tag{4.9}$$

$$\nabla_\mu T^{\mu 1}_{\text{fluid}} = \nabla_\mu\left(wu^\mu u^1 + g^{\mu 1}p\right) = \partial_t(w\gamma^2 v) + \frac{1}{r^2}\partial_r\left(r^2 w\gamma^2 v^2\right) + \partial_r p. \tag{4.10}$$

To simplify the equations, we introduce two new thermodynamic variables: $Z := w\gamma^2 v$ and $\tau := w\gamma^2 - p$. Using this parametrization, the equations of motion for the fluid can be rewritten as

$$\partial_t\tau + \frac{1}{r^2}\partial_r(r^2(\tau + p)v) = \frac{\partial V}{\partial\phi}\partial_t\phi + \eta\gamma(\partial_t\phi + v\partial_r\phi)\partial_t\phi, \tag{4.11}$$

$$\partial_t Z + \frac{1}{r^2}\partial_r\left(r^2 Zv\right) + \partial_r p = -\frac{\partial V}{\partial\phi}\partial_r\phi - \eta\gamma(\partial_t\phi + v\partial_r\phi)\partial_r\phi. \tag{4.12}$$

Equations (4.11) and (4.12), together with (4.7), supplemented by the equation of state (3.26)-(3.28), form a closed system of partial differential equations, which is further discretized and solved numerically on a lattice, as described in the next section.

4.2 Numerical treatment

In order to obtain a numerical approximation for solutions of equations (4.7), (4.11) and (4.12) we use the finite element method, in both time and space.

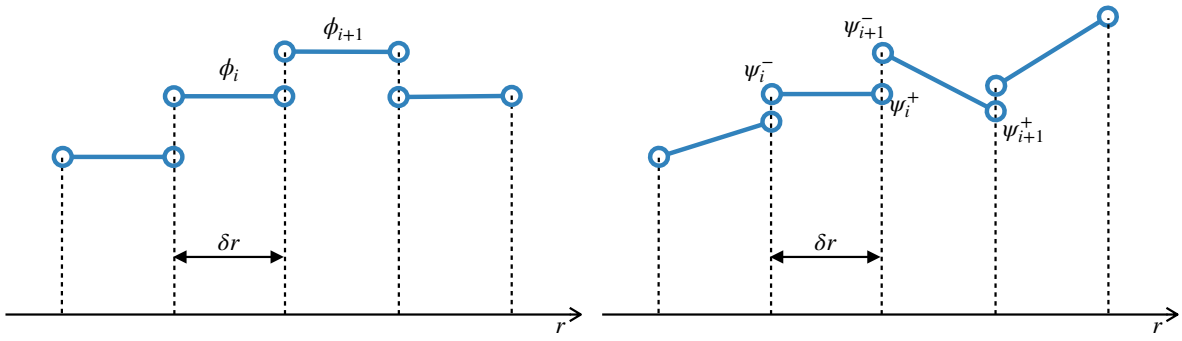

Figure 4.1: *Schematic illustration of the interpolating functions used in the spacial Galerkin method: discontinuous piecewise constant function for the interpolation of the scalar field ϕ and conserved quantities Z, τ (left panel); discontinuous piecewise linear function for the interpolation of the scalar field gradient $\psi = \partial_r \phi$ (right panel).*

To discretise in space, we employ the discontinuous Galerkin method [120–127]. The computational domain $[0, R]$ is divided into elements of length δr. The wave equation (4.7), governing the evolution of the scalar field is treated using a mixed scheme, introducing an auxiliary variable $\psi = \partial_r \phi$, which is interpolated using discontinuous piecewise linear functions (see Fig. 4.1). For numerical quadrature, we employ a trapezoid rule adapted to spherical coordinates:

$$\int_a^b x^2 f(x)\,\mathrm{d}x = \lim_{\epsilon \to 0^+} \frac{b-a}{12} \Big[f(a+\epsilon)\left(3a^2 + 2ab + b^2\right) + f(b-\epsilon)\left(a^2 + 2ab + 3b^2\right) \Big] + \mathcal{O}\left((b-a)^3\right). \tag{4.13}$$

which generalizes the second-order central finite difference scheme in Cartesian coordinates.

In the centre of the bubble ($r = 0$) we impose the Neumann boundary condition for field ϕ, which in the mixed formulation translates to $\psi|_{r=0} = 0$. At the outer edge of the computational domain ($r = R$), we enforce the Dirichlet boundary condition by setting the field value to the position of the false minimum.

For the temporal discretization, we utilize the discontinuous piecewise linear interpolation functions for ϕ and right-discontinuous linear interpolation for its time derivative $\dot{\phi}$, yielding a scheme that mimics position formulation of the Strömer-Verlet method.

Compared to the scalar field equation, deriving a numerical scheme for the plasma evolution is significantly more challenging. Equations (4.11) and (4.12) are first-order hyperbolic equations which present difficulties for numerical methods due to the formation of discontinuities within a finite time, even from smooth initial conditions. Various numerical methods have been proposed to address this issue. We decided to use flux-corrected transport, as introduced in [128–131], to maintain second-order accuracy in smooth regions of the profile while preventing numerical artifacts (such as the Gibbs effect) around discontinuities. This approach employs two schemes, referred to as high-order and low-order, which are combined in a way that ensures the solution remains within the range of physically correct values according to the maximum principle [132, 133].

To derive the high-order scheme (second-order in our case) for the FCT procedure, we employed the local discontinuous Galerkin method with piecewise constant interpolation functions for the conserved quantities Z and τ. Time integration of the high-order scheme was performed using the explicit midpoint method [120–127]. The low-order scheme was constructed via algebraic upwinding [128–131] which yields a local extrema diminishing scheme, and was integrated in time using the backward (implicit) Euler method. The forward (explicit) Euler method was tested but proved to be unstable in certain cases near the centre of the bubble $r = 0$.

For the limiting procedure, we adapted Zalesak's peak preserving limiter [134] incorporating a correction inspired by [135] to restrict the range over which conserved quantity values are considered when limiting antidiffusive fluxes.

The entire FCT algorithm can be summarized in the following steps:

1. Compute the low-order fluxes F^L using a method that ensures no unphysical values are generated.

2. Compute the high-order fluxes F^H using a method that maintains accuracy in smooth regions of the solution.

3. Compute the antidiffusive fluxes as $A = F^H - F^L$.

4. Compute the numerical solution for the conserved quantities U^L using the low-order method.

5. Limit the antidiffusive fluxes as $A_\alpha = \alpha A$, ensuring that $\alpha \sim 1$ in smooth regions and $\alpha \sim 0$ near shocks.

6. Apply the limited fluxes A_α to U^L, o obtain the final solution, which reproduces the high-order scheme in smooth regions.

Finally, since the fluxes in equations (4.11) and (4.12) are expressed in terms of both conserved and so-called primitive variables v, T (and p derived from them), it is necessary to determine the primitive variables from ϕ, τ, and Z, which are evolved in the code. To achieve this, we combine the equations of state (3.26)-(3.28) to obtain

$$\tau + p(\phi, T) - \frac{1}{2}\left(w(\phi, T) + \sqrt{w(\phi, T)^2 + 4Z^2}\right) = 0. \tag{4.14}$$

This equation is solved using the Raphson-Newton method to find the temperature T. Once T is determined, w and p can be computed directly from the equations of state, and the velocity v can be easily obtained by inverting the definition of Z.

4.3 Setup of the simulations

The numerical simulations were performed on the `KRUK` computer cluster [136]. In most cases, the grid size was set to $\delta r = 0.01$ GeV^{-1} and $\delta t = 0.001$ GeV^{-1}, although other values were tested to ensure numerical convergence. The duration of the evolution was chosen to be long enough for the system to asymptotically reach stationary states, typically set to $t_{max} \sim 100$ GeV^{-1}, depending on the specific model. The physical size of the lattice was fixed at $R = t_{max}$, which is large enough to prevent the bubbles from reaching the boundaries, as they expand subluminally.

Each simulation was initialized with field profiles corresponding to the recently nucleated bubble, computed using the `CosmoTransitions` code [85], denoted with the dashed profiles in Fig. 4.2. To smoothly extend the initial profile across the entire computational domain, we fitted a hyperbolic tangent ansatz, given by

$$\phi(t = 0) = \frac{v_e}{2}\left(1 - \tanh\frac{r - r_0}{L_w}\right), \tag{4.15}$$

to the actual critical bubble, treating v_e, r_0, and L_w as fitting parameters. The plasma velocity v and temperature T were initialized as spatially uniform, with $v(r) = 0$ and

$T(r) = T_n$, respectively. This choice approximates a homogeneous plasma in which nucleation occurs and enables accurate tracking of the early stages of bubble evolution and the formation of the fluid profiles. The conserved variables Z and τ were initialized to the values corresponding to the initial profiles of v and T.

4.4 Benchmark evolution

To evaluate the performance of our code, we initialized simulations with two benchmark points that have been previously studied in a similar context [60], using a toy-model potential with high-temperature corrections, parametrized as

$$V(\phi, T) = -\frac{\pi^2}{90} g_* T^4 + \frac{1}{2}\gamma(T^2 - T_0^2)\phi^2 - \frac{1}{3}\delta T \phi^3 + \frac{1}{4}\lambda\phi^4, . \tag{4.16}$$

Table 4.1 summarizes the key parameters characterizing these models.

Fig. 4.2 shows the early-time evolution of the scalar field and plasma profiles for benchmark model M_2, evaluated for two different values of the effective friction coefficient corresponding to distinct hydrodynamic regimes. The left column illustrates the evolution toward a deflagration-like solution ($\eta/T_c = 0.45$), while the right column corresponds to a detonation-like regime ($\eta/T_c = 0.13$). All profiles are plotted as functions of the radial coordinate r, with color indicating time since nucleation in the range $t \in [0, 0.05\, t_{\max}]$. The gray dashed line marks the initial critical bubble configuration.

These snapshots show how the system dynamically develops structures characteristic of a self-similar regime from the natural initial configuration. As friction and hydrodynamic backreaction come into play, the scalar field profile becomes thinner and approaches the true vacuum υ_0 at the centre of the bubble, while the plasma velocity and temperature gradients evolve into well-defined, stationary shapes.

A detailed view of the stationary regime is presented in Fig. 4.3, where the profiles are shown in self-similar coordinates $\xi = r/t$. In this representation, all thermodynamic

Benchmark	T_c [GeV]	T_0 [GeV]	γ	δ	λ	T_n [GeV]	α_θ
M_1	100	$\frac{100}{\sqrt{2}}$	$\frac{1}{18}$	$\frac{\sqrt{10}}{72}$	$\frac{10}{648}$	86	0.005
M_2	100	$\frac{100}{\sqrt{2}}$	$\frac{2}{18}$	$\frac{\sqrt{10}}{72}$	$\frac{5}{648}$	80	0.05

Table 4.1: *Model parameters for the benchmark points*

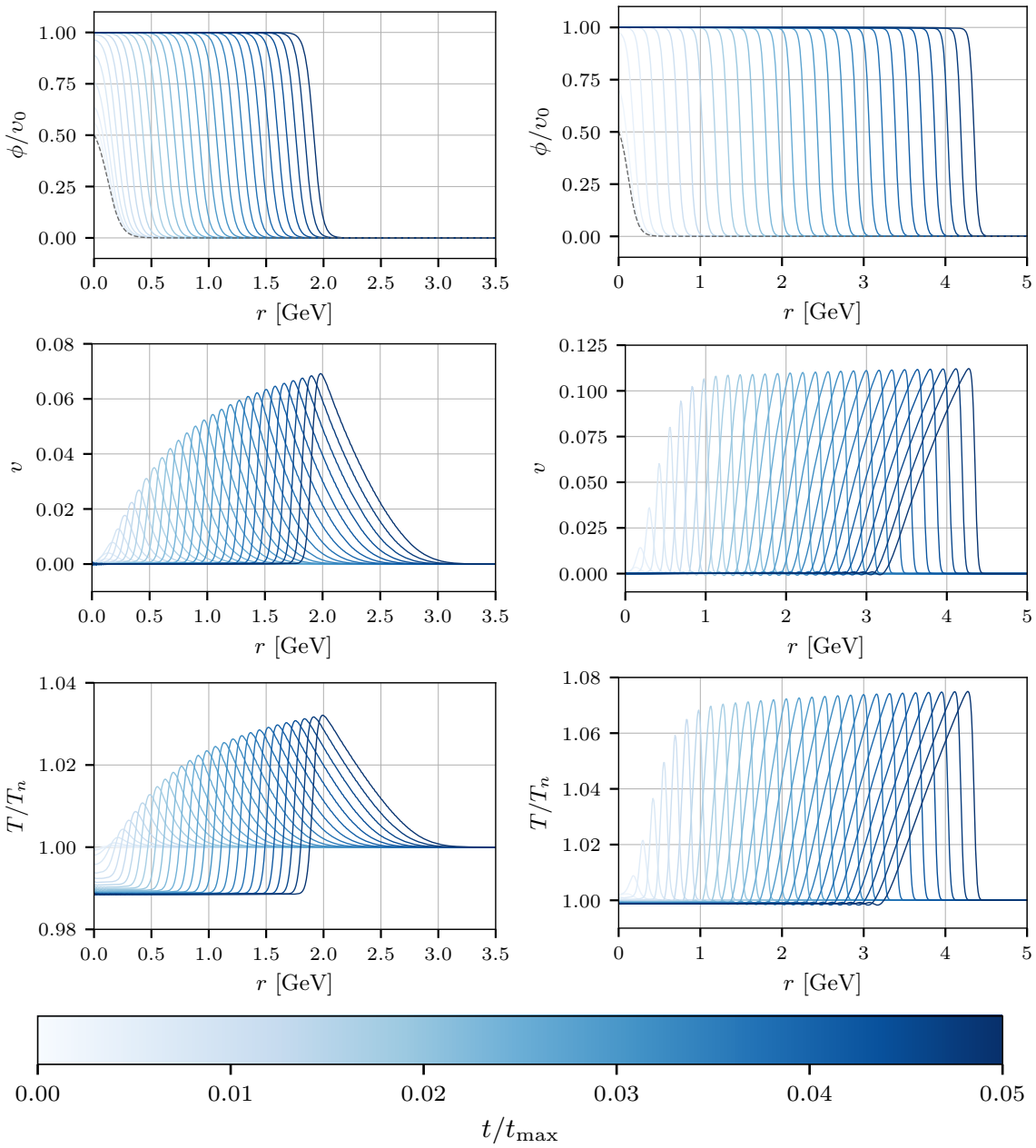

Figure 4.2: *Early stages of the real-time evolution of the system for the benchmark model M_2 with the effective friction parameter $\eta/T_c = 0.45$ (left column) and $\eta/T_c = 0.13$ (right column). Colour coding denotes the time t since nucleation.* ***Top row:*** *scalar field profile $\phi(r)/v_0$, with the critical bubble shown as a dashed line.* ***Middle row:*** *plasma velocity profile $v(r)$.* ***Bottom row:*** *plasma temperature profile $T(r)/T_n$.*

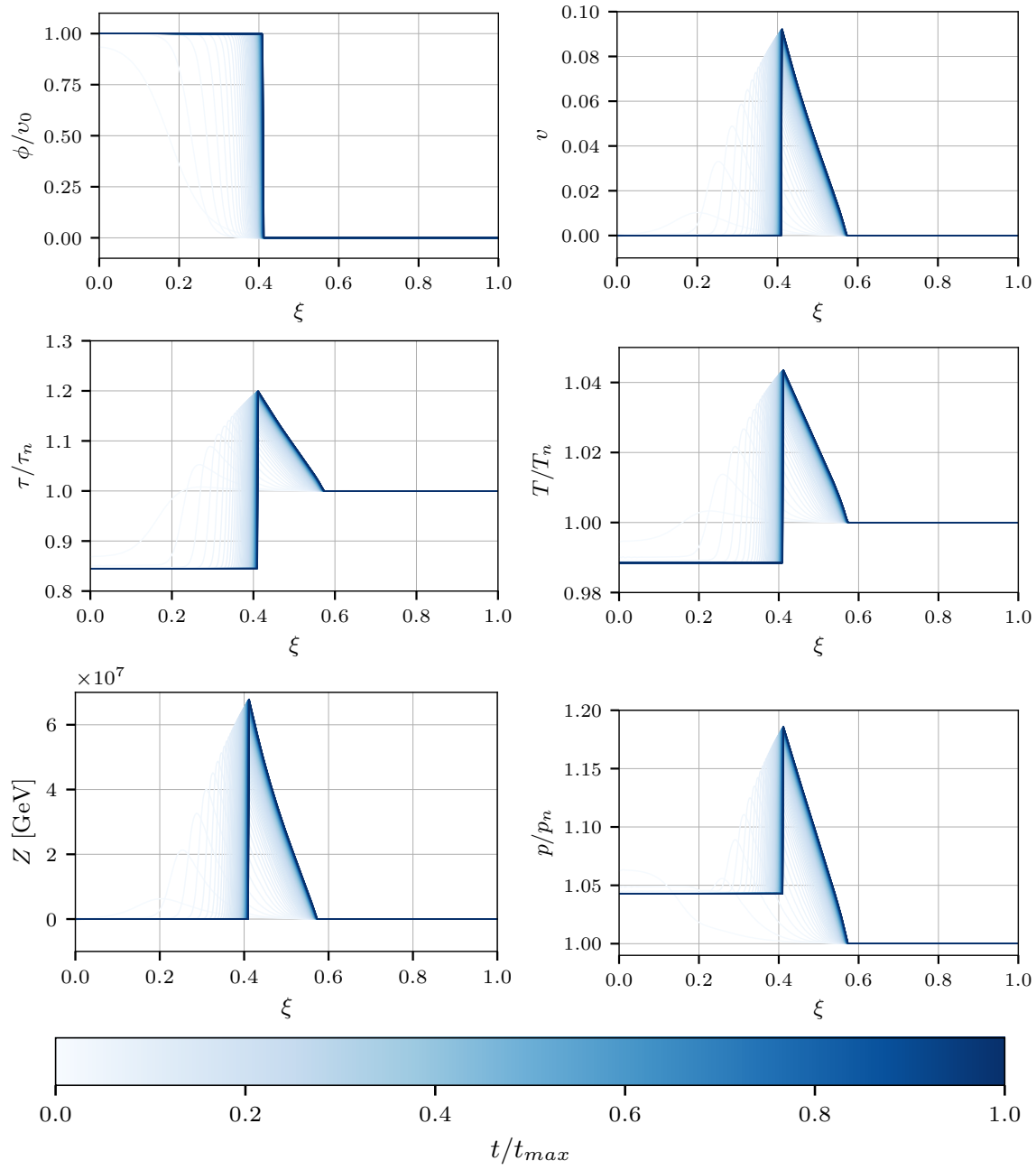

Figure 4.3: *Real-time evolution of the system toward stationary state for benchmark model M_2 with effective friction parameter $\eta/T_c = 0.45$. Colour coding denotes the time t since nucleation.* ***Left column:*** *scalar field ϕ normalized to its vacuum expectation value in the broken phase v_0 and conserved variables τ and Z describing the fluid.* ***Right column:*** *primitive variables, i.e plasma velocity v, temperature T and pressure p. Some thermodynamical quantities are normalized to their values in the nucleation temperature.*

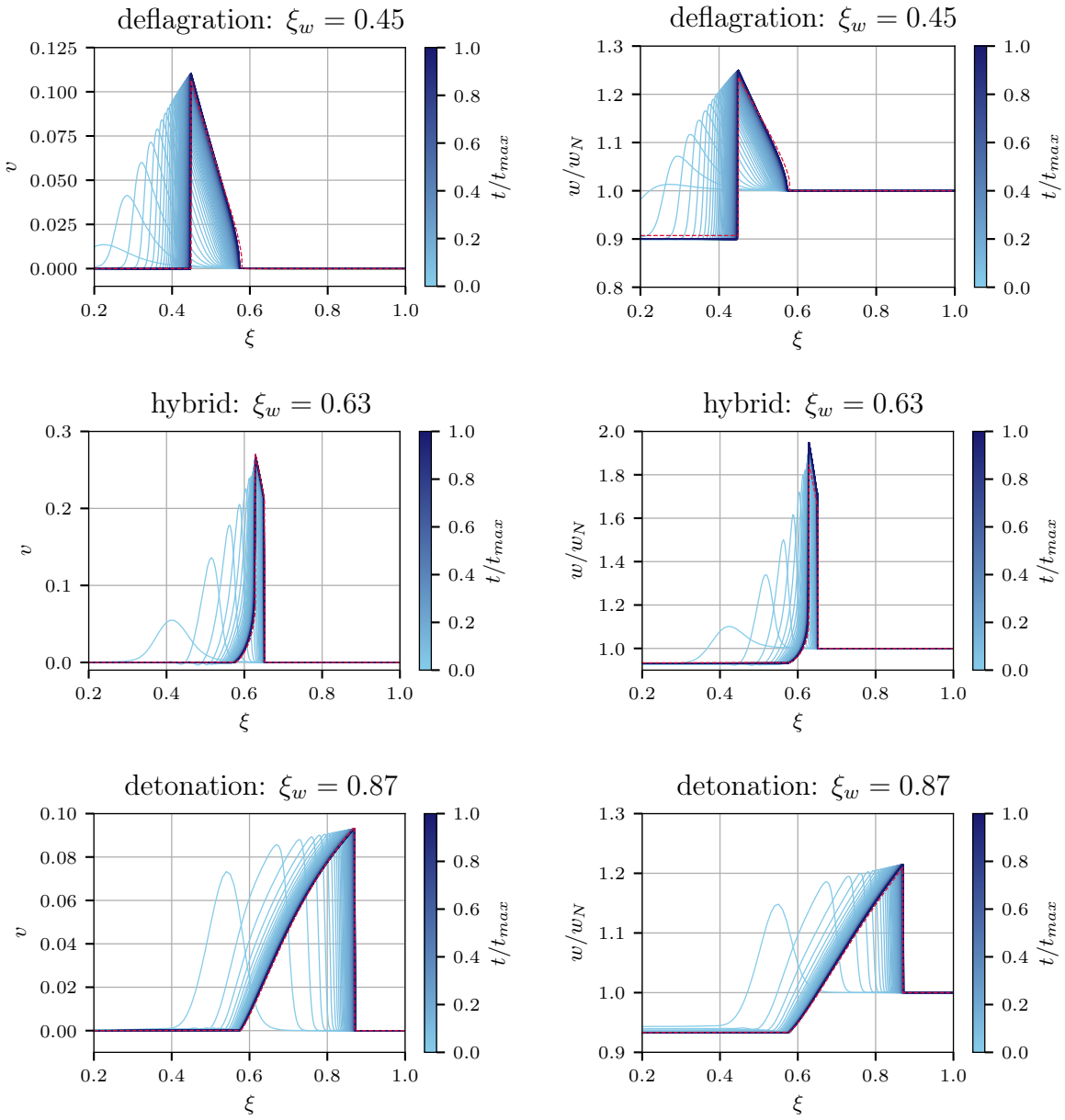

Figure 4.4: *Time evolution of the plasma shell profiles for plasma velocity v and enthalpy w as functions of the self-similar variable $\xi = r/t$. In general, all three types of solutions were found: deflagrations (first row), hybrids (second row), and detonations (third row). Different shades of blue correspond to the time flow. Profiles evolve towards stationary states represented by darker colours. Red, dashed lines denote analytical profiles obtained within the bag model.*

quantities clearly approach stable, self-similar configurations. For simplicity, we show only the results for the deflagration here; however, stationary detonations and hybrid solutions are obtained in a similar manner, with examples provided later in this chapter.

The shapes of stationary profiles show excellent agreement with the predictions of the bag model. A comparison between of our simulation results and the analytical profiles for three representative cases is presented in Fig. 4.4. As shown, we successfully resolved the shocks and accurately reproduced the form of hybrid solutions, which has typically been a challenge in previous studies involving dynamical codes.

The results of the scan over the friction parameter η, presented in Fig. 4.5, confirm the general trend that as η grows, the wall velocity monotonically decreases. However, not all the velocities are typically realized. For the stronger transition (M_2), we obtained all three types of solutions, whereas for the weaker one (M_1), no hybrids were found. This confirms the presence of a velocity gap in the region where hybrid profiles are expected. Such a gap appears in both cases: for M_1, it spans the entire range $\xi_w \in [c_b, c_J]$, while for M_2, it allows the deflagration branch to extend to solutions with supersonic wall velocities. The details of this phenomenon had not been well understood previously and were the main focus of our work in [1].

4.5 Velocity gap

As shown in the previous section, the exact relation between the friction parameter η and the terminal wall velocity ξ_w, generally, depends on the parameters of the potential. To investigate its dependence on the vacuum expectation value of the scalar field, we considered different realizations of phase transitions while keeping both the transition strength α_θ and the nucleation temperature ratio T_n/T_c fixed. Fig. 4.6 demonstrates that since $\eta \sim \phi^{-1}$, the field value in the true vacuum, v_0, fully determines the position of the velocity gap in terms of the friction parameter η. We therefore conclude that the shape of the $\xi_w(\eta)$ relation can be fully described in terms of α_θ and T_n/T_c alone. Moreover, this dependence appears to be universal across a broad class of models with polynomial potentials, as it does not explicitly rely on any model-specific couplings.

To further investigate the role of the nucleation temperature, we extended our analysis to a set of potentials where α_θ and the critical temperature T_c remain fixed, but

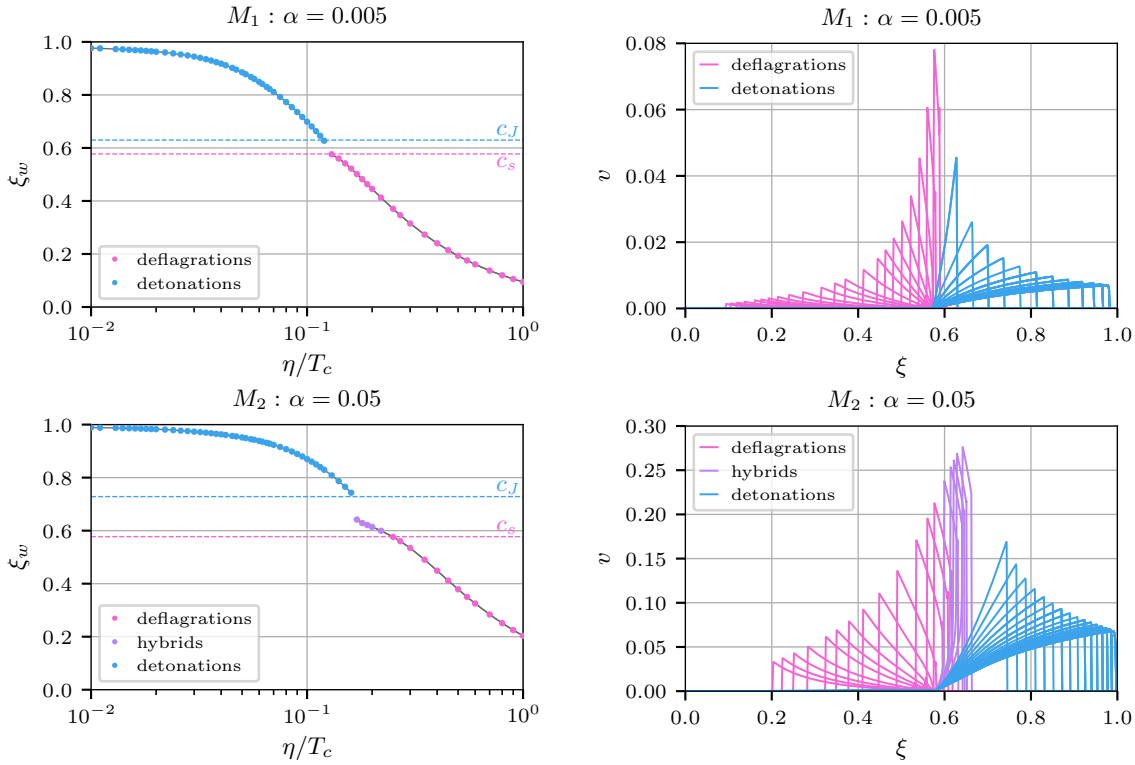

Figure 4.5: *Relation between the friction parameter η and the bubble-wall velocity in the stationary state ξ_w (left panels). Overview of the corresponding velocity profiles for each point (right panels). The first row corresponds to the weaker transition (M_1), while the second to the stronger one (M_2).*

the potential parameters are chosen to yield different nucleation temperatures T_n. This allows us to isolate the impact of T_n on the $\xi_w(\eta)$ relation. The results, presented in Fig. 4.7 (left panels), illustrate how varying T_n affects the dependence of the wall velocity on the friction parameter for two representative transition strengths, $\alpha_\theta \in 0.05, 0.1$.

The results indicate that higher nucleation temperatures lead to a wider velocity gap, whereas for lower temperatures, nearly the entire range of wall velocities can be realized. Notably, when the nucleation temperature approaches the critical temperature, the bubble-wall velocity becomes constrained for both deflagrations and hybrids, preventing it from reaching the speed of sound.

This dependence is further illustrated in the right column of Fig. 4.7, where we present the temperature at the peak of the bubble-wall profile for different nucleation

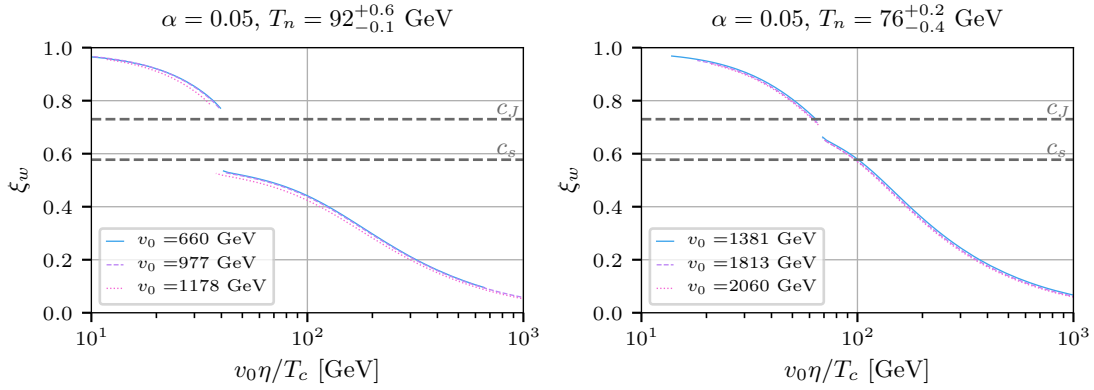

Figure 4.6: *Relation between the friction parameter η and bubble-wall velocity in the stationary state ξ_w, for the fixed nucleation temperature $T_n = 76$ GeV (left panel) and $T_n = 92$ GeV (right panel). Different colours represent different positions of the true vacuum.*

temperatures and values of α_θ. As seen, a stationary state cannot generally be achieved if the temperature profile significantly exceeds the critical temperature. This condition plays a crucial role in explaining the lower part of the velocity gap, where $\xi_w < c_s$. In fact, this type of hydrodynamical obstruction was already proposed in the small-velocity limit [105], where bounds on the subsonic wall velocity were derived.

Our results agree roughly with those limits when the nucleation temperature is very close to the critical one. However, we found that a similar behaviour continues for much lower temperatures and eventually also supersonic solutions are affected. The mechanism itself in those cases becomes less straightforward, though, as the temperature reached within the shells is significantly below the critical one when the instability sets in, and the non-equilibrium effects become important.

We conclude that some solutions are always forbidden, and the velocity gap widens as the nucleation temperature predicted by the potential approaches the critical temperature, at which the potential minima become degenerate. In [1], we provided only a qualitative description of this phenomenon and proposed a simple fit:

$$\xi_w^{max} = \left(1 - \frac{T_n}{T_c}\right)^k, \quad \text{with} \quad k = 0.2768 \pm 0.0055, \tag{4.17}$$

which serves as a rough approximation of the upper bound for the wall velocity in deflagration/hybrid solutions. This relation has a similar origin to the one proposed in [105], but it includes an additional suppression factor, characterized by the power k,

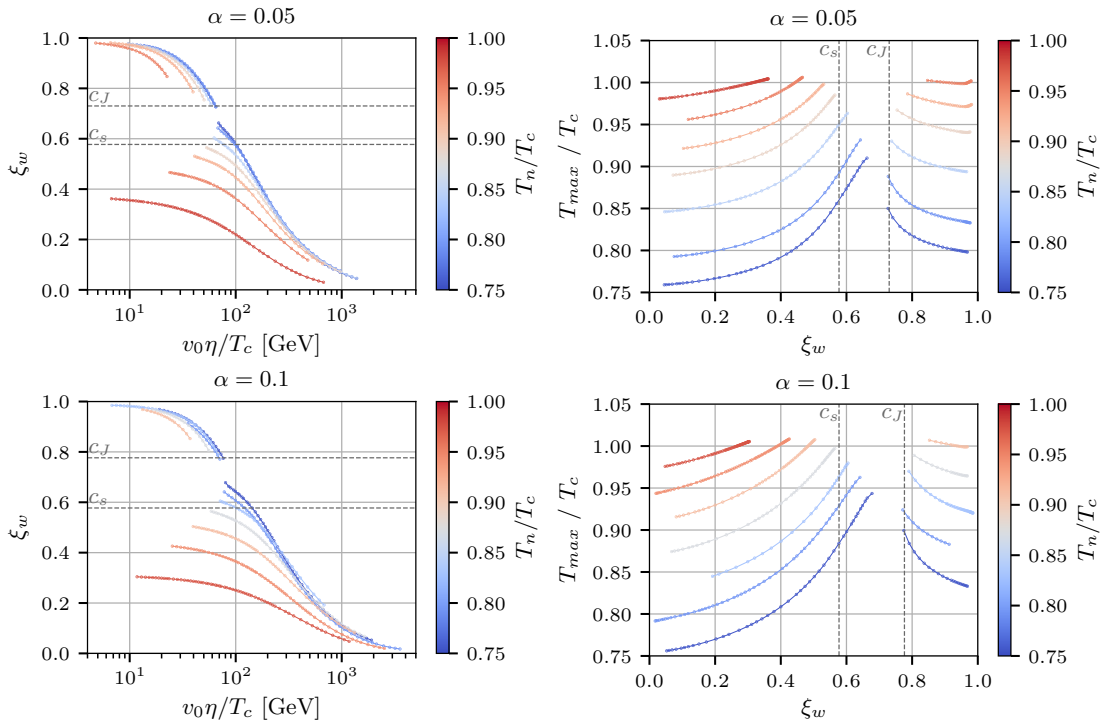

Figure 4.7: *Relation between the friction parameter η and bubble-wall velocity in the stationary state ξ_w (left panels) and the maximum of the plasma temperature along the profile (right panels). Potentials are chosen such that the strength of the transition is fixed to $\alpha_\theta = 0.05$ (upper row) and $\alpha_\theta = 0.1$ (lower row). The value of the nucleation temperature T_n is encoded with the colour.*

which accounts for the effects observed at low temperatures.

Note that in some extreme cases with $T_n \sim T_c$, detonation solutions were not observed, suggesting that in the limit $\eta \to 0$, pure hydrodynamic backreaction can lead to subsonic steady-state expansion. This result, analytically predicted in [30, 31] but not previously reported in numerical simulations, served as a starting point for bridging these two approaches. It motivated a more detailed study of real-time bubble-wall dynamics in the limit $\eta \to 0$ [2], which is the focus of the next section.

Finally, a full quantitative understanding of the origin of the velocity gap was achieved by introducing the entropy production rate and the corresponding matching condition [3], as described in Chapter 3. This approach allowed us to fully predict the size of the gap for a given model, parametrized by α_θ and Ψ. An example of the relation between the forbidden region and α_θ for $\Psi = 0.95$ is illustrated in Fig. 4.8.

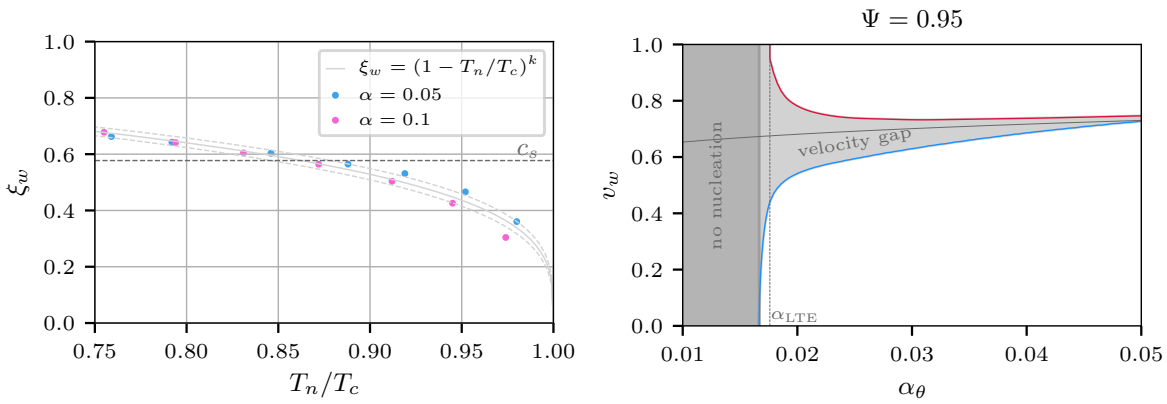

Figure 4.8: ***Left panel:*** *Maximum wall velocity on the deflagration/hybrid branch, obtained from real-time simulations, as a function of T_n/T_c, with the fit given by (4.17).* ***Right panel:*** *Analytical estimates of the velocity gap as a function of α_θ, obtained using the generalized matching method (see Chapter 3). The blue line represents the fastest deflagration/hybrid solution, while the red line corresponds to the slowest detonation. Note that for $\alpha_\theta < \alpha_{LTE}$, no detonation solution exists.*

4.6 Real-time evolution of the bubble in LTE

To further investigate the impact of hydrodynamic backreaction and verify the asymptotic behaviour of the solution in the limit of local thermal equilibrium, we employ our numerical framework to simulate the real-time evolution of bubble-wall expansion in the absence of non-equilibrium friction. As discussed in Chapter 3, this limit was recently analysed analytically [34], but numerical confirmation has so far remained elusive. Building upon the insights from the previous section, we now focus on the self-consistent dynamics of the expanding wall when frictional forces become negligible.

As a benchmark model, we consider a singlet scalar extension of the Standard Model, using the parameter sample presented in Chapter 2. Our results reveal significant deviations from the predictions of the matching method, as illustrated in Fig. 4.9. The left panel presents the velocities obtained from our simulations, while the right panel shows the corresponding predictions from the matching method. For the majority of cases where the matching approach predicts deflagration or hybrid solutions, we observe a qualitatively different evolution: the bubble walls accelerate beyond the Jouguet velocity before a heated fluid shell can form in front of the expanding bubble.

A representative example of this behaviour is depicted in the left panel of Fig. 4.10.

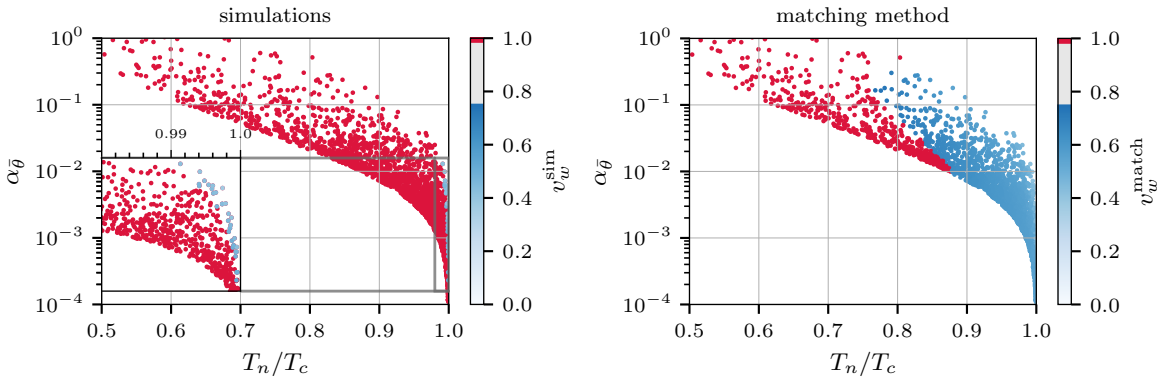

Figure 4.9: *Results for the bubble-wall velocity in LTE from the hydrodynamical simulations (left panel) and from analytical calculations [34] (right panel). The stationary states are shown in shades of blue corresponding to the wall velocity in both panels while runaway scenarios are shown in red. In most of the parameter space where matching equations predict a deflagration or hybrid solution the simulation results in a runaway. In those cases, the simulated bubble accelerates beyond the Jouguet velocity before the heated fluid shell around the bubble is formed while analytical methods assume a steady state at all times where the shell is heated enough to cease the acceleration.*

This effect can be understood as a direct consequence of the rapid bubble growth in local thermal equilibrium. During the early stages of expansion, the plasma perturbations remain small in amplitude and less sharply defined compared to their steady-state counterparts. As a result, the backreaction force exerted by the plasma on the bubble wall is significantly weaker than in the stationary regime, allowing the wall to accelerate further. If the velocity surpasses the Jouguet limit before a steady-state profile is established, no stationary solution can be realized, and the bubble continues to grow in a runaway-like manner.

This phenomenon is not limited to isolated cases but occurs for the vast majority of parameter points in our scan where the matching method predicts a finite wall velocity. In fact, the realisations that do reach a steady-state solution are confined to a finely-tuned region of parameter space, where $T_n/T_c \sim 1$. For relatively weak transitions that are not supercooled, the plasma temperature around the bubble front quickly reaches the critical temperature T_c. This prevents further acceleration of the bubble wall, as achieving higher velocities (up to the Chapman-Jouguet limit) would require a temperature peak exceeding T_c which would locally tend to reverse the ongoing

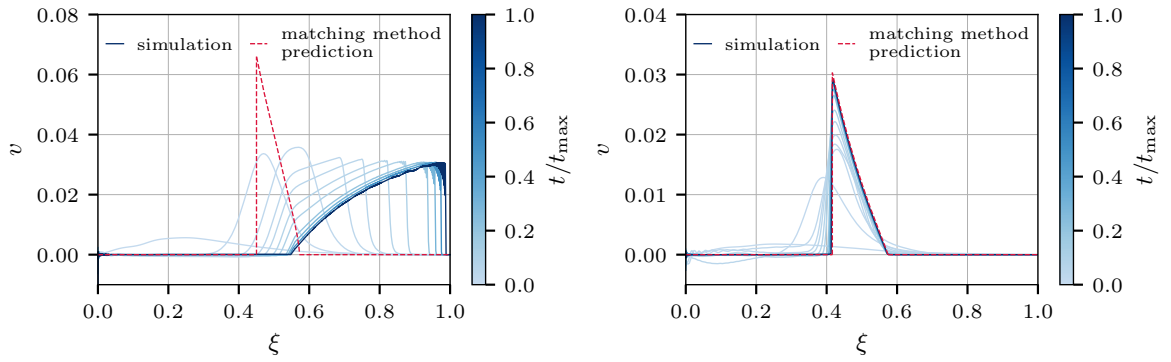

Figure 4.10: *Two possible scenarios for the growing bubble in local thermal equilibrium approximation: rapid expansion beyond Chapman-Jouguet velocity leading to a runaway scenario (left panel) and evolution toward a stationary state predicted by matching conditions (right panel). Solid blue curves represent the results of the real-time simulations, where darker shades correspond to later times. Red, dashed curves denote predictions of the equilibrium methods.*

transition. From this moment the bubble asymptotically approaches a constant velocity, and the plasma profiles evolve toward the stationary states predicted by the matching conditions.

A similar behaviour was observed in the ballistic simulations [7]. From the EoM (3.42) it follows that the wall tension parameter σ does affect the terminal velocity in the limit $R \to \infty$, provided that ΔP remains unchanged. However, when the particle-particle interactions are included, the fluid thermalizes, making ΔP time-dependent. To verify this scenario, N-body simulations were performed, varying σ, while keeping the remaining parameters fixed. The results confirmed that modifying the wall tension did not alter the terminal velocity but influenced whether a stationary solution could be achieved and how rapidly the wall velocity evolved in the early stages of expansion. For a detailed discussion of these results, see [7].

While this occurs only in a very limited region of the parameter space, it is worth noting that the bubble-wall velocities and plasma profiles obtained from our hydrodynamic simulations closely match those predicted by the matching method of [34] in cases where both approaches indicate non-runaway behaviour. A direct comparison of the predictions for this subset of parameter points is presented in Fig. 4.11, showing that the differences do not exceed a few percent.

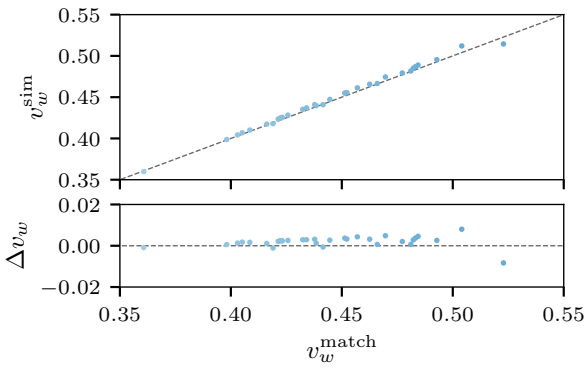

Figure 4.11: *Comparison of the bubble-wall velocity from matching method estimates* $v_w^{\rm match}$ *[34] vs those measured in hydrodynamic simulation* v_w^{sim}*. The lower panel shows the difference between these two values* $\Delta v_w = v_w^{sim} - v_w^{match}$*. The low number of points results from the fact that the two methods agree on the final steady state solution in a very small part of the parameter space where* T_n/T_c *and* $\alpha_{\bar{\theta}}$ *are tuned. The result of the simulation is much more often a runaway (see Fig. 4.9).*

To the best of our knowledge, this study represents the first attempt to directly compare analytical predictions with numerical simulations in this context. The authors of [114] employed a similar setup, solving the equations of motion for the very early stages of bubble evolution ($t_{max} \approx 0.6$ GeV^{-1}, compared with $t_{max} \simeq 100$ GeV^{-1} in our work). While their results demonstrated the initial formation of hydrodynamic profiles, the limited dynamical range prevented verification of whether steady-state solutions were eventually reached. It is also worth noting that their analysis focused on a single benchmark with $T_n/T_c \approx 0.994$, where they observed hydrodynamic obstruction, consistent with our findings. Ref. [62] also reported fluid relaxation leading to the formation of a shell, although, in that study, the numerical framework assumed a fixed wall velocity, meaning that the emergence of a steady-state profile was a direct consequence of this prior assumption rather than an independent outcome of the simulation.

Our results suggest that the assumption of immediate stationarity, inherent to the matching method, overlooks the crucial role of early-stage dynamics in determining the long-term behaviour of the bubble wall. In [3] we introduced a selection rule for identifying whether a stationary state is dynamically realized. However, applying this criterion requires going beyond local thermal equilibrium and analysing the system's asymptotic behaviour as the friction parameter vanishes, a topic we explore in the next

Benchmark	α_θ	Ψ_n	$w_s(T_n)$ [GeV^4]	T_n [GeV]	h_0 [GeV]	$L_w^{\rm app}$ [GeV^{-1}]
B_1	0.0072	0.979	3.87×10^9	96.8	172	0.181
B_2	0.0103	0.972	2.94×10^9	90.6	182	0.079

Table 4.2: *Benchmark realisations of the xSM model: benchmark B_1 is an example of the model which evolves towards stationary subsonic deflagration in the limit of $\eta \to 0$. In the same limit benchmark B_2 evolves as the ultra-relativistic detonation, although the analytical deflagration solution, predicted by the LTE equations, exists. The scan with respect to the friction parameter η is presented on Fig. 4.12.*

section.

4.7 Real-time evolution of the bubble beyond LTE

Building on our previous analysis, we now extend our study by incorporating non-equilibrium effects, which are essential for capturing the full dynamics of the bubble-wall evolution. In particular, we focus on the limit where friction arises solely from the coupling to the Higgs field, adopting the assumption $\eta_h = \eta$ and $\eta_s = 0$, similarly as in [32, 33].

As discussed in Chapter 3, the generalized third matching equation (3.39) yields two types of steady-state solutions: deflagrations/hybrids, whose wall velocity approaches the LTE prediction in the limit $\eta \to 0$, and stable detonations, which for $\eta \to 0$ reach $\xi_w \to 1$. Here, we compare these analytical predictions with the results of real-time simulations for benchmark points representing both categories (see Table 4.2).

To express the friction parameter η used in hydrodynamic simulations in terms of the normalized friction parameter $\tilde{\eta}$, it is crucial to determine the wall width L_w for the stationary field profile. Since solving the full system of equations is computationally demanding, we employ a simple analytical approximation:

$$L_w \approx \frac{h_0}{\sqrt{8V_b|_{T_c}}} \tag{4.18}$$

which depends on the Higgs VEV h_0 and the potential barrier between the supercooled and true vacua on the tunneling path, evaluated at the *critical* temperature. Despite its

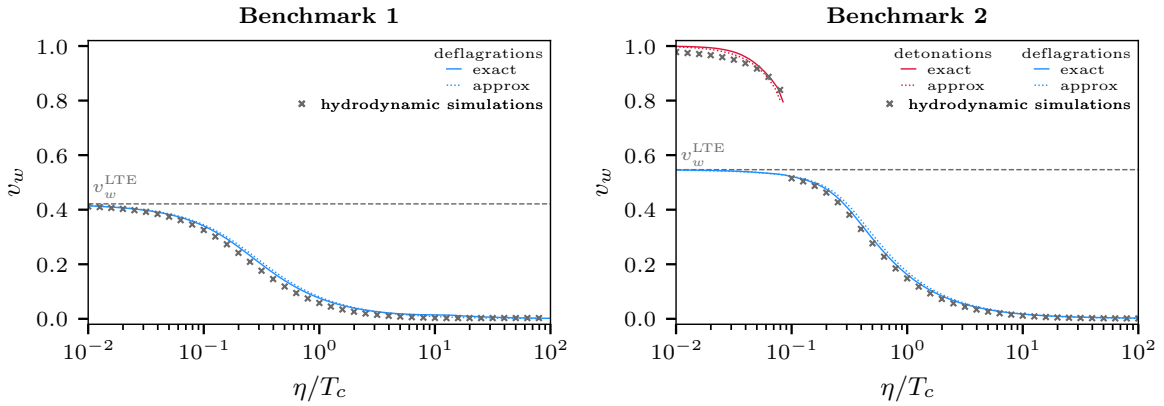

Figure 4.12: *The bubble-wall velocity v_w in the stationary state plotted against the effective friction parameter η for two benchmarks (see Table 4.2). Red and blue curves represent the analytical results with the third matching condition beyond LTE given with eq. (3.39). Solid and dotted lines denote different methods of bubble-wall width evaluation: the exact value measured from the simulation, and the simple analytical approximation (4.18). Gray dashed lines mark the standard LTE analytical results (see [34]), while grey crosses represent the results of real-time lattice simulations with the full equations of motion of the system.*

simplicity, this expression provides a remarkably accurate estimate of the wall velocity. A more detailed justification for eq. (4.18), along with a comparison to wall widths extracted from lattice simulations, is presented in the Appendix B.

Fig. 4.12 presents our predictions for the terminal wall velocity as a function of the friction coupling η, which is treated as a free parameter and varied across several orders of magnitude. The grey crosses denote values obtained directly from the simulations, while the solid and dashed lines depict our steady-state predictions, based on the extended matching conditions. The deflagration/hybrid branch of solutions is shown in blue, and the detonation branch is marked in red, following the convention of Fig. 3.5. The solid lines correspond to the analytical estimates discussed in Chapter 3, with the wall width extracted from simulations. In contrast, the dashed lines employ the simplified approximation from eq. (4.18). The close agreement between the two demonstrates that the uncertainty introduced by this approximation is minimal. Finally, the horizontal grey dashed line indicates the wall velocity in the LTE limit.

The left panel corresponds to a benchmark with $\alpha_\theta < \alpha_{\mathrm{LTE}}$, where hydrodynamic

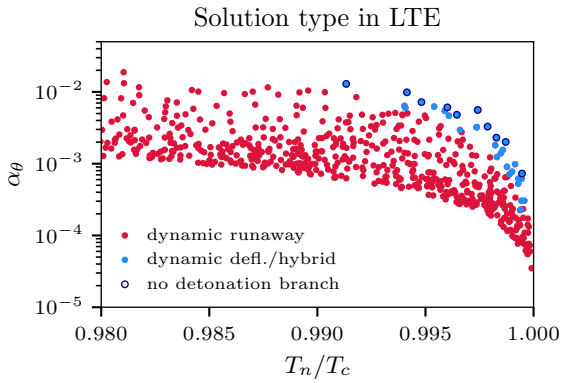

Figure 4.13: *Solution types in the LTE regime as predicted by lattice simulations. In the plotted region, a stationary LTE solution is dynamically realized only at the benchmarks marked in blue, while for those marked in red, the wall undergoes runaway expansion. The dark blue rim highlights points where the analytical computation does not predict the existence of a detonation branch, implying that the system should evolve into a deflagration or hybrid solution. This analytical prediction is confirmed by lattice simulations, which consistently converge to deflagration/hybrid solutions for all rimmed benchmarks.*

obstruction in the LTE limit prevents further acceleration, leading to a stationary state. In contrast, the right panel shows a case with $\alpha_\theta > \alpha_{\text{LTE}}$, for which two distinct steady-states are kinematically allowed in the limit of low η. When multiple stable asymptotic solutions exist for the partial differencial equation, the initial conditions determine which one is realized. Our simulations, starting from a nucleating bubble, indicate a strong preference for the faster solution. This occurs because the fluid shell is still forming when the wall surpasses the velocity of the slower solution, and at that stage, the friction profile does not yet resemble the asymptotic form assumed in analytical approaches.

To verify the accuracy of our selection rule, we applied it to the previously studied sample. As shown in Fig. 4.13, all benchmark points for which our method does not predict the existence of a detonation branch dynamically evolve into stationary deflagrations or hybrid solutions. This suggests that the absence of a detonation branch serves as a sufficient condition for steady-state expansion.

The remaining deflagration/hybrid solutions may result from small numerical friction inherent in the simulations due to unavoidable imperfections of the numerical

scheme. Another source of uncertainty stems from the approximations used in derivation of the analytical relation between friction and velocity. Additionally, we cannot exclude the possibility that the deflagrations/hybrids observed in numerical simulations, but not predicted by our condition, accelerate slowly enough to form heated fluid shells that inhibit further acceleration before reaching the Jouguet velocity, ultimately settling into a stationary state with a finite terminal velocity. As suggested by Fig. 4.13, such cases appear to be highly fine-tuned. In the vast majority of the parameter space, bubbles expand as runaways in the LTE approximation whenever the detonation branch is present.

CHAPTER 5

Summary

Understanding the dynamics of cosmological first-order phase transitions is essential, as the next generation of gravitational wave detectors promises to explore the Early Universe with unprecedented sensitivity. This dissertation aimed to present our study of vacuum bubble evolution during these transitions, offering a more comprehensive framework for modelling their dynamics and bridging the gap between analytical predictions and numerical simulations.

Our first objective was to understand how stationary states emerge within a finite time during the expansion of true vacuum bubbles. To this end, we developed numerical lattice simulations, exploiting the system's spherical symmetry to study the real-time evolution of a single, spherically symmetric bubble. By comparing the resulting field and fluid profiles with well-established analytical solutions based on the bag model, we found a good level of agreement in their overall structure and asymptotic behaviour.

A key observation, however, was that the hydrodynamical obstruction preventing the realization of the fastest deflagration and hybrid solutions appears to be a universal feature. We consistently found that certain branches of solutions are excluded, with the gap in allowed wall velocities widening as the nucleation temperature predicted by the potential approaches the critical temperature at which the two minima become degenerate. In extreme cases, even detonation solutions were fully suppressed. These

aspects of our study were primarily discussed in [1].

Next, focusing on the bubble-wall velocity under the assumption of local thermal equilibrium, we confirmed that equilibrium backreaction alone can sustain steady-state expansion. Whenever such stationary states emerged in our simulations, the resulting wall velocity closely matched recent predictions based on the matching equations [34]. However, this behavior proved to be highly exceptional and required a finely tuned nucleation temperature. Indeed, steady expansion was only possible when supercooling was negligible, that is, for transitions with $T_n/T_c \approx 1$.

These results indicate that, in the absence of non-equilibrium friction, bubble expansion typically leads to runaway behavior. During the early stages of their evolution, nucleated bubbles accelerate rapidly while the surrounding heated fluid shell is still forming. In most cases, the walls exceed the Jouguet velocity and begin transitioning into detonations before the fluid profile has time to stabilize. Once this stage is reached, the bubble continues to accelerate indefinitely, even though a steady-state solution exists in which vacuum pressure would balance the driving force at a lower velocity. These findings for local thermal equilibrium were presented in [2].

To extend our analysis beyond the local thermal equilibrium and include the effective friction present in realistic models, we refined the analytical computation of the wall velocity by incorporating an updated matching condition that accounts for entropy production. This improvement allowed us to identify a new branch of solutions consisting of stable detonations that, in the limit of vanishing friction, smoothly transition into runaway solutions.

To verify these predictions, we performed real-time lattice simulations. We found that the analytical solutions closely match the simulation results, allowing us to predict the behaviour of solutions across the entire model parameter space. Specifically, we discovered that above a critical phase transition strength, there is no gap between the velocities of the two solution branches, meaning all profiles are kinematically allowed. Below this threshold, deflagration/hybrid solutions often coexist with the new detonation branch, with a velocity gap separating them. Most importantly, our real-time simulations demonstrate that the faster detonation solution is strongly favoured in these cases.

It is worth noting that our updated third matching condition enables the determination of the friction-dependent bubble-wall velocity without the need for simulations. Additionally, it constrains the range of possible solutions and predicts the size of the velocity gap. A simple rule of thumb we propose is that whenever a detonation result appears on top of the regular deflagration/hybrid solution, it should be treated as the physical one. The code for searching the steady-state velocity v_w as a function of model parameters and effective friction $\tilde{\eta}$ is available online [115]. This part of the results is discussed in [3].

The main limitations of the method stem from the range of applicability of the ansatz used for the entropy source. While these challenges could potentially be addressed by applying the Chapman-Enskog expansion of the Boltzmann equation for particles interacting with the wall, a more fundamental difficulty lies in determining the precise value of the η parameter. This parameter is essential for assessing how far the system is from local thermal equilibrium. Some valuable insights can be derived from the ballistic limit, which provides an upper bound on entropy production and suggests a maximum possible value for η. A more thorough investigation of these issues we will be addressed in future works.

From a phenomenological perspective, our findings have important implications for electroweak baryogenesis. In particular, if the early-time dynamics of bubble walls significantly influence their eventual evolution, as our results suggest, then many regions of parameter space previously considered viable may no longer support successful baryogenesis. This is because electroweak baryogenesis requires sufficiently slow-moving walls [96], typically realized in hybrid or deflagration solutions, whereas, according to our analysis, detonations emerge as the more generic outcome. As a result, scenarios capable of providing the necessary out-of-equilibrium conditions for baryon asymmetry generation may be substantially constrained. This highlights the need to re-examine existing baryogenesis studies that do not incorporate the dynamical selection of steady-state solutions during bubble growth.

By contrast, the consequences for gravitational wave signals are less restrictive. Although the inclusion of early-time dynamics alters the evolution of the wall and may affect its final velocity in certain regions, these changes typically occur in transitions that are already too weak to produce observable gravitational waves. In other

words, the scenarios where dynamical effects are most pronounced tend to correspond to phase transitions below the sensitivity threshold of future interferometers such as LISA. Therefore, while our results refine the theoretical understanding of bubble-wall dynamics, they do not significantly change the prospects for gravitational wave detection from cosmological first-order phase transitions.

To summarize, we have demonstrated that the early stages of bubble evolution during cosmological phase transitions can significantly impact the resulting phenomenology. In particular, assuming local thermal equilibrium during these early times typically leads to a runaway solution, even when analytical methods predict a small terminal velocity. Introducing the effective friction term allows for a better understanding and control of this effect, providing a useful selection rule to determine whether the deflagration solution is physical. This has profound implications for our understanding of the phase transition dynamics and may impact some of the cosmological observables in considered theories.

APPENDIX A

Sensitivity curves for LISA

Following [137], we will review the construction of sensitivity curves for LISA. Dominant sources of noise are due to acceleration and optical path-length fluctuations, characterized with their amplitudes as

$$\sqrt{(\delta a^2)} = 3 \times 10^{-15}\,\mathrm{m/s^2}, \qquad \sqrt{(\delta x^2)} = 1.5 \times 10^{-11}\,\mathrm{m}. \tag{A.1}$$

They constitute main sources of the noise, given by

$$S_I(f) = 4\left(\sqrt{(\delta a^2)}/L\right)^2 \left(1 + (f_1/f_f)^2\right)\,\mathrm{Hz^{-1}} \approx 5.76 \times 10^{-48}\left(1 + (f_1/f)^2\right)\,\mathrm{s^{-4}\,Hz^{-1}} \tag{A.2}$$

$$S_{II}(f) = 4\left(\sqrt{(\delta x^2)}/L\right)^2\,\mathrm{Hz^{-1}} \approx 3.6 \times 10^{-41}\,\mathrm{Hz^{-1}} \tag{A.3}$$

The effective noise can be modelled as

$$S_{\mathrm{eff}}(f) = \frac{10}{3}\left(\frac{S_I(f)}{(2\pi f)^4} + S_{II}(f)\right) R(f) + S_{\mathrm{GAL}}(f), \tag{A.4}$$

with the response function

$$R(f) = \left(1 + (f_2/f)^2\right). \tag{A.5}$$

We use LISA arm length $L = 2.5 \times 10^9\,\mathrm{m}$ and characteristic frequencies $f_1 = 0.4\,\mathrm{mHz}$ and $f_2 = 25\,\mathrm{mHz}$. The galactic confusion noise is produced by the white dwarves and

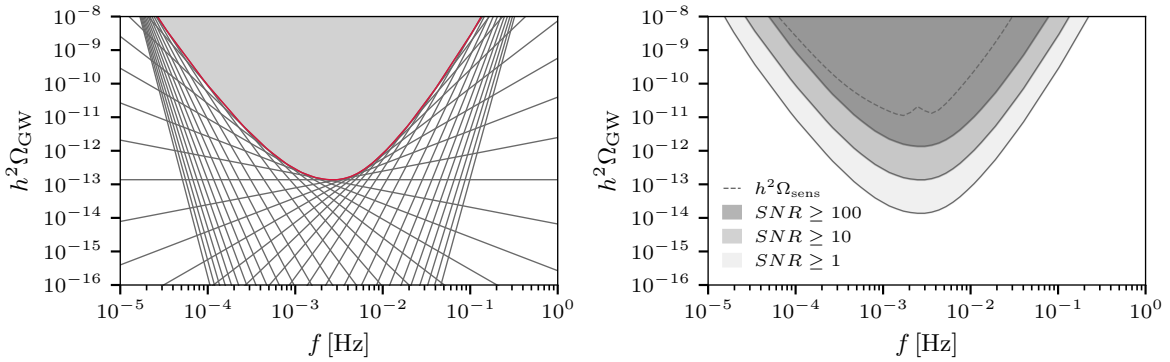

Figure A.1: *Left panel: Computation of the power law sensitivity for* $SNR = 10$. *The gray lines represent power law signals* (A.9) *with different slopes* n, *while the red line correspond to resulting envelope. Gray-shaded region denotes the region for which signal-to-noise ratio is greater than the threshold value.*
Right panel: Power law sensitivity for different values of SNR *(denoted with different shades of gray) compared with LISA sensitivity curve* (A.8) *(denoted with a dashed line).*

can be approximated with the following analytic fit

$$S_{\rm GAL}(f) = Af^{-7/3}\exp(-(f/f_3)^{\alpha})\,\frac{1}{2}\left[1+\tanh\left(\frac{f-f_k}{f_4}\right)\right], \tag{A.6}$$

with $A = 1.14\times10^{-44}$, $\alpha = 1.8$ and $f_4 = 0.31\,\text{mHz}$. The frequencies f_3 and f_k depend on the observational time $T_{\rm obs}$ through the following relations

$$\log_{10}(f_3) = a_3\log_{10}(T_{\rm obs}) + b_3, \qquad \log_{10}(f_k) = a_k\log_{10}(T_{\rm obs}) + b_k, \tag{A.7}$$

where the best fit parameters are $a_3 = -0.25$, $b_3 = -2.7$, $a_k = -0.27$, $b_k = -2.47$ and obrervational time $T_{\rm obs}$ is here given in years.

The quantity typically used to describe the sensitivity to SGWB is the energy density sensitivity defined by

$$\Omega_{\rm sens}(f) = \frac{4\pi^2}{3H_0^2}f^3 S_{\rm eff}(f) \tag{A.8}$$

and the signal-to-noise ratio for a given signal can be estimated using eq. (1.54). In order to estimate the detectability of a simple power law signal in the form

$$\Omega_{\rm GW}(f) = \Omega_n(f/f_{\rm ref})^n, \tag{A.9}$$

the power law sensitivity was introduced. It is computed as the envelope of all power law curves with different slopes n for fixed SNR. Example of such a construction

is presented in the left panel of Fig. A.1, while on the right panel resulting power law curves for three different values of SNR are compared with LISA sensitivity curve (A.8).

APPENDIX B

Field profile widths

The bubble-wall width is a key parameter characterizing the structure and evolution of the expanding bubble during a first-order phase transition. In particular, it plays a significant role in determining the friction acting on the wall, and appears explicitly in our modified third matching condition beyond the local thermal equilibrium (LTE) approximation, see eqs. (3.39) and (3.40).

In this appendix, we review several methods for estimating the wall width based solely on the form of the effective potential at the nucleation temperature. We derive an analytic approximation in the single-field limit, discuss its generalization to multi-field configurations, and compare it with prescriptions proposed in the literature. These methods are then confronted with numerically extracted profiles from the lattice simulations.

We begin with the scalar field equation of motion (4.7), written in the planar-wall approximation, in which the curvature of the bubble is neglected. This simplification is justified, as the associated corrections are suppressed by the inverse of the bubble radius and are negligible at late stages of bubble evolution.

To obtain an equation for the stationary profile in the rest frame of the wall, we set all time derivatives of the scalar field ϕ to zero. Moreover, for weak and moderately strong transitions, lattice simulations indicate that the friction term can be neglected,

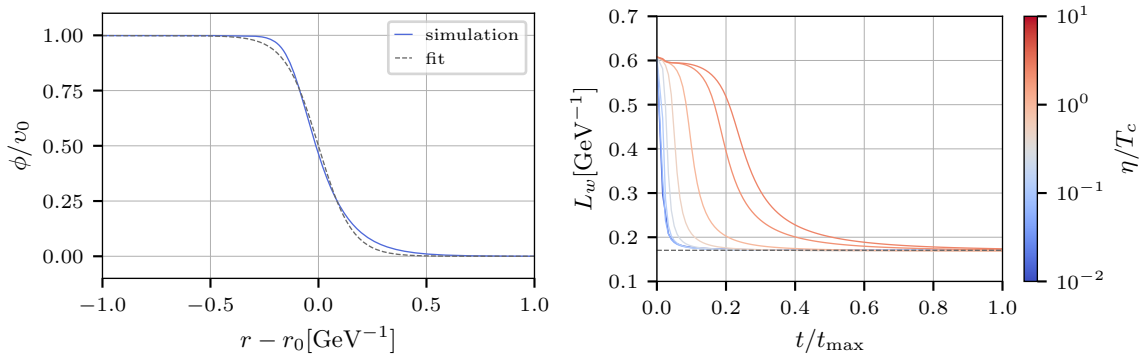

Figure B.1: ***Left panel:*** *example of the field profile from the real-time simulation at its final time $t = t_{max}$ compared with the fit given with eq. (B.3).* ***Right panel:*** *time evolution of L_w for* ***Benchmark 1*** *of xSM (see Table 4.2). Different colours represent different values of the effective friction parameter η. The asymptotic value L_w is achieved in the whole spectrum of η values.*

at least in the case of deflagrations and hybrid solutions. Under these assumptions, the equation reduces to a one-dimensional differential equation:

$$\frac{d^2\phi}{dz^2} - \frac{\partial V_{\text{eff}}}{\partial \phi} = 0, \tag{B.1}$$

which describes the shape of the bubble wall in terms of the scalar field profile $\phi(z)$. To simplify the analysis, we restrict our attention to transitions for which the nucleation and critical temperatures are close, i.e. $T_n \sim T_c$ so that the temperature can be treated as approximately constant across the wall. This assumption is justified in the region of the xSM parameter space where deflagrations and hybrid solutions are dynamically realized in the local thermal equilibrium limit [2]. Under this approximation, the scalar field profile can be reliably determined by solving the equation of motion at the critical temperature:

$$\frac{d^2\phi}{dz^2} = \frac{\partial V_{\text{eff}}(\phi, T = T_c)}{\partial \phi}. \tag{B.2}$$

The expression for the profile width is obtained by substituting the hyperbolic tangent ansatz into the equation of motion:

$$\phi = \frac{v_0}{2}\left[1 - \tanh\left(\frac{z}{L}\right)\right]. \tag{B.3}$$

For a single-field potential, parametrized for instance as $V = \lambda/4\phi^2(\phi - \phi_0)^2$ this yields the well-known result [4, 138]

$$L_w = \frac{v_0}{\sqrt{8V_b}}, \tag{B.4}$$

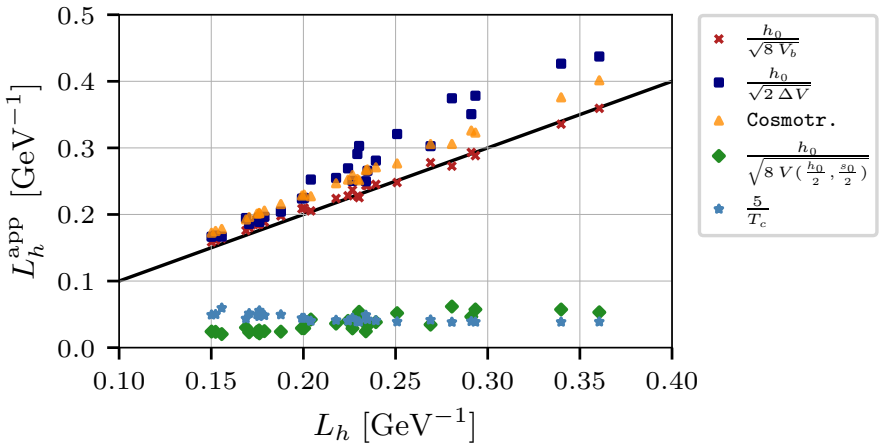

Figure B.2: *Different approximations for the Higgs field profile width at the steady state L_h^{app}, plotted against values obtained in lattice simulations L_h.*

where v_0 is the scalar VEV at broken vacuum, while V_b is the barrier height. In the multi-field case, the generalization of formula (B.4) remains accurate, provided that V_b is evaluated along the tunnelling path. Alternatively, a phenomenological approximation can be used that does not require computing the tunneling path

$$L_w \approx \frac{v_0}{\sqrt{2\Delta V_{\rm eff}}}, \tag{B.5}$$

where $\Delta V_{\rm eff}$ denotes the potential difference between the false and true vacua, typically evaluated at the nucleation temperature.

These estimates, along with other commonly used approximations from the literature [4, 29, 73, 138], have been compared with data from lattice simulations of bubble expansion within the xSM model (see Fig. B.2). The lattice results for L_h were obtained by fitting a hyperbolic tangent function, as given in eq. (B.3), to the field profiles from the lattice simulations. An example of such a fit is shown in the left panel of Fig. B.1, while the right panel presents the time evolution of the fitted wall width as it approaches the stationary limit. Notably, within the deflagration/hybrid branch, the asymptotic value of L_w is independent of the effective friction η, which justifies the omission of the friction term in eq. (B.1).

While all the analyzed methods correctly predict the order of magnitude of the Higgs profile width L_h, the exact values often differ significantly from the lattice results. The most accurate predictions, within 6% from the lattice values, are obtained with (B.4). The simpler estimate in equation (B.5) also provides a surprisingly good approximation

for smaller profile widths, but for larger values of L_h it tends to overestimate the lattice results by up to 35%. Additionally, we include in our comparison the built-in routine from `CosmoTransitions` [85] that calculates the profile of the wall moving through the plasma, which should not be confused with the routine used for computing the critical profile. This method also slightly overestimates the lattice results, with deviations remaining under 15%. The simple estimate assuming a symmetric barrier, given by

$$L_h \approx \frac{h_0}{\sqrt{8V_{\text{eff}}(\frac{h_0}{2}, \frac{s_0}{2})}}, \tag{B.6}$$

underestimates the profile widths by a factor of 5 to 8 compared to the lattice results. Additionally, the approximation based on the critical temperature,

$$L_h \approx \frac{5}{T_c}, \tag{B.7}$$

also yields significantly smaller values for the xSM Higgs profile widths. To summarize, we recommend using the expression (B.4), which has been employed in the main part of the work.

Bibliography

[1] Tomasz Krajewski, Marek Lewicki, and Mateusz Zych. "Hydrodynamical constraints on the bubble wall velocity". In: *Phys. Rev. D* 108.10 (2023), p. 103523. DOI: 10.1103/PhysRevD.108.103523. arXiv: 2303.18216 [astro-ph.CO].

[2] Tomasz Krajewski, Marek Lewicki, and Mateusz Zych. "Bubble-wall velocity in local thermal equilibrium: hydrodynamical simulations vs analytical treatment". In: *JHEP* 05 (2024), p. 011. DOI: 10.1007/JHEP05(2024)011. arXiv: 2402.15408 [astro-ph.CO].

[3] Tomasz Krajewski et al. "Steady-state bubbles beyond local thermal equilibrium". In: *JHEP* 06 (2025), p. 118. DOI: 10.1007/JHEP06(2025)118. arXiv: 2411.16580 [astro-ph.CO].

[4] Marek Lewicki, Marco Merchand, and Mateusz Zych. "Electroweak bubble wall expansion: gravitational waves and baryogenesis in Standard Model-like thermal plasma". In: *JHEP* 02 (2022), p. 017. DOI: 10.1007/JHEP02(2022)017. arXiv: 2111.02393 [astro-ph.CO].

[5] John Ellis et al. "The scalar singlet extension of the Standard Model: gravitational waves versus baryogenesis". In: *JHEP* 01 (2023), p. 093. DOI: 10.1007/JHEP01(2023)093. arXiv: 2210.16305 [hep-ph].

[6] Maciej Kierkla et al. "From Hubble to Bubble". In: *JHEP* 11 (2023), p. 077. DOI: 10.1007/JHEP11(2023)077. arXiv: 2309.08530 [astro-ph.CO].

[7] Tomasz Krajewski et al. "Thermalization effects on the dynamics of growing vacuum bubbles". In: (Nov. 2024). arXiv: 2411.15094 [hep-ph].

[8] Arno A. Penzias and Robert Woodrow Wilson. "A Measurement of excess antenna temperature at 4080-Mc/s". In: *Astrophys. J.* 142 (1965), pp. 419–421. DOI: 10.1086/148307.

[9] N. W. Boggess et al. "The COBE mission - Its design and performance two years after launch". In: *Astrophys. J.* 397 (1992), pp. 420–429. DOI: 10.1086/171797.

[10] D. N. Spergel et al. "First year Wilkinson Microwave Anisotropy Probe (WMAP) observations: Determination of cosmological parameters". In: *Astrophys. J. Suppl.* 148 (2003), pp. 175–194. DOI: 10.1086/377226. arXiv: astro-ph/0302209.

[11] N. Aghanim et al. "Planck 2018 results. VI. Cosmological parameters". In: *Astron. Astrophys.* 641 (2020). [Erratum: Astron.Astrophys. 652, C4 (2021)], A6. DOI: 10.1051/0004-6361/201833910. arXiv: 1807.06209 [astro-ph.CO].

[12] S. L. Glashow. "Partial Symmetries of Weak Interactions". In: *Nucl. Phys.* 22 (1961), pp. 579–588. DOI: 10.1016/0029-5582(61)90469-2.

[13] Steven Weinberg. "A Model of Leptons". In: *Phys. Rev. Lett.* 19 (1967), pp. 1264–1266. DOI: 10.1103/PhysRevLett.19.1264.

[14] Abdus Salam. "Weak and Electromagnetic Interactions". In: *Conf. Proc. C* 680519 (1968), pp. 367–377. DOI: 10.1142/9789812795915_0034.

[15] G. Arnison et al. "Experimental Observation of Isolated Large Transverse Energy Electrons with Associated Missing Energy at $\sqrt{s} = 540$ GeV". In: *Phys. Lett. B* 122 (1983), pp. 103–116. DOI: 10.1016/0370-2693(83)91177-2.

[16] G. Arnison et al. "Experimental Observation of Lepton Pairs of Invariant Mass Around 95-GeV/c**2 at the CERN SPS Collider". In: *Phys. Lett. B* 126 (1983), pp. 398–410. DOI: 10.1016/0370-2693(83)90188-0.

[17] Georges Aad et al. "Observation of a new particle in the search for the Standard Model Higgs boson with the ATLAS detector at the LHC". In: *Phys. Lett. B* 716 (2012), pp. 1–29. DOI: 10.1016/j.physletb.2012.08.020. arXiv: 1207.7214 [hep-ex].

[18] Serguei Chatrchyan et al. "Observation of a New Boson at a Mass of 125 GeV with the CMS Experiment at the LHC". In: *Phys. Lett. B* 716 (2012), pp. 30–61. DOI: 10.1016/j.physletb.2012.08.021. arXiv: 1207.7235 [hep-ex].

[19] Peter W. Higgs. "Broken Symmetries and the Masses of Gauge Bosons". In: *Phys. Rev. Lett.* 13 (1964). Ed. by J. C. Taylor, pp. 508–509. DOI: 10.1103/PhysRevLett.13.508.

[20] Peter W. Higgs. "Broken symmetries, massless particles and gauge fields". In: *Phys. Lett.* 12 (1964), pp. 132–133. DOI: 10.1016/0031-9163(64)91136-9.

[21] F. Englert and R. Brout. "Broken Symmetry and the Mass of Gauge Vector Mesons". In: *Phys. Rev. Lett.* 13 (1964). Ed. by J. C. Taylor, pp. 321–323. DOI: 10.1103/PhysRevLett.13.321.

[22] B. P. Abbott et al. "Binary Black Hole Mergers in the First Advanced LIGO Observing Run". In: *Physical Review X* 6.4 (Oct. 2016). ISSN: 2160-3308. DOI: 10.1103/physrevx.6.041015. URL: http://dx.doi.org/10.1103/PhysRevX.6.041015.

[23] Pau Amaro-Seoane et al. "Laser Interferometer Space Antenna". In: (Feb. 2017). arXiv: 1702.00786 [astro-ph.IM].

[24] A. D. Sakharov. "Violation of CP Invariance, C asymmetry, and baryon asymmetry of the universe". In: *Pisma Zh. Eksp. Teor. Fiz.* 5 (1967), pp. 32–35. DOI: 10.1070/PU1991v034n05ABEH002497.

[25] V. A. Kuzmin, V. A. Rubakov, and M. E. Shaposhnikov. "On the Anomalous Electroweak Baryon Number Nonconservation in the Early Universe". In: *Phys. Lett. B* 155 (1985), p. 36. DOI: 10.1016/0370-2693(85)91028-7.

[26] Andrew G. Cohen, D. B. Kaplan, and A. E. Nelson. "Progress in electroweak baryogenesis". In: *Ann. Rev. Nucl. Part. Sci.* 43 (1993), pp. 27–70. DOI: 10.1146/annurev.ns.43.120193.000331. arXiv: hep-ph/9302210.

[27] V. A. Rubakov and M. E. Shaposhnikov. "Electroweak baryon number nonconservation in the early universe and in high-energy collisions". In: *Usp. Fiz. Nauk* 166 (1996), pp. 493–537. DOI: 10.1070/PU1996v039n05ABEH000145. arXiv: hep-ph/9603208.

[28] David E. Morrissey and Michael J. Ramsey-Musolf. "Electroweak baryogenesis". In: *New J. Phys.* 14 (2012), p. 125003. DOI: 10.1088/1367-2630/14/12/125003. arXiv: 1206.2942 [hep-ph].

[29] Benoit Laurent and James M. Cline. "Fluid equations for fast-moving electroweak bubble walls". In: *Phys. Rev. D* 102.6 (2020), p. 063516. DOI: 10.1103/PhysRevD.102.063516. arXiv: 2007.10935 [hep-ph].

[30] Marc Barroso Mancha, Tomislav Prokopec, and Bogumila Swiezewska. "Field-theoretic derivation of bubble-wall force". In: *JHEP* 01 (2021), p. 070. DOI: 10.1007/JHEP01(2021)070. arXiv: 2005.10875 [hep-th].

[31] Wen-Yuan Ai, Bjorn Garbrecht, and Carlos Tamarit. "Bubble wall velocities in local equilibrium". In: *JCAP* 03.03 (2022), p. 015. DOI: 10.1088/1475-7516/2022/03/015. arXiv: 2109.13710 [hep-ph].

[32] James M. Cline et al. "Baryogenesis and gravity waves from a UV-completed electroweak phase transition". In: *Phys. Rev. D* 103.12 (2021), p. 123529. DOI: 10.1103/PhysRevD.103.123529. arXiv: 2102.12490 [hep-ph].

[33] Benoit Laurent and James M. Cline. "First principles determination of bubble wall velocity". In: *Phys. Rev. D* 106.2 (2022), p. 023501. DOI: 10.1103/PhysRevD.106.023501. arXiv: 2204.13120 [hep-ph].

[34] Wen-Yuan Ai, Benoit Laurent, and Jorinde van de Vis. "Model-independent bubble wall velocities in local thermal equilibrium". In: (Mar. 2023). arXiv: 2303.10171 [astro-ph.CO].

[35] Mikel Sanchez-Garitaonandia and Jorinde van de Vis. "Prediction of the bubble wall velocity for a large jump in degrees of freedom". In: *Phys. Rev. D* 110.2 (2024), p. 023509. DOI: 10.1103/PhysRevD.110.023509. arXiv: 2312.09964 [hep-ph].

[36] Andreas Ekstedt et al. "How fast does the WallGo? A package for computing wall velocities in first-order phase transitions". In: (Nov. 2024). arXiv: 2411.04970 [hep-ph].

[37] Wen-Yuan Ai, Benoit Laurent, and Jorinde van de Vis. "Bounds on the bubble wall velocity". In: (Nov. 2024). arXiv: 2411.13641 [hep-ph].

[38] J. Ignatius et al. "The growth of bubbles in cosmological phase transitions". In: *Phys. Rev. D* 49 (1994), pp. 3854–3868. DOI: 10.1103/PhysRevD.49.3854. arXiv: astro-ph/9309059.

[39] H. Kurki-Suonio and M. Laine. "On bubble growth and droplet decay in cosmological phase transitions". In: *Phys. Rev. D* 54 (1996), pp. 7163–7171. DOI: 10.1103/PhysRevD.54.7163. arXiv: hep-ph/9512202.

[40] Mark Hindmarsh et al. "Numerical simulations of acoustically generated gravitational waves at a first order phase transition". In: *Phys. Rev. D* 92.12 (2015), p. 123009. DOI: 10.1103/PhysRevD.92.123009. arXiv: 1504.03291 [astro-ph.CO].

[41] Sidney Coleman. "Fate of the false vacuum: Semiclassical theory". In: *Phys. Rev. D* 15 (10 May 1977), pp. 2929–2936. DOI: 10.1103/PhysRevD.15.2929. URL: https://link.aps.org/doi/10.1103/PhysRevD.15.2929.

[42] Curtis G. Callan Jr. and Sidney R. Coleman. "The Fate of the False Vacuum. 2. First Quantum Corrections". In: *Phys. Rev. D* 16 (1977), pp. 1762–1768. DOI: 10.1103/PhysRevD.16.1762.

[43] Andrei D. Linde. "Decay of the False Vacuum at Finite Temperature". In: *Nucl. Phys. B* 216 (1983). [Erratum: Nucl.Phys.B 223, 544 (1983)], p. 421. DOI: 10.1016/0550-3213(83)90072-X.

[44] Mariano Quiros. "Finite temperature field theory and phase transitions". In: *ICTP Summer School in High-Energy Physics and Cosmology*. Jan. 1999, pp. 187–259. arXiv: hep-ph/9901312.

[45] Edward W Kolb and Michael Stanley Turner. *The early universe*. Frontiers in physics. Boulder, CO: Westview Press, 1990. DOI: 10.1201/9780429492860. URL: https://cds.cern.ch/record/206230.

[46] Sidney Coleman. *Aspects of Symmetry: Selected Erice Lectures*. Cambridge University Press, 1985.

[47] Chiara Caprini et al. "Gravitational waves from first-order phase transitions in LISA: reconstruction pipeline and physics interpretation". In: *Journal of Cosmology and Astroparticle Physics* 2024.10 (Oct. 2024), p. 020. ISSN: 1475-7516. DOI:

10.1088/1475-7516/2024/10/020. URL: http://dx.doi.org/10.1088/1475-7516/2024/10/020.

[48] Fred C. Adams. "General solutions for tunneling of scalar fields with quartic potentials". In: *Phys. Rev. D* 48 (1993), pp. 2800–2805. DOI: 10.1103/PhysRevD.48.2800. arXiv: hep-ph/9302321.

[49] Andrei D. Linde. "Fate of the False Vacuum at Finite Temperature: Theory and Applications". In: *Phys. Lett. B* 100 (1981), pp. 37–40. DOI: 10.1016/0370-2693(81)90281-1.

[50] John Ellis, Marek Lewicki, and José Miguel No. "On the Maximal Strength of a First-Order Electroweak Phase Transition and its Gravitational Wave Signal". In: *JCAP* 04 (2019), p. 003. DOI: 10.1088/1475-7516/2019/04/003. arXiv: 1809.08242 [hep-ph].

[51] Chiara Caprini et al. "Detecting gravitational waves from cosmological phase transitions with LISA: an update". In: *JCAP* 03 (2020), p. 024. DOI: 10.1088/1475-7516/2020/03/024. arXiv: 1910.13125 [astro-ph.CO].

[52] Pierre Auclair et al. "Cosmology with the Laser Interferometer Space Antenna". In: *Living Rev. Rel.* 26.1 (2023), p. 5. DOI: 10.1007/s41114-023-00045-2. arXiv: 2204.05434 [astro-ph.CO].

[53] Mark Hindmarsh et al. "Shape of the acoustic gravitational wave power spectrum from a first order phase transition". In: *Phys. Rev. D* 96.10 (2017). [Erratum: Phys.Rev.D 101, 089902 (2020)], p. 103520. DOI: 10.1103/PhysRevD.96.103520. arXiv: 1704.05871 [astro-ph.CO].

[54] Jose R. Espinosa et al. "Energy Budget of Cosmological First-order Phase Transitions". In: *JCAP* 06 (2010), p. 028. DOI: 10.1088/1475-7516/2010/06/028. arXiv: 1004.4187 [hep-ph].

[55] Dario Bettoni et al. "Hubble-Induced Phase Transitions: Gravitational-Wave Imprint of Ricci Reheating from Lattice Simulations". In: (Sept. 2024). arXiv: 2409.15450 [gr-qc].

[56] Andreas Mantziris and Orfeu Bertolami. "Gravitational waves from a curvature-induced phase transition of a Higgs-portal dark matter sector". In: (July 2024). arXiv: 2407.18845 [astro-ph.CO].

[57] Dario Bettoni, Asier Lopez-Eiguren, and Javier Rubio. "Hubble-induced phase transitions on the lattice with applications to Ricci reheating". In: *JCAP* 01.01 (2022), p. 002. DOI: 10.1088/1475-7516/2022/01/002. arXiv: 2107.09671 [hep-ph].

[58] Giorgio Laverda and Javier Rubio. "Ricci Reheating Reloaded". In: (July 2023). arXiv: 2307.03774 [astro-ph.CO].

[59] Dario Bettoni and Javier Rubio. "Hubble-induced phase transitions: Walls are not forever". In: *JCAP* 01 (2020), p. 002. DOI: 10.1088/1475-7516/2020/01/002. arXiv: 1911.03484 [astro-ph.CO].

[60] Mark Hindmarsh et al. "Gravitational waves from the sound of a first order phase transition". In: *Phys. Rev. Lett.* 112 (2014), p. 041301. DOI: 10.1103/PhysRevLett.112.041301. arXiv: 1304.2433 [hep-ph].

[61] Chiara Caprini et al. "Gravitational waves from decaying sources in strong phase transitions". In: (Sept. 2024). arXiv: 2409.03651 [gr-qc].

[62] Ryusuke Jinno et al. "Higgsless simulations of cosmological phase transitions and gravitational waves". In: *JCAP* 02 (2023), p. 011. DOI: 10.1088/1475-7516/2023/02/011. arXiv: 2209.04369 [astro-ph.CO].

[63] Felix Giese, Thomas Konstandin, and Jorinde van de Vis. "Model-independent energy budget of cosmological first-order phase transitions—A sound argument to go beyond the bag model". In: *JCAP* 07.07 (2020), p. 057. DOI: 10.1088/1475-7516/2020/07/057. arXiv: 2004.06995 [astro-ph.CO].

[64] John McDonald. "Electroweak baryogenesis and dark matter via a gauge singlet scalar". In: *Phys. Lett. B* 323 (1994), pp. 339–346. DOI: 10.1016/0370-2693(94)91229-7.

[65] J. R. Espinosa and M. Quiros. "The Electroweak phase transition with a singlet". In: *Phys. Lett. B* 305 (1993), pp. 98–105. DOI: 10.1016/0370-2693(93)91111-Y. arXiv: hep-ph/9301285.

[66] Jose Ramon Espinosa and Mariano Quiros. "Novel Effects in Electroweak Breaking from a Hidden Sector". In: *Phys. Rev. D* 76 (2007), p. 076004. DOI: 10.1103/PhysRevD.76.076004. arXiv: hep-ph/0701145.

[67] Stefano Profumo, Michael J. Ramsey-Musolf, and Gabe Shaughnessy. "Singlet Higgs phenomenology and the electroweak phase transition". In: *JHEP* 08 (2007), p. 010. DOI: 10.1088/1126-6708/2007/08/010. arXiv: 0705.2425 [hep-ph].

[68] Jose R. Espinosa, Thomas Konstandin, and Francesco Riva. "Strong Electroweak Phase Transitions in the Standard Model with a Singlet". In: *Nucl. Phys. B* 854 (2012), pp. 592–630. DOI: 10.1016/j.nuclphysb.2011.09.010. arXiv: 1107.5441 [hep-ph].

[69] Vernon Barger et al. "Strongly First Order Phase Transitions Near an Enhanced Discrete Symmetry Point". In: *Phys. Lett. B* 710 (2012), pp. 1–7. DOI: 10.1016/j.physletb.2012.02.040. arXiv: 1112.5460 [hep-ph].

[70] James M. Cline and Kimmo Kainulainen. "Electroweak baryogenesis and dark matter from a singlet Higgs". In: *JCAP* 01 (2013), p. 012. DOI: 10.1088/1475-7516/2013/01/012. arXiv: 1210.4196 [hep-ph].

[71] Tommi Alanne, Kimmo Tuominen, and Ville Vaskonen. "Strong phase transition, dark matter and vacuum stability from simple hidden sectors". In: *Nucl. Phys. B* 889 (2014), pp. 692–711. DOI: 10.1016/j.nuclphysb.2014.11.001. arXiv: 1407.0688 [hep-ph].

[72] David Curtin, Patrick Meade, and Chiu-Tien Yu. "Testing Electroweak Baryogenesis with Future Colliders". In: *JHEP* 11 (2014), p. 127. DOI: 10.1007/JHEP11(2014)127. arXiv: 1409.0005 [hep-ph].

[73] Ville Vaskonen. "Electroweak baryogenesis and gravitational waves from a real scalar singlet". In: *Phys. Rev. D* 95.12 (2017), p. 123515. DOI: 10.1103/PhysRevD.95.123515. arXiv: 1611.02073 [hep-ph].

[74] Gowri Kurup and Maxim Perelstein. "Dynamics of Electroweak Phase Transition In Singlet-Scalar Extension of the Standard Model". In: *Phys. Rev. D* 96.1 (2017), p. 015036. DOI: 10.1103/PhysRevD.96.015036. arXiv: 1704.03381 [hep-ph].

[75] Ankit Beniwal et al. "Gravitational wave, collider and dark matter signals from a scalar singlet electroweak baryogenesis". In: *JHEP* 08 (2017), p. 108. DOI: 10.1007/JHEP08(2017)108. arXiv: 1702.06124 [hep-ph].

[76] Ankit Beniwal et al. "Gravitational waves and electroweak baryogenesis in a global study of the extended scalar singlet model". In: *JHEP* 02 (2019), p. 183. DOI: 10.1007/JHEP02(2019)183. arXiv: 1810.02380 [hep-ph].

[77] Lauri Niemi, Philipp Schicho, and Tuomas V. I. Tenkanen. "Singlet-assisted electroweak phase transition at two loops". In: *Phys. Rev. D* 103.11 (2021), p. 115035. DOI: 10.1103/PhysRevD.103.115035. arXiv: 2103.07467 [hep-ph].

[78] Marek Lewicki et al. "Impact of theoretical uncertainties on model parameter reconstruction from GW signals sourced by cosmological phase transitions". In: *Phys. Rev. D* 110.2 (2024), p. 023538. DOI: 10.1103/PhysRevD.110.023538. arXiv: 2403.03769 [hep-ph].

[79] Oliver Gould and Paul Saffin. "Perturbative gravitational wave predictions for the real-scalar extended Standard Model". In: (Nov. 2024). arXiv: 2411.08951 [hep-ph].

[80] Michael J. Ramsey-Musolf, Tuomas V. I. Tenkanen, and Van Que Tran. "Refining Gravitational Wave and Collider Physics Dialogue via Singlet Scalar Extension". In: (Sept. 2024). arXiv: 2409.17554 [hep-ph].

[81] James M. Cline et al. "Update on scalar singlet dark matter". In: *Phys. Rev. D* 88 (2013). [Erratum: Phys.Rev.D 92, 039906 (2015)], p. 055025. DOI: 10.1103/PhysRevD.88.055025. arXiv: 1306.4710 [hep-ph].

[82] Georges Aad et al. "Combined Measurement of the Higgs Boson Mass in pp Collisions at $\sqrt{s} = 7$ and 8 TeV with the ATLAS and CMS Experiments". In: *Phys. Rev. Lett.* 114 (2015), p. 191803. DOI: 10.1103/PhysRevLett.114.191803. arXiv: 1503.07589 [hep-ex].

[83] Ken'ichi Saikawa and Satoshi Shirai. "Primordial gravitational waves, precisely: The role of thermodynamics in the Standard Model". In: *JCAP* 05 (2018), p. 035. DOI: 10.1088/1475-7516/2018/05/035. arXiv: 1803.01038 [hep-ph].

[84] Parsa Ghorbani. "Vacuum structure and electroweak phase transition in singlet scalar dark matter". In: *Phys. Dark Univ.* 33 (2021), p. 100861. DOI: 10.1016/j.dark.2021.100861. arXiv: 2010.15708 [hep-ph].

[85] Carroll L. Wainwright. "CosmoTransitions: Computing Cosmological Phase Transition Temperatures and Bubble Profiles with Multiple Fields". In: *Comput. Phys. Commun.* 183 (2012), pp. 2006–2013. DOI: 10.1016/j.cpc.2012.04.004. arXiv: 1109.4189 [hep-ph].

[86] Vernon Barger et al. "CERN LHC phenomenology of an extended standard model with a real scalar singlet". In: *Physical Review D* 77.3 (Feb. 2008). ISSN: 1550-2368. DOI: 10.1103/physrevd.77.035005. URL: http://dx.doi.org/10.1103/PhysRevD.77.035005.

[87] Georges Aad et al. "Search for invisible decays of a Higgs boson using vector-boson fusion in *pp* collisions at $\sqrt{s} = 8$ TeV with the ATLAS detector". In: *JHEP* 01 (2016), p. 172. DOI: 10.1007/JHEP01(2016)172. arXiv: 1508.07869 [hep-ex].

[88] Vardan Khachatryan et al. "Searches for invisible decays of the Higgs boson in pp collisions at $\sqrt{s} = 7$, 8, and 13 TeV". In: *JHEP* 02 (2017), p. 135. DOI: 10.1007/JHEP02(2017)135. arXiv: 1610.09218 [hep-ex].

[89] Florian Goertz et al. "Higgs Boson self-coupling measurements using ratios of cross sections". In: *JHEP* 06 (2013), p. 016. DOI: 10.1007/JHEP06(2013)016. arXiv: 1301.3492 [hep-ph].

[90] Vernon Barger et al. "Higgs-Pair Production and Measurement of the Triscalar Coupling at LHC(8,14)". In: *Phys. Lett. B* 728 (2014), pp. 433–436. DOI: 10.1016/j.physletb.2013.12.013. arXiv: 1311.2931 [hep-ph].

[91] R. Contino et al. "Physics at a 100 TeV pp collider: Higgs and EW symmetry breaking studies". In: (June 2016). DOI: 10.23731/CYRM-2017-003.255. arXiv: 1606.09408 [hep-ph].

[92] M. Bicer et al. "First Look at the Physics Case of TLEP". In: *JHEP* 01 (2014). Ed. by Norman A. Graf, Michael E. Peskin, and Jonathan L. Rosner, p. 164. DOI: 10.1007/JHEP01(2014)164. arXiv: 1308.6176 [hep-ex].

[93] Guy D. Moore and Tomislav Prokopec. "Bubble wall velocity in a first order electroweak phase transition". In: *Phys. Rev. Lett.* 75 (1995), pp. 777–780. DOI: 10.1103/PhysRevLett.75.777. arXiv: hep-ph/9503296.

[94] Guy D. Moore and Tomislav Prokopec. "How fast can the wall move? A Study of the electroweak phase transition dynamics". In: *Phys. Rev. D* 52 (1995), pp. 7182–7204. DOI: 10.1103/PhysRevD.52.7182. arXiv: hep-ph/9506475.

[95] Glauber C. Dorsch and Daniel A. Pinto. "Bubble wall velocities with an extended fluid Ansatz". In: (Dec. 2023). arXiv: 2312.02354 [hep-ph].

[96] James M. Cline and Kimmo Kainulainen. "Electroweak baryogenesis at high bubble wall velocities". In: *Phys. Rev. D* 101.6 (2020), p. 063525. DOI: 10.1103/PhysRevD.101.063525. arXiv: 2001.00568 [hep-ph].

[97] Glauber C. Dorsch, Stephan J. Huber, and Thomas Konstandin. "On the wall velocity dependence of electroweak baryogenesis". In: *JCAP* 08 (2021), p. 020. DOI: 10.1088/1475-7516/2021/08/020. arXiv: 2106.06547 [hep-ph].

[98] Glauber C. Dorsch, Stephan J. Huber, and Thomas Konstandin. "A sonic boom in bubble wall friction". In: *JCAP* 04.04 (2022), p. 010. DOI: 10.1088/1475-7516/2022/04/010. arXiv: 2112.12548 [hep-ph].

[99] James M. Cline and Benoit Laurent. "Electroweak baryogenesis from light fermion sources: A critical study". In: *Phys. Rev. D* 104.8 (2021), p. 083507. DOI: 10.1103/PhysRevD.104.083507. arXiv: 2108.04249 [hep-ph].

[100] H. Kurki-Suonio and M. Laine. "Real time history of the cosmological electroweak phase transition". In: *Phys. Rev. Lett.* 77 (1996), pp. 3951–3954. DOI: 10.1103/PhysRevLett.77.3951. arXiv: hep-ph/9607382.

[101] P. John and M. G. Schmidt. "Do stops slow down electroweak bubble walls?" In: *Nucl. Phys. B* 598 (2001). [Erratum: Nucl.Phys.B 648, 449–452 (2003)], pp. 291–305. DOI: 10.1016/S0550-3213(00)00768-9. arXiv: hep-ph/0002050.

[102] Wen-Yuan Ai, Benoit Laurent, and Jorinde van de Vis. "Bounds on the bubble wall velocity". In: *Journal of High Energy Physics* 2025.2 (Feb. 2025). ISSN: 1029-8479. DOI: 10.1007/jhep02(2025)119. URL: http://dx.doi.org/10.1007/JHEP02(2025)119.

[103] Felix Giese et al. "Model-independent energy budget for LISA". In: *JCAP* 01 (2021), p. 072. DOI: 10.1088/1475-7516/2021/01/072. arXiv: 2010.09744 [astro-ph.CO].

[104] Paul Joseph Steinhardt. "Relativistic Detonation Waves and Bubble Growth in False Vacuum Decay". In: *Phys. Rev. D* 25 (1982), p. 2074. DOI: 10.1103/PhysRevD.25.2074.

[105] Thomas Konstandin and Jose M. No. "Hydrodynamic obstruction to bubble expansion". In: *JCAP* 02 (2011), p. 008. DOI: 10.1088/1475-7516/2011/02/008. arXiv: 1011.3735 [hep-ph].

[106] Marc Barroso Mancha, Tomislav Prokopec, and Bogumila Swiezewska. "Field-theoretic derivation of bubble-wall force". In: *JHEP* 01 (2021), p. 070. DOI: 10.1007/JHEP01(2021)070. arXiv: 2005.10875 [hep-th].

[107] Dietrich Bodeker and Guy D. Moore. "Electroweak Bubble Wall Speed Limit". In: *JCAP* 05 (2017), p. 025. DOI: 10.1088/1475-7516/2017/05/025. arXiv: 1703.08215 [hep-ph].

[108] Aleksandr Azatov and Miguel Vanvlasselaer. "Bubble wall velocity: heavy physics effects". In: *JCAP* 01 (2021), p. 058. DOI: 10.1088/1475-7516/2021/01/058. arXiv: 2010.02590 [hep-ph].

[109] Yann Gouttenoire, Ryusuke Jinno, and Filippo Sala. "Friction pressure on relativistic bubble walls". In: *JHEP* 05 (2022), p. 004. DOI: 10.1007/JHEP05(2022)004. arXiv: 2112.07686 [hep-ph].

[110] Stefan Höche et al. "Towards an all-orders calculation of the electroweak bubble wall velocity". In: *JCAP* 03 (2021), p. 009. DOI: 10.1088/1475-7516/2021/03/009. arXiv: 2007.10343 [hep-ph].

[111] Daniel Cutting, Mark Hindmarsh, and David J. Weir. "Vorticity, kinetic energy, and suppressed gravitational wave production in strong first order phase transitions". In: *Phys. Rev. Lett.* 125.2 (2020), p. 021302. DOI: 10.1103/PhysRevLett.125.021302. arXiv: 1906.00480 [hep-ph].

[112] Daniel Cutting, Essi Vilhonen, and David J. Weir. "Droplet collapse during strongly supercooled transitions". In: *Phys. Rev. D* 106.10 (2022), p. 103524. DOI: 10.1103/PhysRevD.106.103524. arXiv: 2204.03396 [astro-ph.CO].

[113] Wen-Yuan Ai, Xander Nagels, and Miguel Vanvlasselaer. "Criterion for ultra-fast bubble walls: the impact of hydrodynamic obstruction". In: *JCAP* 03 (2024), p. 037. DOI: 10.1088/1475-7516/2024/03/037. arXiv: 2401.05911 [hep-ph].

[114] Shyam Balaji, Michael Spannowsky, and Carlos Tamarit. "Cosmological bubble friction in local equilibrium". In: *JCAP* 03 (2021), p. 051. DOI: 10.1088/1475-7516/2021/03/051. arXiv: 2010.08013 [hep-ph].

[115] https://github.com/wedelfach/Bubbles-beyond-LTE.git. URL: https://github.com/wedelfach/Bubbles-beyond-LTE.git.

[116] Dietrich Bodeker and Guy D. Moore. "Can electroweak bubble walls run away?" In: *JCAP* 05 (2009), p. 009. DOI: 10.1088/1475-7516/2009/05/009. arXiv: 0903.4099 [hep-ph].

[117] Marek Lewicki, Ville Vaskonen, and Hardi Veermäe. "Bubble dynamics in fluids with N-body simulations". In: *Phys. Rev. D* 106.10 (2022), p. 103501. DOI: 10.1103/PhysRevD.106.103501. arXiv: 2205.05667 [astro-ph.CO].

[118] Marek Lewicki et al. "Dynamics of false vacuum bubbles with trapped particles". In: *Phys. Rev. D* 108.3 (2023), p. 036023. DOI: 10.1103/PhysRevD.108.036023. arXiv: 2305.07702 [hep-ph].

[119] Mark Hindmarsh and Mulham Hijazi. "Gravitational waves from first order cosmological phase transitions in the Sound Shell Model". In: *JCAP* 12 (2019), p. 062. DOI: 10.1088/1475-7516/2019/12/062. arXiv: 1909.10040 [astro-ph.CO].

[120] Wensheng Tang and Yajuan Sun. "Time finite element methods: A unified framework for numerical discretizations of ODEs". English. In: *Applied Mathematics and Computation* 219.4 (2012), pp. 2158–2179. DOI: 10.1016/j.amc.2012.08.062.

[121] E. Gagarina et al. "Variational space–time (dis)continuous Galerkin method for nonlinear free surface water waves". In: *Journal of Computational Physics* 275 (2014), pp. 459–483. ISSN: 0021-9991. DOI: https://doi.org/10.1016/j.jcp.2014.06.035. URL: https://www.sciencedirect.com/science/article/pii/S0021999114004422.

[122] Shan Zhao and G. W. Wei. "A unified discontinuous Galerkin framework for time integration". In: *Mathematical Methods in the Applied Sciences* 37.7 (2014), pp. 1042–1071. DOI: https://doi.org/10.1002/mma.2863. eprint: https://onlinelibrary.wiley.com/doi/pdf/10.1002/mma.2863. URL: https://onlinelibrary.wiley.com/doi/abs/10.1002/mma.2863.

[123] Cédric M. Campos. "High Order Variational Integrators: A Polynomial Approach". In: *Advances in Differential Equations and Applications*. Ed. by Fernando Casas and Vicente Martínez. Cham: Springer International Publishing, 2014, pp. 249–258. ISBN: 978-3-319-06953-1. DOI: 10.1007/978-3-319-06953-1_24. URL: https://doi.org/10.1007/978-3-319-06953-1_24.

[124] Sina Ober-Blöbaum and Nils Saake. *Construction and analysis of higher order Galerkin variational integrators*. 2014. arXiv: 1304.1398 [math.NA].

[125] E. Gagarina et al. "On variational and symplectic time integrators for Hamiltonian systems". In: *Journal of Computational Physics* 306 (2016), pp. 370–389. ISSN: 0021-9991. DOI: https://doi.org/10.1016/j.jcp.2015.11.049. URL: https://www.sciencedirect.com/science/article/pii/S0021999115007895.

[126] Michael Muehlebach, Thomas Heimsch, and Ch. Glocker. "Variational integrators – A continuous time approach". In: 2016.

[127] Sina Ober-Blöbaum. "Galerkin variational integrators and modified symplectic Runge–Kutta methods". In: *IMA Journal of Numerical Analysis* 37.1 (Feb. 2016), pp. 375–406. ISSN: 0272-4979. DOI: 10.1093/imanum/drv062. eprint: https://academic.oup.com/imajna/article-pdf/37/1/375/9633641/drv062.pdf. URL: https://doi.org/10.1093/imanum/drv062.

[128] D. Kuzmin and S. Turek. "Flux Correction Tools for Finite Elements". In: *Journal of Computational Physics* 175.2 (2002), pp. 525–558. ISSN: 0021-9991.

DOI: https://doi.org/10.1006/jcph.2001.6955. URL: https://www.sciencedirect.com/science/article/pii/S0021999101969554.

[129] D. Kuzmin, M. Möller, and S. Turek. "Multidimensional FEM-FCT schemes for arbitrary time stepping". In: *International Journal for Numerical Methods in Fluids* 42.3 (2003), pp. 265–295. DOI: https://doi.org/10.1002/fld.493. eprint: https://onlinelibrary.wiley.com/doi/pdf/10.1002/fld.493. URL: https://onlinelibrary.wiley.com/doi/abs/10.1002/fld.493.

[130] Matthias Möller. "Algebraic Flux Correction for Nonconforming Finite Element Discretizations of Scalar Transport Problems". In: *Computing* 95.5 (May 2013), pp. 425–448. ISSN: 0010-485X. DOI: 10.1007/s00607-012-0276-y. URL: https://doi.org/10.1007/s00607-012-0276-y.

[131] Dmitri Kuzmin. "A new perspective on flux and slope limiting in discontinuous Galerkin methods for hyperbolic conservation laws". In: *Computer Methods in Applied Mechanics and Engineering* 373 (2021), p. 113569. ISSN: 0045-7825. DOI: https://doi.org/10.1016/j.cma.2020.113569. URL: https://www.sciencedirect.com/science/article/pii/S0045782520307544.

[132] Jay P. Boris and David L. Book. "Flux-Corrected Transport. I. SHASTA, A Fluid Transport Algorithm That Works". In: *Journal of Computational Physics* 11.1 (Jan. 1973), pp. 38–69. DOI: 10.1016/0021-9991(73)90147-2.

[133] Steven T Zalesak. "Fully multidimensional flux-corrected transport algorithms for fluids". In: *Journal of Computational Physics* 31.3 (1979), pp. 335–362. ISSN: 0021-9991. DOI: https://doi.org/10.1016/0021-9991(79)90051-2. URL: https://www.sciencedirect.com/science/article/pii/0021999179900512.

[134] Steven T. Zalesak. "The Design of Flux-Corrected Transport (FCT) Algorithms for Structured Grids". In: *Flux-Corrected Transport: Principles, Algorithms, and Applications*. Ed. by Dmitri Kuzmin, Rainald Löhner, and Stefan Turek. Dordrecht: Springer Netherlands, 2012, pp. 23–65. ISBN: 978-94-007-4038-9. DOI: 10.1007/978-94-007-4038-9_2. URL: https://doi.org/10.1007/978-94-007-4038-9_2.

[135] E.E Kunhardt and C Wu. "Towards a more accurate flux corrected transport algorithm". In: *Journal of Computational Physics* 68.1 (1987), pp. 127–150. ISSN: 0021-9991. DOI: https://doi.org/10.1016/0021-9991(87)90048-9. URL: https://www.sciencedirect.com/science/article/pii/0021999187900489.

[136] URL: https://www.fuw.edu.pl/~pablo/kruk/ (visited on 10/17/2024).

[137] Adam Gonstal, Marek Lewicki, and Bogumila Swiezewska. "Reconstructing early universe evolution with gravitational waves from supercooled phase transitions". In: (Feb. 2025). arXiv: 2502.18436 [gr-qc].

[138] Stephan J. Huber and Miguel Sopena. "An efficient approach to electroweak bubble velocities". In: (Feb. 2013). arXiv: 1302.1044 [hep-ph].